NONRIGID REGISTRATION BASED METHOD FOR CORRECTION OF DISTORTIONS IN ECHO PLANAR IMAGES

By

Yong Li

Dissertation

Submitted to the Faculty of the

Graduate School of Vanderbilt University

in partial fulfillment of the requirements

for the degree of

DOCTOR OF PHILOSOPHY

in

Electrical Engineering

December, 2007

Nashville, Tennessee

Approved:

Professor Benoit Dawant

Professor J. Michael Fitzpatrick

Professor John Gore

Professor David Pickens

Professor Mitchell Wilkes

To my parents

and

To my beloved wife, Xin Liu, and wonderful sons, Hanfei and Peiyuan

ACKNOWLEDGEMENTS

First, I would like to thank my advisors, Dr. Benoit Dawant and Dr. J. Michael Fitzpatrick for their teaching, guidance and support. I feel honored to have two great professors to be my advisors. Both of them provide tremendous amount of help and advice on my studies and research. This work would not have been done without the support of them.

I would also like to thank Dr. David Pickens not only for being my committee member but also for having me in his project. He is always being nice and provides a lot of help to me during my entire stay here. I would like to thank Dr. John Gore and Dr. Mitchell Wilkes for serving on my committee and providing invaluable insights on my work. I also want to thank Dr. Victoria Morgan. She helps me on data acquisition and is always willing to answer my questions.

I thank all other members in MIP lab. Their friendship possesses an infinite value to me. Special thanks to Ning Xu, Rui Li and Xia Li for their great help on my studies and research work.

Nobody has been more important to me in the pursuit of this degree than the members in my family. I would like to thank my parents for their unending support and faith in me. I want to thank my wife Xin Liu for her constant love and my two lovely sons, Hanfei and Peiyuan for the delight they can always bring to me.

TABLE OF CONTENTS

LIST OF FIGURES

LIST OF TABLES

CHAPTER I

INTRODUCTION

Echo Planar Imaging (EPI) is known for its ability to acquire magnetic resonance (MR) images in a very short time. It has been widely used in many applications, such as functional magnetic resonance imaging (fMRI) for the study of brain activity, diffusion tensor imaging (DTI) for tissue fiber detection, or perfusion imaging for the measurement of blood flow at microscopic levels. However, EPI images are prone to artifacts and distortions. Because these deteriorate the analysis of the images, artifacts and distortions need to be corrected prior to the analysis.

A significant source of EPI image distortions is inhomogeneity in the main static magnetic field (B_0). Both object independent factors, such as field imperfections and gradient nonlinearities, and spatially varying magnetic susceptibilities in the object contribute to inhomogeneity of B_0. Furthermore, when acquiring several images over time, the susceptibilities can also be time-varying due to subject movement or respiration effects, which induce time-varying field inhomogeneities. Such inhomogeneities lead to geometric and intensity distortions in EPI images. Methods based on nonrigid registration have been employed to correct these distortions. These methods, by registering an EPI image to a reference image with negligible distortions, generate an image transformation that is applied to the EPI image to produce a corrected one, and they often rely on transformations with a very large number of degrees of freedom. Due to the complexities of the images to be registered and the registration algorithm itself, it is still a challenging task to make these methods perform robustly and accurately.

1. Research Goal and Contribution

The goal of this research is to develop new methods based on nonrigid registration to correct for distortions in EPI images, to evaluate the effectiveness of the proposed methods, and to compare the proposed methods with a commonly used method: the field-map method. The effectiveness of any method based on registration depends on an accurate registration, and one approach to improving registration accuracy is to incorporate knowledge about the existing deformation into the registration process. In this work we add into our nonrigid registration algorithm known information about the distortions in EPI images. The proposed correction schemes are evaluated on both simulated and real images.

The main contributions of this research are as follows.

We include along with a standard Jacobian correction factor a new "rephasing" factor in the registration. We incorporate both factors into a previously published nonrigid registration algorithm—the Adaptive Bases Algorithm, or ABA—such that not only geometric distortion but also intensity distortion and attenuation in Gradient Echo (GE) EPI images can be corrected after the registration process. Nonrigid registration methods, such as ABA, are usually used to deform the shape of one image to make it match another one. However, in EPI images, because of the geometric distortion, the MR signal is redistributed in the reconstructed image, resulting in intensity distortion. This effect can be handled with the Jacobian factor. However, in GE EPI, which is the primary type of image used in functional MRI, intravoxel dephasing causes signal loss and thus intensity attenuation in the images. It is this attenuation which is corrected by the rephasing factor. Both of these intensity changes affect the accuracy of the ABA method,

which uses intensities for computation of the similarity measure. In our method, we compute the Jacobian factor and the rephasing factor from the deformation field after each update and incorporate them into the measure of image similarity. Our results show that the inclusion of these two factors improves the accuracy of estimation of geometric distortion and permits the correction of intensity values in GE EPI images.

We also incorporate into our registration method a spatially varying scale mechanism to better approximate the geometric distortion in EPI images. The character of the geometric distortion in different regions of an EPI image can be quite different, thus suggesting the use of deformations whose properties are adapted spatially. We use a scale map to adapt the local scale of the transformations. To compute the scale map, a technique is proposed that relies on an estimate of the expected deformation field. This estimate is computed using knowledge of the physical processes that induce distortions in EPI images. We find that, in comparison with our earlier method using fixed scale, the proposed method finds deformation fields that are smoother and finds them faster without sacrificing accuracy.

We propose in addition a hybrid method that combines both a field map and nonrigid registration for correction of distortions in EPI images. Field-map methods and nonrigid registration methods are the two most common post-processing techniques used in distortion correction for EPI images. Each of them has its advantages and disadvantages. The combination of these two has not yet been investigated. In this work, we use a measured field map to compute the initial values for the deformation field. This deformation field is then updated using nonrigid registration to compensate inaccuracies

in field-map measurements. A mask is generated according to the field map and the EPI image, and is used to constrain the deformation field during the registration.

Finally, we compare three distortion correction methods for EPI images on both 3T and 7T datasets. The aim of this comparison is to find how field-map method and registration method compare and which one of them should be chosen under certain situations. The methods we have compared include: the field map method (i.e., no registration), registration with spatially varying scale, as described in Chapter IV (i.e., no field map), and a method that combines both field map and registration, as introduced in Chapter V. Our results indicate that field-map methods should be used for the correction of relatively small geometric distortion. For intensity correction or for the correction of distortions in EPI images in which the distortions are much larger, the registration method and the combination method lead to better results.

2. Significance

EPI is widely used for a lot of applications, for example functional MRI (fMRI). Functional MRI, one of the most important developments in MRI, provides noninvasive measurements of human brain function. It is capable of detecting brain function in regions of the human cortex when tasks are performed or stimuli are received. fMRI is now used for the localization of visual, motor, language, memory, and somatosensory response for surgical resection [61], localization of "handedness", and elucidation of brain function and metabolism altered by pathologies such as stroke, multiple sclerosis [62], and Alzheimer's disease [63]. fMRI has also been used in clinical assessment of brain function. After acquiring fMRI scans, statistical analysis is needed to detect the

activation areas. Most often, the fMRI images are then aligned, i.e., "registered", with a high-resolution anatomic image to identify precisely the anatomical location of the fMRI-based findings. Distortions in fMRI images will affect both the statistical analyses and the correlation between functional and anatomical information, and thus need to be corrected effectively.

MR scanners with higher and higher magnetic field are being built and deployed. As the strength of the magnetic field increases, so does the signal to noise ratio. This will permit increasing the spatial resolution of the images and shorten scanning time. But, the severity of the distortion artifacts also increases with the magnetic field. Correction of distortion in EPI images will thus remain an important topic in the years to come.

A large body of work addressing such problems has been published. However, despite these efforts, methods that can be used routinely are still lacking. The long term objective of the work presented herein is to advance the state of the art in this area.

3. Overview

This chapter summarizes the goal, the main contribution, and the significance of this research. The reminder of the thesis is organized as follows. Chapter II introduces some background and related work. Chapter III presents a new approach for retrospective correction of the geometric distortion and signal loss in GE EPI images. Chapter IV proposes a spatially varying scale mechanism for our nonrigid registration method and applies it to geometric distortion correction in EPI images. Chapter V presents a field map constrained nonrigid registration approach for correction of distortions in EPI

images. Chapter VI compares three distortion methods. Chapter VII concludes this thesis and provides recommendations for future work.

CHAPTER II

BACKGROUND AND RELATED WORK

1. Distortions in EPI Images due to Main Magnetic Field Inhomogeneity

Echo Planar Imaging (EPI) is a magnetic resonance imaging (MRI) technique permitting very rapid data acquisition. It acquires multiple image lines in k space (usually all lines in k space) after a single excitation, which leads to a very short scan time—2 seconds for a 3D image is usual, as compared with scan times of three to five minutes for a conventional sequence, termed a "spin-warp" sequence. This makes EPI a widely used fast imaging technique in many applications, such as functional magnetic resonance imaging (fMRI), diffusion weighted imaging (DWI), and dynamic imaging with contrast agent enhancement. The tradeoff is a relatively low resolution (64 x 64 or 128 x 128). Also, a well-known problem with EPI is that it is more sensitive to image distortions than conventional MRI due to the encoding scheme that is used. The EPI acquisition requires a longer readout time and therefore a lower bandwidth along the phase encoding direction, which accentuate the geometric distortion in this direction due to off-resonance factors, such as inhomogeneity in the static B_0 field, chemical shift, eddy-current effects, etc. See Figure 1 for an example. Among these factors, a primary source of distortion is inhomogeneity in the static B_0 field [58], which we deal with in this work. This inhomogeneity is induced mainly by the magnetic susceptibility differences between various structures within the object placed inside the scanner. For head imaging, such inhomogeneities often occur at air-tissue or bone-tissue interfaces, such as those in the vicinities of the mouth, the nasal sinuses, and the ears. They cause severe geometric

distortion in certain brain areas, especially the orbitofrontal cortex and the temporal lobes. In addition to the geometric distortion, the acquired MR signals are redistributed in the reconstructed image space, which results in intensity distortion. In Gradient Echo (GE) EPI images, which are commonly used for fMRI, field inhomogeneity also gives rise to intravoxel dephasing, which causes signal loss (i.e., intensity reduction in the image) in some areas. These geometric and intensity distortions degrade image quality and will thus have an impact on the analysis of these images.

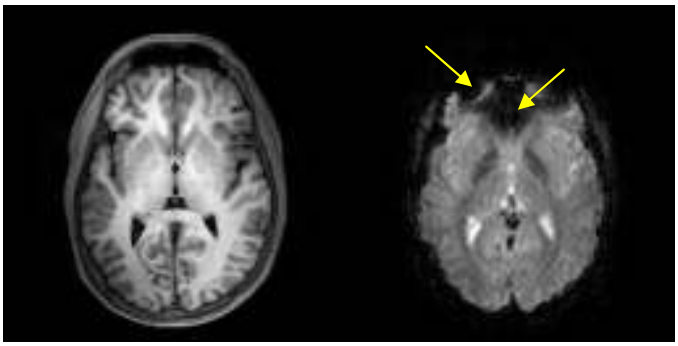

(a) (b)

Figure 1: Illustration of EPI distortion. (a): A conventional MRI; (b): An EPI image. The distortions are mainly present in the frontal part of the EPI image, as indicated by the arrows.

Furthermore, when acquiring a series of images, an additional difficulty caused by motion during the acquisition needs to be addressed. Indeed, when motion artifacts are ignored, one single EPI volume can be corrected and the same correction applied to all the other aligned volumes in the series. But when changes in the image due to head movement or other dynamic effects, such as those generated by respiration are considered, the correction needs to be adjusted differently for each volume in the time series. Even if the only dynamic changes are due to re-orientation of the head, a simple re-orientation of

the geometric correction computed on one volume is not sufficient to correct the other volumes. The reason is that the distortion map for a rotated head is different from the rotated version of the distortion map of the head before rotation [1].

2. Distortion Correction Methods

Many methods have been proposed to correct for distortions in EPI images caused by inhomogeneity in the main magnetic field. Shimming techniques, such as global shimming [3] or dynamic shimming [4], can be performed before images are acquired by adjusting the main magnetic field B_0 to maximize its homogeneity. However, even after shimming, substantial field variations often remain, especially for those areas at the interfaces between substances with very different magnetic susceptibilities, where the field changes very rapidly. A technique called "z-shimming" alters the strength of the slice-selection gradient to compensate for the "through-plane" dephasing, which is caused by the component of field inhomogeneity perpendicular to the imaging plane [5], [6]. Unfortunately, z-shimming does not compensate for "in-plane" dephasing and it compensates for through-plane dephasing only at a few selected small regions in the volume, while exacerbating the effect in other areas.

Another approach is to modify the standard acquisition sequences to acquire more information during the imaging process and to use this information to reduce acquisition artifacts. Chen *et al.* [7], [8] developed a phase-shift EPI pulse sequence to encode the EPI phase errors due to off-resonance-related factors. The encoded information can be applied to remove EPI distortions. While these methods can reduce geometric distortions

and even signal loss [9], they also lengthen the acquisition time and/or require specialized technical support, which is not always available.

The so-called "forward-reverse" or "reversed-gradient" method was initially applied to correct distortions in images from spin-warp imaging [10] and then extended to EPI [11]-[13]. In this approach, a second image of the same object is acquired with one gradient reversed, which leads to reversed geometric distortion. These images are then used to generate the corrected image. It should be noted that this technique doubles the acquisition time and is vulnerable to noise, large distortions, and motion of the imaged object between acquisitions.

The Point Spread Function (PSF) method relies on the fact that a distorted image can be described as a non-stationary convolution of an undistorted image with a spatially variant point-spread function that characterizes the effect of field inhomogeneities on the image. In this method, several additional images of the same object are acquired with additional phase-encoding gradient of varying strength applied before readout to map the PSF of each voxel. These PSFs encode the spatial information about the distortion and the overall distribution of intensities from a single voxel [14]. This method also increases the acquisition time significantly and is vulnerable to motion of the imaged object during the several image acquisitions.

SENSitivity Encoding (SENSE) [73], one of the parallel imaging techniques, acquires a smaller number of k space lines in the phase encoding direction, and then uses a combination of the sampled signal from multiple coils to reconstruct the whole image. This increases the bandwidth in the phase-encoding direction, which mitigates the geometric distortion artifact [74], [75]. SENSE is now commonly used for fMRI,

diffusion imaging, and cardiac imaging to reduce both scan time and geometric distortion. However, signal attenuation caused by intravoxel dephasing cannot be reduced by such techniques.

Field-map methods [15]-[18] employ a measured field map for the object inside the scanner to compute the existing distortions in the EPI images according to relationships between spatial distortion and field inhomogeneity. Preprocessing methods such as regularization [19] and unwrapping [20] algorithms are often needed to obtain a smooth field map. See Figure 2 for example. The accuracy of the obtained field map is sensitive to various effects, such as subject motion, respiration, blood flow, and the performance of the aforementioned processing algorithms.

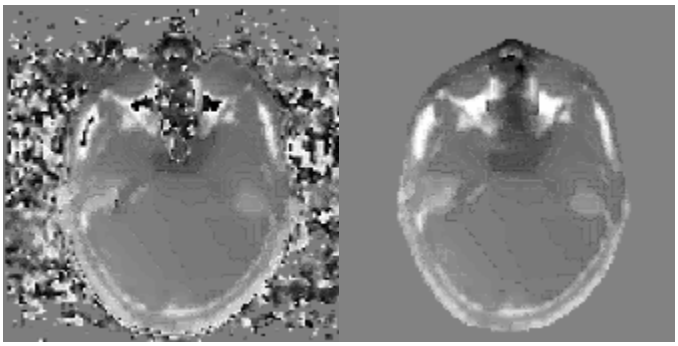

Figure 2: A measured field map before (left) and after (right) preprocessing.

Other correction methods have also been proposed. Andersson *et al.* [1] employ a set of cosine basis functions to model the field inhomogeneity. The coefficients of the basis functions are computed using the EPI images and movement parameters estimated using a rigid-body registration algorithm. Signal loss is not considered in their work. In [21], an imaged organ is enveloped with a layer of material that has similar susceptibility

to that of the organ to shift the field inhomogeneity away from the imaged tissue. While this procedure is simple to implement and able to reduce distortions in EPI images to some degree, it does not work well, as the authors point out, for organs with complex shape and internal air cavities, such as the human head.

All of these correction methods reduce the effects of geometrical distortion, but only z-shimming has an effect of intravoxel dephasing. As pointed out above, z-shimming helps only with one component of this dephasing and only in selected regions of the image. Dephasing causes intensity attenuation in GE acquisitions, and intensity attenuation confounds the statistical analysis required for fMRI, which relies on GE. Thus, correction methods that effectively include the effects of dephasing along with geometrical distortion are needed.

3. Registration-Based Methods for Distortion Correction

Registration-based methods have also been proposed for distortion correction in EPI images [22]-[35]. Such methods, by registering an EPI image to a reference image with no or negligible distortion, generate a deformation field that is then applied to the EPI image to produce a corrected one. An illustration is given in Figure 3.

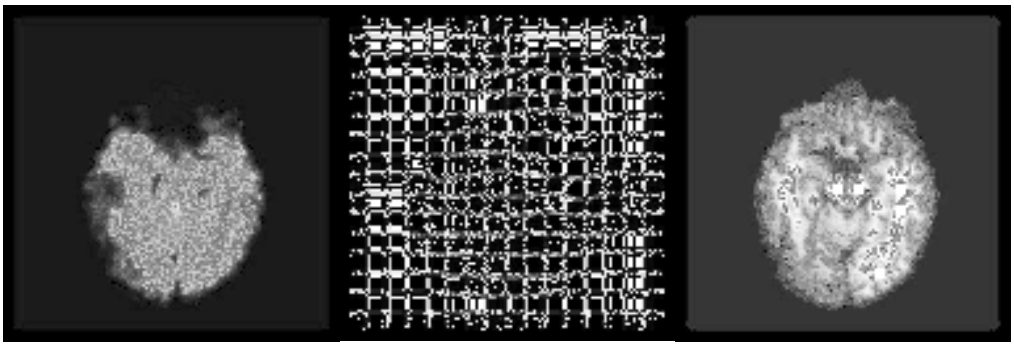

(a) (b) (c)

Figure 3: An illustration of registration method for distortion correction. (a): An EPI image; (b): An obtained deformation field; (c): A reference image.

Studholme *et al.* [22] register SE EPI images to a spin-warp SE image. They derived constraints for a nonrigid registration algorithm, which are based on physical principles governing SE EPI imaging. The deformation is estimated in only one direction (the phase encoding direction), and the Jacobian of the deformation field is used to correct for intensity distortion. They use a set of cubic B-splines to parameterize the transformation and the normalized mutual information between these images as the similarity measure. Kybric *et al.* [23] present a unidirectional registration algorithm to unwarp distorted EPI images by registering them to a spin-warp GE image. They also model the deformation field with B-splines but use the sum of squared differences (SSD) as the similarity measure. A preprocessing step that consists of filtering and histogram equalization is applied to compensate for intensity differences between source and target images. Hellier and Barillot [24] use a piecewise affine transformation to estimate a deformation field for the correction of geometric distortions in EPI images. They use mutual information as the cost function.

In [25], Skerl *et al.* employ optic flow to register EPI images to T_1-weighted images. The proposed approach includes skull removal and intensity remapping. Ardekani and Sinha [26] use a registration method based on optical flow to correct the geometric distortions in diffusion-weighted images (DWIs) due to both magnetic field inhomogeneities and eddy current effects. They first register a baseline EPI (no diffusion weighting) to a T_2-weighted fast-spin-echo (FSE) image and then use the obtained deformation map to initialize the warping of the DWIs to the FSE image. This approach requires preprocessing of the EPI images with global or local intensity matching, which, in turn, requires segmentation. No correction of intensity distortion is included. In [27], Gholipour *et al.* use distortion regions estimated from a measured field map to constrain the deformation parameters during the nonrigid registration of EPI images to a reference image. Pauchard *et al.* [28] aim at reducing the distortions in images with metallic implants by employing a point-based registration algorithm that produces a transformation based on the thin-plate spline. A specially designed 3-D grid phantom is initially imaged as a reference image. Then a metallic implant, which is the same as that in the patient environment, is positioned in this grid phantom and imaged to produce a distorted image. The transformation is calculated on the basis of points extracted from the distorted grid images and from the reference image. In this work, deformation is constrained to be in the readout direction and intensity correction using the Jacobian of the transformation is included.

Registration-based methods for reducing the distortions in DWI usually use an affine model or a geometric distortion model derived from acquisition principles, which leads to the estimation of a few parameters as in [29], [30]. Netsch *et al.* [31], [32] study

image-based distortion correction in DWI. They apply a consistency test to compare a dedicated transformation adapted to distortion induced by eddy currents [2] and a 3D affine transformation as well as similarity measures using mutual information (MI) and local correlation. Nielsen *et al.* [33] compare the affine and polynomial registration for correction of distortion induced by eddy currents in diffusion tensor imaging of newborns. They use mutual information as their similarity measure. Based on visual inspection of fractional anisotropy maps obtained with both registration techniques, they found that 2nd order polynomial registration performs slightly better than affine registration for artifact reduction. Rohde *et al.* [34] used a registration algorithm based on MI to correct both rigid-body motion and distortion induced by eddy currents in DWI images. They align DWI images to a reference image by optimizing a cost function with 14 parameters, which include a rigid motion with six degrees of freedom and a quadratic term to model the effect of eddy currents. A brightness correction factor is then used to correct the intensity distortions in the image. Mistry *et al.* [35] use a Fourier Transform as the interpolation method in an affine registration algorithm to correct distortions in DWI images.

4. Regularization of Deformation Fields in Nonrigid Registration

Because the geometric distortion in EPI images is not rigid motion, nonrigid registration is needed for its correction. While rigid or affine registration transforms images globally, nonrigid registration deforms images locally by finding a deformation field that maps each location in one image onto its corresponding location in the other one. The transformation T can be written as: $T(\mathbf{x}) = \mathbf{x} + \mathbf{v}(\mathbf{x})$, with $\mathbf{x}$ a coordinate vector in

image space and **v(x)** a deformation field. The deformation field can be computed in two different ways—using *parametric* or *nonparametric* methods. Parametric approaches represent the deformation field with a weighted sum of basis functions. The basis functions can have global support, i.e., spanning the entire image, such as the Discrete Cosine Transform (DCT) [36], [37] and thin-plate spline [38]-[40], or local support, i.e., being zero outside a subregion, such as B-splines [41], [42] or radial basis functions [43]. Nonparametric approaches compute the deformation for each image voxel directly. Examples include optical-flow/demon-based methods [44]-[46], elastic models, [47] and viscous fluid models [48]. The nonparametric methods are more flexible than representations using basis functions but are usually more computationally demanding.

One of the key problems with nonrigid registration methods is the need to introduce constraints on the deformation field. Nonrigid registration typically requires a very large number of degrees of freedom to capture correctly the local deformations between images to be registered. In the general case, for 3D images, each voxel in the image is allowed to be displaced independently in all three directions if there is no constraint applied. As a consequence, registration of two images with 256x256x128 voxels can lead to a problem with more than 25 million unknown parameters. This is not only computationally demanding but also requires solving problems such as topological correctness, invertability, and correctness of the transformation over homogeneous regions. To solve these issues, regularization of the deformation fields is often required. The regularized deformation field is typically assumed to be a continuous, one-to-one, and topology preserving mapping [49]. However, for pairs of images having different

anatomic components or components that have a different topology, such one-to-one mapping may not even exist.

A number of techniques have been used to regularize the deformation field. One approach is to regularize the field *uniformly*. In [41], for example, Rueckert *et al*. add a penalty term, related to the second derivative of the deformation field, to the cost function to constrain the transformation to be smooth. Rohlfing *et al.* [50] propose volume-preservation transformations, which are achieved by introducing a term that penalizes transformations whose Jacobian is different from one. Thirion *et al*. [44] and Guimond *et al*. [45], use a stationary Gaussian filter to smooth the deformation field after each update in a demon-based registration algorithm. In [43] Rhode *et al.*, apply a constraint to the relative value of the coefficients of adjacent basis functions to keep the Jacobian of the transformation positive definite. In many situations, however, the characteristics of the deformation are spatially dependent due to intrinsic properties of the images to be registered. For example, in images consisting of hard tissue and soft tissue, the former is expected to remain more rigid than the latter. A priori information about the deformation can be used to *adapt spatially* the regularization of the deformation fields and methods to do so have been proposed recently. In [51] Hellier *et al*. use a robust estimator on the regularization term to take into account possible discontinuities of the deformation field in a registration method based on optical flow. In [52] Hava *et al*. propose a modified viscous-fluid algorithm to reduce or prohibit deformations in specific areas based on an initial segmentation. Duay *et al.* [53] assign different values to a stiffness parameter used in the method described in [43] for image regions with different properties, thereby permitting the spatial adaptation of the transformation characteristics. In [54] Staring *et al*.

propose three constraints on the Jacobian of the local deformation field inside a pre-generated mask to preserve the rigidity of the transformation on vessels. Li *et al.* [55] add an additional term to the cost function for minimizing the displacement of bone structure and use it for whole-body registration. Stefanescu *et al.* [46] employ two non-stationary regularization steps in a demon-based algorithm. They apply diffusion equations to both the intermediate correction field and the overall deformation field. The image gradient and information on structures in the images are used to provide values for the parameters in the diffusion equations. In [59], Commowick *et al*. employ an idea similar to Stefanescu's in [46] to build a statistical stiffness map for the deformation field.

When basis functions are used for parameterizing the deformation field, the support size of each basis function also affects the regularization of the deformation field. Smoothness of the deformation field is intrinsic at scales smaller than the support size. To accommodate highly local deformations, a high density of basis functions with a small support size is needed. But relying on a dense regular grid of basis functions leads to a complex optimization problem with a very large number of degrees of freedom. In recent years, approaches have been proposed to address this problem. For instance, Rohde *et al.* [43] put basis functions on a regular grid first and then identify mismatched regions based on the gradient of the cost function with respect to the coefficients of these basis functions. Control points are then placed only on these regions and are optimized separately. Rohlfing *et al.* [56] and Schnabel *et al.* [57] use local entropy to identify active and inactive regions, and only control points in the active regions are allowed to be changed during the optimization. Similarly, Park *et al.* [40] identify those mismatched

regions based on local Mutual Information (MI) and entropy measures, and they add one control point each time at the location where the maximum local mismatch occurs.

The above techniques explore various ways to introduce constraints into nonrigid registration for different applications. In this thesis, our purpose is to add prior knowledge into nonrigid registration methods for the correction of distortions in EPI images. In the following chapters, we present several approaches to do this and we provide a comparison among three different methods.

CHAPTER III

ACCOUNTING FOR SIGNAL LOSS DUE TO DEPHASING IN THE CORRECTION OF DISTORTIONS IN GRADIENT-ECHO EPI VIA NONRIGID REGISTRATION

1. Introduction

Because they can be acquired very rapidly, GE EPI images are commonly used for applications such as functional imaging and cardiac imaging. But EPI images are sensitive to geometric distortions caused by main magnetic field inhomogeneity [58]. Such distortions are a major source of problems in functional studies because they can compromise both the activation detection results and the accurate correlation of activation sites with their corresponding anatomical locations. Also, unlike spin-echo (SE) EPI images, in which signal is preserved during the image formation process, GE EPI images suffer from signal loss (i.e. intensity reduction) caused by intravoxel dephasing, which further complicates the problem.

As introduced in Chapter II, many registration based methods have been proposed to correct distortions in EPI images. While MR imaging physics has been used in some of these methods (see for instance [22], [23], [25]-[27], [34]), a physics-based model specifically derived for GE EPI has not been incorporated into any of them. This chapter presents an extension to a previously published registration-based correction method, which is designed to correct GE EPI images. After describing our method, we test it on both simulated and real images.

The reminder of the chapter is organized as follows. In Section 2, we derive the correction term we introduce and the registration algorithm we use. In Section 3, we

apply the method to both simulated and real brain data. Finally, in Section 4, we discuss the advantages and disadvantages of the proposed approach.

2. Methods

2.1. Signal in gradient echo EPI

Inhomogeneity in the static magnetic field (B_0) can cause not only geometric and intensity distortions in GE EPI images but also intravoxel dephasing, which leads to signal loss. Considering normal 2D GE EPI, let m and n represent the m^{th} and the n^{th} sampling points in the readout and the phase encoding directions, respectively, with $-M/2 \le m < M/2$, $-N/2 \le n < N/2$. Ignoring T_2 effects, the MR signal S for a slice at location z_1 in the presence of field inhomogeneity $\Delta B(x,y,z)$ can be expressed as an integration of the signals from the spins over the excited slice:

$$S(m,n,z_1) = A\iiint p(\omega(x,y,z)-\omega_1)\rho(x,y,z)e^{-i2\pi\gamma\left(xG_x m\Delta t_x + yn\overline{G}_b\tau_p + \Delta B(x,y,z)t\right)} \quad (1)$$

Here, A is a constant, $p(\omega(x,y,z)-\omega_1)$ is the slice selection (here z) profile, with $\omega(x,y,z)$ the spins' frequency of precession and ω_1 the frequency of the RF pulse; $\rho(x,y,z)$ is the spin density at location (x,y,z) , γ is the gyromagnetic ratio in Hz/Tesla ($\gamma = 42.5774\times10^6$ Hz/Tesla for hydrogen), G_x is the gradient in the x direction, $\overline{G}_b$ is the average blip gradient in the y direction during the period τ_p, Δt_x is the time interval between adjacent points in the readout direction, t is the elapsed time at the n^{th} line in the phase encoding direction and the m^{th} point in the readout direction, with the time origin at the center of the 90-degree RF pulse. t can also be expressed as:

$$t = t_{TE} + m\Delta t_x + n\Delta t_y \tag{2}$$

where t_{TE} is the echo time and Δt_y is the time interval between adjacent points in the phase encoding direction.

Let G_z be the gradient in the z direction. $\omega(x,y,z)$ and ω_1 in the slice selection profile can be computed as $\omega(x,y,z) = \gamma(B_0 + zG_z + \Delta B(x,y,z))$ and $\omega_1 = \gamma(B_0 + z_1 G_z)$. Then:

$$p(\omega(x,y,z) - \omega_1) = p\left(\gamma G_z\left(z + \frac{\Delta B(x,y,z)}{G_z} - z_1\right)\right) \tag{3}$$

Using Eqs. (2) and (3) in (1) gives:

$$\begin{aligned} S(m,n,z_1) = A\iiint p\left(\gamma G_z\left(z + \frac{\Delta B(x,y,z)}{G_z} - z_1\right)\right)\rho(x,y,z) \\ \times e^{-i2\pi\gamma\left(\left(x+\frac{\Delta B(x,y,z)}{G_x}\right)G_x m\Delta t_x + \left(y+\frac{\Delta B(x,y,z)}{G_y^{(eff)}}\right)G_y^{(eff)} n\Delta t_y\right)} e^{-i2\pi\gamma\Delta B(x,y,z)t_{TE}}\,dxdydz \end{aligned} \tag{4}$$

with $G_y^{(eff)} = \dfrac{\overline{G}_b \tau_p}{\Delta t_y}$ the effective gradient.

Defining spatial frequencies k_x and k_y in k space $k_x \equiv \gamma G_x m\Delta t_x$, $k_y \equiv \gamma G_y^{(eff)} n\Delta t_y$, Eq. (4) can be written as:

$$\begin{aligned} S(k_x,k_y,z_1) = A\iiint p\left(\gamma G_z\left(z + \frac{\Delta B(x,y,z)}{G_z} - z_1\right)\right)\rho(x,y,z) \\ \times e^{-i2\pi\left(\left(x+\frac{\Delta B(x,y,z)}{G_x}\right)k_x + \left(y+\frac{\Delta B(x,y,z)}{G_y^{(eff)}}\right)k_y\right)} e^{-i2\pi\gamma\Delta B(x,y,z)t_{TE}}\,dxdydz \end{aligned} \tag{5}$$

2.2. Geometric and intensity distortions in GE EPI images

According to the Fourier shift theorem, the additional phase in *k*-space induced by $\Delta B(x,y,z)$ will cause a pixel shift in the reconstructed image space, as can be seen in Eq. (5). Signal emanating from location (x,y,z) will be shifted to (x',y',z') with:

$$x' = x + \frac{\Delta B(x,y,z)}{G_x}, y' = y + \frac{\Delta B(x,y,z)}{G_y^{(eff)}}, z' = z + \frac{\Delta B(x,y,z)}{G_z} \tag{6}$$

Because of geometric distortions, the MR signal is redistributed in the reconstructed image, which results in intensity distortions. If the image is compressed, one image voxel will contain signal emanating from more tissue than it would if the image was not compressed; this will cause a local intensity increase. The converse is true if the image is stretched. Change in intensity values can be related simply to the local deformation through the Jacobian of this deformation. Suppose that geometric distortions map coordinate (x,y,z) to coordinate (x',y',z'). Then the Jacobian *J* of this transformation is computed as follows:

$$J = \begin{vmatrix} \frac{\partial x'}{\partial x} & \frac{\partial x'}{\partial y} & \frac{\partial x'}{\partial z} \\ \frac{\partial y'}{\partial x} & \frac{\partial y'}{\partial y} & \frac{\partial y'}{\partial z} \\ \frac{\partial z'}{\partial x} & \frac{\partial z'}{\partial y} & \frac{\partial z'}{\partial z} \end{vmatrix} \tag{7}$$

Putting Eq. (6) into Eq. (7), we get:

$$J = 1 + \frac{\partial \Delta B}{\partial x} \Big/ G_x + \frac{\partial \Delta B}{\partial y} \Big/ G_y^{(eff)} + \frac{\partial \Delta B}{\partial z} \Big/ G_z \tag{8}$$

During our correction process, we assume that J is larger than zero, so "folding" of the image does not occur. While such an assumption is reasonable under most circumstances, folding may happen when the field inhomogeneity changes rapidly, but this cannot be corrected by retrospective correction methods based on the image itself, such as the method proposed herein.

According to Eq. (6), for a location (x,y,z), the geometric distortion in each direction is linearly proportional to the inverse of the corresponding gradient in that direction, i.e., when the gradient is small, the distortion is large, and vice versa. The field of view (FOV), or physical dimension of the image, in the k_x and the k_y directions can be written as:

$$\mathrm{FOV}_x = \left(\gamma G_x \Delta t_x\right)^{-1},\ \mathrm{FOV}_y = \left(\gamma G_y^{(eff)} \Delta t_y\right)^{-1} \tag{9}$$

Typically, FOV_x and FOV_y are equal, and Δt_y can be computed as:

$$\Delta t_y = \tau_p + N_x \Delta t_x \tag{10}$$

with N_x the number of sampling points in the readout direction.

We then obtain:

$$\gamma G_x \Delta t_x = \gamma G_y^{(eff)} \Delta t_y \Rightarrow G_y^{(eff)} = G_x \frac{\Delta t_x}{\Delta t_y} = G_x \frac{\Delta t_x}{\tau_p + N_x \Delta t_x} < \frac{G_x}{N_x} \tag{11}$$

Usually the size of EPI images is 64x64 or 128x128 pixels, so $G_y^{(eff)}$ is much smaller than G_x. Also, G_z is much larger than $G_y^{(eff)}$. Because of their much larger gradients, the distortions in the readout and the slice selection directions are much smaller

than that in the phase encoding direction. In a typical EPI image, the distortions in the phase encoding direction may be up to several mm while distortions in the other directions are less than one tenth mm [16]. Here we assume that pixel displacements in the frequency and slice selection directions are negligible so that:

$$x' \approx x, y' = y + \frac{\Delta B(x, y, z)}{G_y^{(eff)}}, z' \approx z \tag{12}$$

We note that such unidirectional distortion model has been used in previous distortion correction work [22], [23], [25], [26].

Eq. (8) can thus be rewritten as:

$$J \approx 1 + \frac{\partial \Delta B}{\partial y} \Big/ G_y^{(eff)} \tag{13}$$

As shown in Eq. (22), this term is used to change the image intensity during registration.

We use Eqs. (12) and (13) as our geometric and intensity distortion models. Note that they also hold for SE EPI, as described by Studholme *et al.* [22].

2.3. Signal loss due to intravoxel dephasing in GE EPI

Intravoxel dephasing is a process in which spins within an imaged voxel lose phase coherence due to static magnetic field inhomogeneities. The phase factor $e^{-i2\pi\gamma\Delta B(x,y,z)t_{TE}}$ in Eq. (5) is the source of the intravoxel dephasing effects in GE EPI. It does not exist in SE EPI since there is an 180^o pulse that restores coherence to the spins at the echo time t_{TE}.

Changing integration variables from (x, y, z) to (x', y', z') in Eq. (5), we have:

$$S(k_x,k_y,z_1)=A\iiint p(\gamma G_z(z'-z_1))\rho(x(x',y',z'),y(x',y',z'),z(x',y',z'))\\ \times e^{-i2\pi(x'k_x+y'k_y)}e^{-i2\pi\gamma\Delta B(x,y,z)t_{TE}}J^{-1}(x,y,z)dx'dy'dz' \tag{14}$$

To obtain the reconstructed complex image, we take the inverse Fourier transform of the *k*-space data:

$$i(x_1,y_1,z_1)=C\int p(\gamma G_z(z'-z_1))\rho(x(x_1,y_1,z'),y(x_1,y_1,z'),z(x_1,y_1,z'))\\ \times e^{-i2\pi\gamma\Delta B(x,y,z)t_{TE}}J^{-1}(x,y,z)dz' \tag{15}$$

here *C* is a constant. In the above equation, we ignore the fact that the signal in *k*-space is acquired for only a finite amount of time. Otherwise, we would need to convolve the image obtained with Eq. (15) with a point spread function of the *k*-space truncation filter, as in [4], [65].

Assuming that the spin density $\rho(x,y,z)$ and the Jacobian $J(x,y,z)$ at voxel (x_1,y_1,z_1) are constant, and that the slice selection function *p* is a boxcar, Eq. (15) can be written as:

$$i(x_1,y_1,z_1)=D\rho(x(x_1,y_1,z_1),y(x_1,y_1,z_1),z(x_1,y_1,z_1))J^{-1}(x,y,z)v_z^{-1}\int_{z_1-\Delta z/2}^{z_1+\Delta z/2}e^{-i2\pi\gamma\Delta B(x,y,z)t_{TE}}dz'\\ =i_0(x,y,z)J^{-1}(x,y,z)v_z^{-1}\int_{z_1-v_z/2}^{z_1+v_z/2}e^{-i2\pi\gamma\Delta B(x,y,z)t_{TE}}dz' \tag{16}$$

with *D* a constant, $i_0(x,y,z)$ the complex image without distortion and v_z the voxel size in the z direction. If the voxel size is not too large and the variation of ΔB is not too severe, ΔB across the voxel of interest can be written as a linear field:

$$\Delta B=\Delta B_0+(x'-x_1)\Delta B_{x_1}+(y'-y_1)\Delta B_{y_1}+(z'-z_1)\Delta B_{z_1} \tag{17}$$

with $\Delta B_{a1}=\partial\Delta B/\partial\alpha\big|_{\alpha=a1}$, in which *a* can stand for *x*, *y*, or *z*.

Combining Eqs. (16) and (17) gives:

$$\begin{aligned} i(x_1,y_1,z_1) &= i_0(x,y,z)J^{-1}e^{-i2\pi\gamma t_{TE}\left(\Delta B_0+(x'-x_1)\Delta B_{x_1}+(y'-y_1)\Delta B_{y_1}\right)}v_z^{-1}\int_{z_1-v_z/2}^{z_1+v_z/2}e^{-i2\pi\gamma t_{TE}(z'-z_1)\Delta B_{z_1}}dz' \\ &= i_0(x,y,z)J^{-1}e^{-i2\pi\gamma t_{TE}\left(\Delta B_0+(x'-x_1)\Delta B_{x_1}+(y'-y_1)\Delta B_{y_1}\right)}\mathrm{sinc}\left(\Delta\phi_{z_1}/2\right) \end{aligned} \quad (18)$$

Here, $\Delta\phi_{z_1} = 2\pi\gamma v_z t_{TE}\Delta B_{z_1}$ (19)

The factor $e^{-i2\pi\gamma t_{TE}\left(\Delta B_0+(x'-x_1)\Delta B_{x1}+(y'-y_1)\Delta B_{y_1}\right)}$ changes the phase of the image but not the magnitude. By taking the magnitude of the complex image, we obtain:

$$\left|i(x_1,y_1,z_1)\right| = \left|i_0(x,y,z)\right|J^{-1}\left|\mathrm{sinc}\left(\Delta\phi_{z_1}/2\right)\right| \quad (20)$$

We define

$$h(x,y,z) \equiv \left|\mathrm{sinc}\left(\Delta\phi_{z_1}/2\right)\right| \quad (21)$$

as the "dephasing factor", which describe the dephasing effects due to ΔB in the slice selection direction [65]-[68], and accordingly $h^{-1}(x,y,z)$ as the "rephasing factor". ΔB also causes dephasing effects in the *x* and *y* directions [4], [65], which are omitted here because, as a result of the relatively small voxel sizes in these directions, they are typically much smaller than *h*. With Eqs. (20) and (21), the distortion corrected image can be calculated as:

$$\left|i_0(x,y,z)\right| = \left|i(x,y_1,z)\right|\cdot J(x,y,z)\cdot h^{-1}(x,y,z) \quad (22)$$

Here the geometric distortions in the x and z directions are omitted, i.e. $x_1 = x$ and $z_1 = z$. According to the above equation, the intensity value at (x,y,z) in the corrected image can

be computed by multiplying the intensity value at (x, y_1, z) in the distorted image by both the Jacobian and rephasing factors at (x, y, z). The amount of intensity changes at a certain location caused by geometric distortion and intravoxel dephasing depends on the magnitudes of J^{-1} and h at this location, respectively. The values of J^{-1} and h are each proportional to the gradient of ΔB in the y and z directions, separately. While J^{-1} can have values ranging from smaller than one to larger than one, h always takes values smaller than one. Usually h is dominant in the regions close to the air and tissue interfaces, e.g. the frontal sinus of brain.

2.4. Nonrigid registration algorithm

Our nonrigid registration method is based on the ABA algorithm proposed in [43]. In this algorithm, the deformation field is modeled as a linear combination of a set of basis functions:

$$\mathbf{x}' = \mathbf{x} + \sum_{i=1}^{n} \mathbf{c}_i \Phi(\mathbf{x} - \mathbf{x}_i) \tag{23}$$

where, $\mathbf{x}$ and $\mathbf{x}'$ are corresponding locations in units of voxels in two images to be registered, and $\Phi(\mathbf{x} - \mathbf{x}_i)$ is the basis function centered at location $\mathbf{x}_i$ with coefficient $\mathbf{c}_i$. $\Phi(\mathbf{Y}) = \phi(\|\mathbf{Y}\|_2 / s)$, with $\|\cdot\|_2$ the Euclidean norm, and s the size of the support of the basis function. $\phi(\cdot) = \phi_{k,l}(\cdot)$, with k=1 and l=2, is one of Wu's compactly supported radial basis functions (RBF) [76]. It is C^2 smooth and strictly positive definite in R^3. An optimum transformation is obtained by finding the coefficients of the basis functions that maximize the normalized mutual information between the images. In a typical application,

registration is performed in a multilevel approach by progressively changing the resolution of the images and the support region of the basis functions. At each level, a set of basis functions with the appropriate size is first placed on a regular grid. The gradient of the similarity measure with respect to the coefficients of the basis functions is then computed and used to identify regions of mismatch. Optimization is performed on these regions independently. The process is repeated until the highest image resolution and highest density of basis functions is reached. Note that modifying the value of one of the coefficients affects only the displacements in a local region due to the basis functions' compact support. The support region of the basis function can thus be adapted for capturing displacements at various scales.

In this work, the geometric distortion in a GE EPI image is estimated by registering it nonrigidly to a reference image in which geometric distortions are negligible. The distortion model for GE EPI, given by Eq. (22), is incorporated into the registration process, which includes unidirectional deformation and intensity corrections using the Jacobian and rephasing factors. The displacement in the phase encoding (here y) direction at location $\mathbf{x}$ ($\mathbf{x} \in R^3$) in the reference image with voxels as units, $DF_y(\mathbf{x})$, is parameterized by the linear combination of the basis functions as described in Eq. (23):

$$DF_y(\mathbf{x}) = \sum_{i=1}^{N} c_i \Phi(\mathbf{x} - \mathbf{x}_i), \quad 1 \le i \le N . \tag{24}$$

According to Eq. (12), we constrain the displacement to be in the y direction only, so the displacement at location $\mathbf{x}$ is $DF(\mathbf{x}) = \begin{bmatrix} 0 & DF_y(\mathbf{x}) & 0 \end{bmatrix}^T$. Relating this to Eq. (12), we have:

$$\frac{\Delta B(\mathbf{x})}{G_y^{(eff)}} = DF_y(\mathbf{x}) v_y \,. \tag{25}$$

The multiplicative factor v_y, which is the voxel size in the y direction, changes the units of displacement from voxel to mm. Then $\mathbf{x}' = \mathbf{x} + DF(\mathbf{x})$, with **x'** the location corresponding to **x** in the distorted image.

Because the undistorted reference image is typically a T1-weighted image and the EPI images are typically T2-weighted images, we use the normalized mutual information [69] between the images as our similarity measure E_{sim}. With the distortion model of GE EPI described in Eq. (22), we have:

$$E_{sim} = \frac{H(I_R(\mathbf{x})) + H\left(I_E(\mathbf{x}, DF(\mathbf{x})) \cdot J(\mathbf{x}, DF(\mathbf{x})) \cdot h^{-1}(\mathbf{x}, DF(\mathbf{x}))\right)}{H\left(I_R(\mathbf{x}), I_E(\mathbf{x}, DF(\mathbf{x})) \cdot J(\mathbf{x}, DF(\mathbf{x})) \cdot h^{-1}(\mathbf{x}, DF(\mathbf{x}))\right)}. \tag{26}$$

Here, $I_R(\mathbf{x})$ and $I_E(\mathbf{x}, DF(\mathbf{x}))$ are the reference image and deformed EPI image, respectively, and $H(\cdot)$ and $H(\cdot,\cdot)$ stand for the marginal entropy and joint entropy functions, respectively. Note that the Jacobian factor $J(\mathbf{x}, DF(\mathbf{x}))$ and rephasing factor $h^{-1}(\mathbf{x}, DF(\mathbf{x}))$ are included in the cost function. Given a deformation field *DF,* the intensity value at each location **x** in the distortion-corrected EPI image is first estimated from the original EPI image through trilinear interpolation, and then multiplied by $J(\mathbf{x}, DF(\mathbf{x}))$ and $h^{-1}(\mathbf{x}, DF(\mathbf{x}))$ for local intensity correction.

The Jacobian *J* is computed from the deformation field (*DF*). The rephasing factor h^{-1} is computed from the gradient of ΔB according to Eqs. (19) and (21). Given *DF,* according to Eq. (25), the corresponding ΔB can be calculated as:

$$\Delta B(x,y,z) = DF_y(\mathbf{x})v_y G_y^{(eff)} = \frac{DF_y(\mathbf{x})v_y}{\gamma \mathrm{FOV}_y \Delta t_y}. \quad (27)$$

Here, $\mathrm{FOV}_y = \left(\gamma G_y^{(eff)} \Delta t_y\right)^{-1}$ is the field of view (FOV), or physical dimension of the image, in the y direction. Next, as required in Eq. (19), the gradient of ΔB in the z direction at each location is estimated using finite difference. An alternative would be to compute this gradient analytically from the parameterized deformation field in Eq. (24). Experiments show that both methods provide very similar results when the space between the locations of adjacent basis functions is not too small (larger than 5 voxels).

3. Experiments and Results

3.1. Simulated GE EPI image

In order to evaluate the proposed algorithm for distortion correction, we employed an MR simulator, which we have developed [64], to generate a distortion-free EPI image as a reference image. We then used this reference image and a measured field map to create a simulated EPI image with geometric distortion and modified intensity values using Eq. (22). Inputs to the simulator are three tissue volumes: white matter, gray matter, and CSF, which are segmented from a T1-weighted volume acquisition of a human subject's head. The output is a simulated 128x128x28 distortion-free GE EPI image. Imaging was performed on a Philips Intera Achieva 3T MR scanner. The T1-weighted image was acquired using an Inverse Recovery Turbo Spin Echo (IR TSE) pulse sequence with 28 slices, 4.5 mm slice thickness, 0.4 mm gap, matrix size 256x256, field of view (FOV) 240mm, TE = 10ms, and TR = 2000ms. A field map of the same subject

was acquired during the same study from the phase difference between two Fast Field Echo (FFE, gradient echo) scans collected at differing echo times. The field map has the same dimensions and voxel size as the anatomical image. It was first unwrapped using PRELUDE in FSL [70] and then used to compute the distortions in the GE EPI, which were applied to the reference image to simulate a real GE EPI image. Before the simulation, both the reference image and the field map were masked using a brain mask obtained with BET [70]. The geometric distortion computed from the field map is used as the ground truth to which the deformation fields obtained with our method is compared.

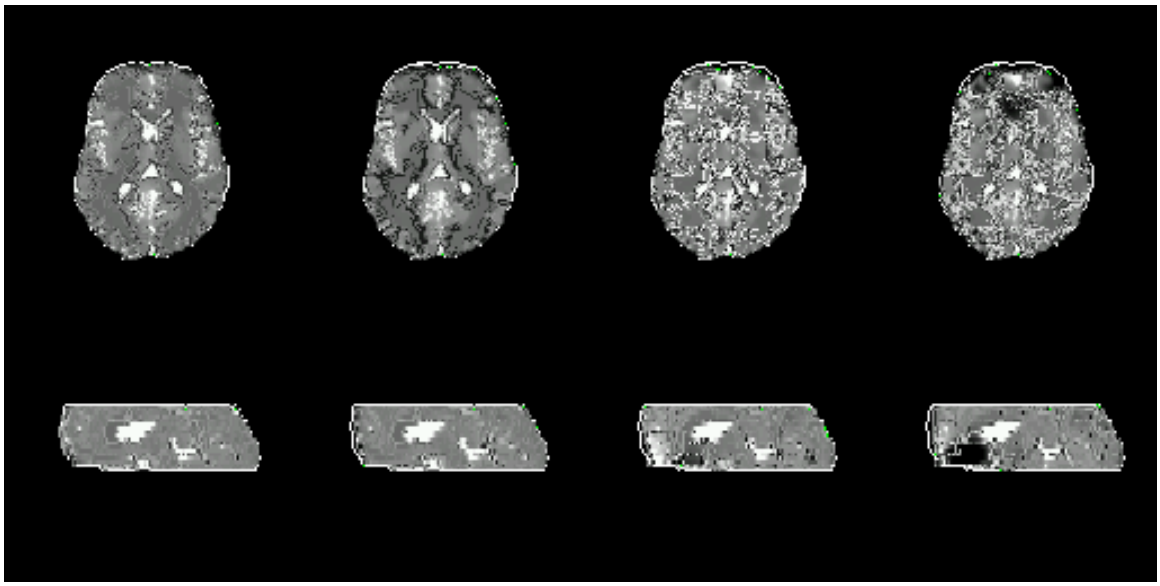

(a) (b) (c) (d)

Figure 4: Simulated brain images are shown in both axial (top) and sagittal (bottom) views. (a): Simulated distortion-free image; (b): Distorted image with geometric distortion only; (c): Distorted image with geometric distortion and the Jacobian factor; (d): Distorted image with geometric distortion, Jacobian, and dephasing.

Figure 4 shows the simulated distortion-free image and its distorted versions. The outer contour of the head is outlined in (a) and overlaid onto the other images to show the

induced distortions more clearly. Note, as shown in the figure, that only a portion of the brain is used for simulation to reduce computation time. Distortion occurs mainly in the frontal area because of the proximity of the sinuses, which produce relatively large field perturbations. Figure 4 (b) shows the distorted image with geometric distortion only. Figure 4 (c) shows the effect of distortion on SE EPI images. As the image is compressed, the intensity increases because more signal contributes to the voxels in the distorted area. In Figure 4 (d), dephasing has been introduced to simulate a GE EPI image, leading to intensity reduction in certain regions.

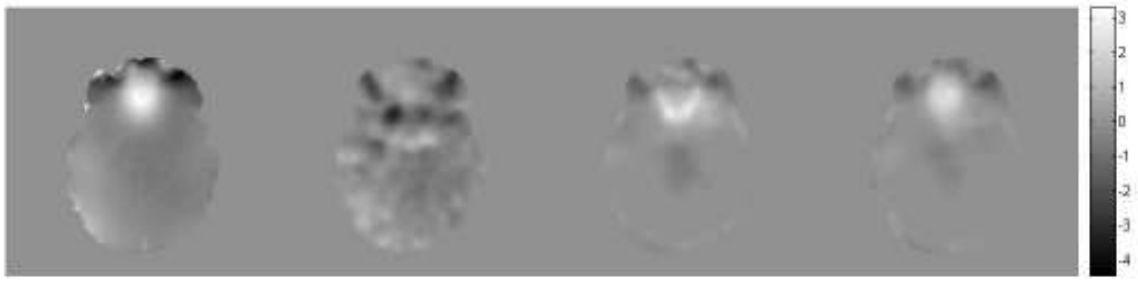

(a) (b) (c) (d)

Figure 5: (a): The distortion map (ground truth) derived from a measured field map of a human brain. (b)-(d): The deformation field obtained through unidirectional nonrigid registration: with ABA (b); with ABA-J (c); and with ABA-JRE (d).

To correct the distortions, we register the image in Figure 4 (d) to that in Figure 4 (a) using our nonrigid registration algorithm with and without Jacobian and rephasing factors. We label the original registration method ABA, the method with the Jacobian factor ABA-J, and the method with both the Jacobian and rephasing factors as ABA-JRE. Figure 5 shows the magnitude of the distortion field (ground truth) and of the deformation fields estimated through registration. Adding the Jacobian factor (Figure 5 (c)) has a clear effect on the result, but the patterns in the estimated deformation field do

not correspond to the ground truth. Introducing the rephasing factor (Figure 5 (d)) improves the results further; this is especially visible in the frontal part of the image. The corresponding distortion corrected images are shown in Figure 6 (c)-(e). Figure 6 (a) and (b) are added for comparison. As was the case in Figure 4, the outer contour is drawn on the distortion-free image and overlaid on these corrected images. These figures show that without correction factors, the nonrigid registration algorithm stretches the distorted image but intensity values in hypo- and hyper-intense areas are not corrected. The Jacobian term corrects the region of hyper-intensity (pointed by the arrow in Figure 6 (d)). The rephasing term improves the image in areas in which signal dropout can be observed (pointed by the arrow in Figure 6 (e)).

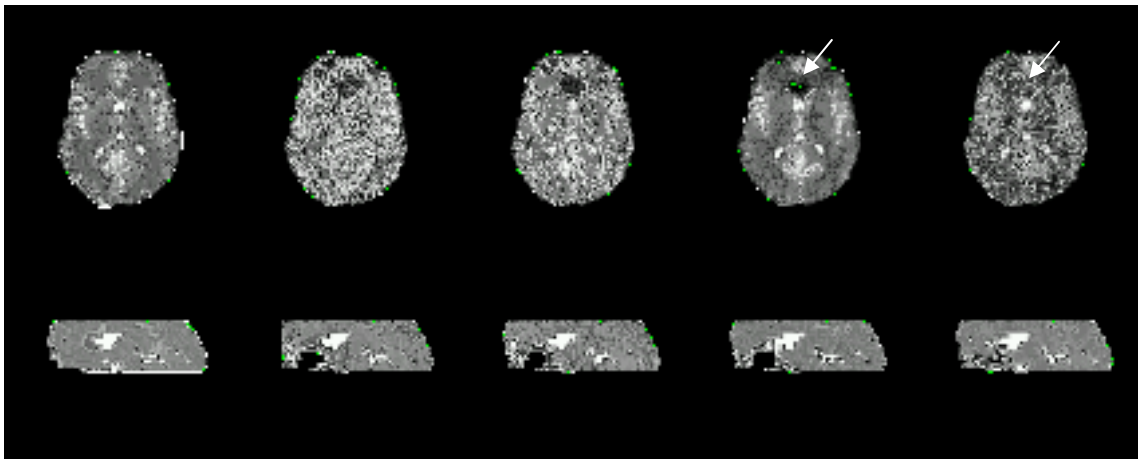

(a) (b) (c) (d) (e)

Figure 6: Images after distortion correction. (a): Simulated distortion-free image same as in Figure 1(a); (b): Simulated distorted image same as in Figure 1(d); (c)-(e): Images corrected using nonrigid registration: with ABA (c), with ABA-J (d), with ABA-JRE (e).

To evaluate the correction results quantitatively, we compute the root mean square (rms) value over each image slice of the magnitude in voxels of the difference at

each point inside the brain between the distortion field that is calculated from the field map and the deformation field that we obtain with our method. These rms values indicate the residual errors after distortion correction. The values are calculated slice by slice to show the effectiveness of the correction method on different parts of the brain. The results are plotted in Figure 7 (a). This figure shows that for the lower part of the brain (corresponding to slices 1-7), where the intravoxel dephasing effect is severe or obvious, ABA-JRE produces better results than the approach without the rephasing factor. For the upper part of the brain (corresponding to slices 8-12), where only minimal amount of dephasing effect exists, adding the rephasing factor does not change the results substantially and may even worsen them. Close inspection of the deformation field shows that for these slices adding the rephasing factor reduces accuracy some but produces deformation fields that are smoother. Figure 7 (b) shows the rms values of the intensity differences between the reference image and the EPI images before and after correction. Those values are also computed slice by slice. This figure shows that ABA-JRE produces the corrected image with intensity values that are the closest to the reference image.

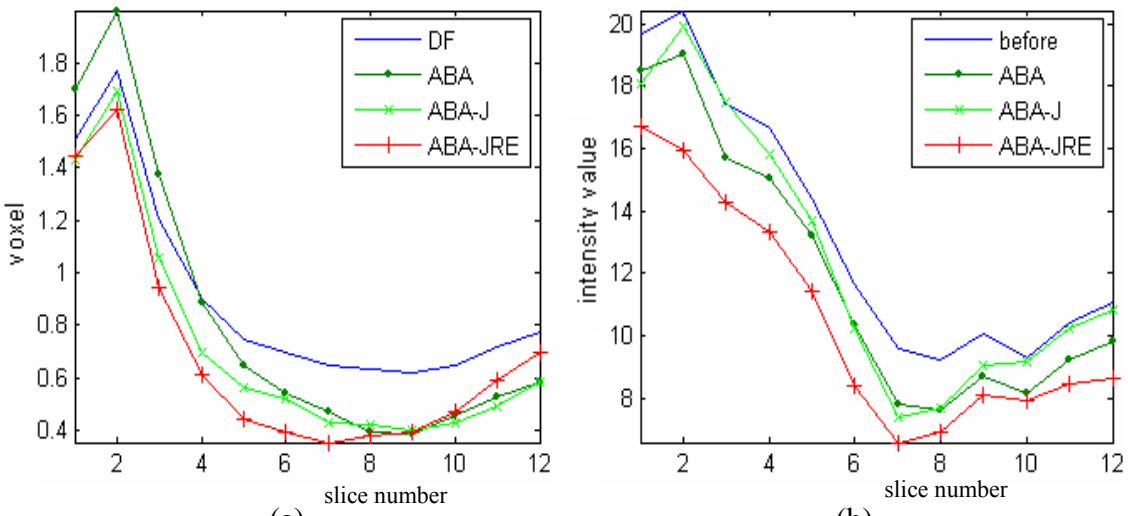

Figure 7: Root mean square value vs. slice number for (a): the original distortion field (DF) and the differences between DF and the obtained deformation fields using ABA, ABA-J and ABA-JRE methods, (b): the intensity differences between the reference image and the EPI images before and after correction using three methods.

3.2. Human brain images

Brain MRI images of 5 humans are used as subjects for the evaluation of the performance of the algorithm. For each subject, a set of GE EPI image volumes and a single, standard, multi-shot, spin-echo image volume with high in-plane resolution were acquired on a Philips 3T scanner, with SENSE enabled. The image resolution for GE EPIs is 128 x 128 (interpolated from 80x80), with 28 slices, TE 35 ms, voxel size 1.875 x 1.875 x 4.5 mm. The spin-echo volumes also have 28 slices but a 256 x 256 in plane resolution. They were downsampled to 128 x 128 to match the size of GE EPIs for registration purposes. Figure 8 (a) shows a representative slice from the spin-echo volume of a representative subject. Because it is a standard, multi-shot acquisition, its geometrical distortion is negligible; because it is a spin-echo image, there is no signal loss due to dephasing. Thus, it provides a standard for comparison. Figure 8 (b) shows a representative slice from a representative GE-EPI volume. A comparison of Figure 8 (b)

to (a) shows clearly that geometric distortion and intensity reduction are present in the frontal regions of the EPI image.

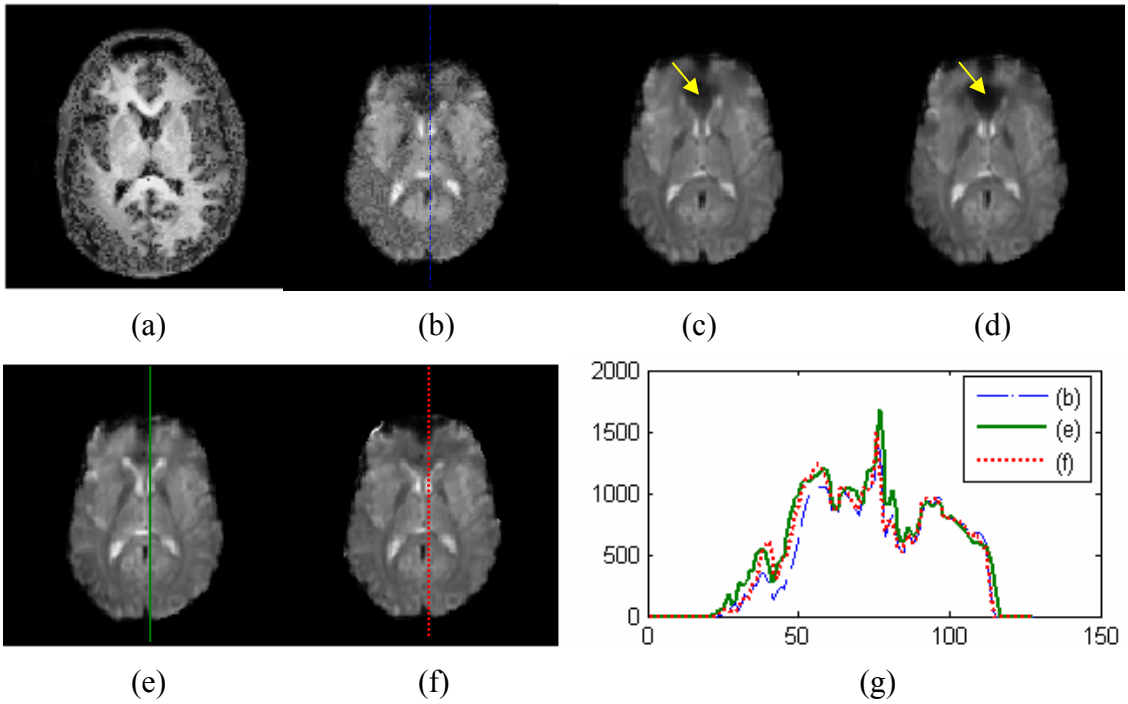

Figure 8: Images after distortion correction. (a): the spin echo anatomic image; (b): the GE EPI image; (c)-(e): Images corrected using nonrigid registration: (c) with neither the Jacobian nor dephasing factors, (d) with the Jacobian factor only, (e) with both the Jacobian and rephasing factors. (f): Image corrected using a measured field map; (g): intensity profiles along the line from top to bottom in (b), (e) and (f). Arrows in (c) and (d) point the regions where the images are inappropriately stretched and intensity attenuation is still present after registration.

We registered each of the subject's GE EPI volumes to the spin-echo volume using our proposed method to correct for geometric distortion and signal loss. For comparison, nonrigid registrations without the Jacobian factor or rephasing factor were also performed. Figure 8 (c)-(e) show the correction results for one of the subjects. In Figure 8 (c) and (d), the rephasing factor is not considered. Although the outline of the upper part of the brain is stretched when geometric distortion alone is considered, the

region in the frontal area of the brain (pointed by arrows) is inappropriately stretched and intensity attenuation is still present as before. Using the Jacobian factor as in Figure 8 (d) does not help much. When the rephasing factor is used, as in Figure 8 (e) intensity is recovered, at least partially, and the corrected image is similar to the corrected image obtained with the measured field map, which is shown in Figure 8 (f). The intensity profiles plotted in Figure 8 (g) further show that the method we propose leads to corrected images that are similar (and arguably better in the frontal part) to those obtained with a field map approach, which can be considered as the standard when the field map is available and measured accurately.

Figure 9 shows multiple slices of a GE EPI image before (a) and after (b) correction, and it highlights the strengths and remaining weaknesses of the algorithm. When signal loss is extremely severe as is the case for the images 1 to 3 in the top row, the algorithm is unable to correct the artifacts. It is unlikely that any post-acquisition algorithm will lead to satisfactory results for this type of artifact. When the signal loss is small to moderate as is the case for images 4,5,6,7, and 8 our approach leads to satisfactory results. Figure 10 shows one slice in each of the other four volumes we have used to test our algorithm. It can be seen that intensity reduction, especially in the region just anterior to the ventricle, has been corrected after applying the proposed method.

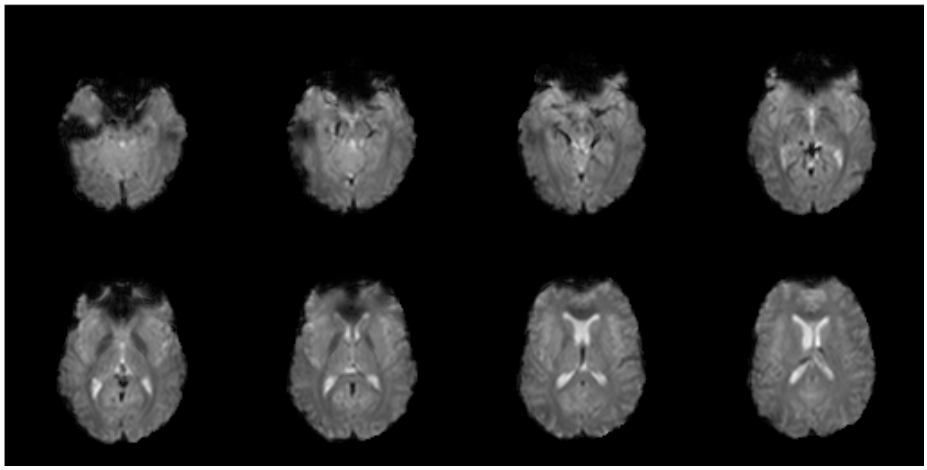

(a)

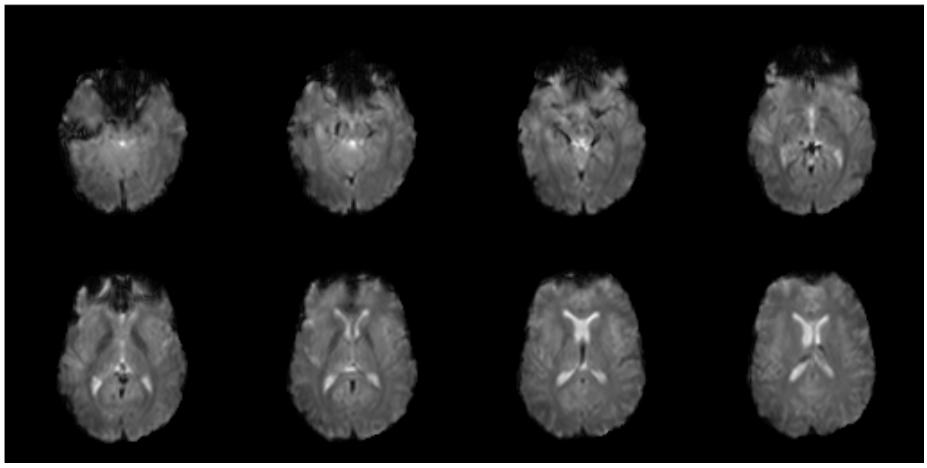

(b)

Figure 9: Multiple slices of an EPI image before (a) and after (b) correction using the proposed method. The slices are numbered as 1 to 8, starting from left to right and then top to bottom.

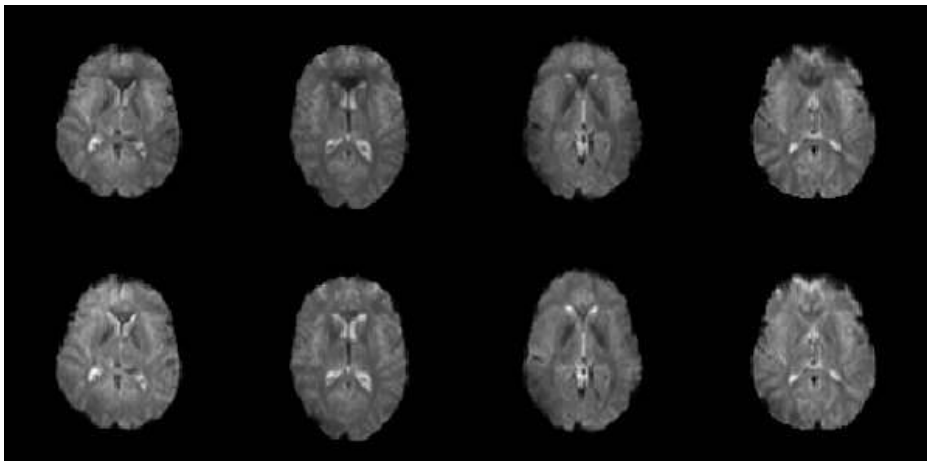

Figure 10: Correction results from other four datasets. Top row: before distortion correction, bottom row: after distortion correction.

4. Discussion

We have proposed a new approach for retrospective correction of the geometric distortions and signal loss in GE EPI images. An intensity-based multimodal nonrigid registration is used for this purpose. A rephasing factor is added as a novel component in the similarity measure and used to correct for the signal loss artifact observed in GE EPI but not SE EPI. We have shown that introducing such a factor derived from the physics of MR imaging enhances the registration process. Not only does it help in correcting the images geometrically but it also permits the correction of intensity values. This may have a positive impact on the analysis of these images and improve, for instance, the detection and localization of activation regions in fMRI studies.

As our results have shown, our method improves the results but is not capable of correcting the images completely. In areas in which signal loss is very severe, it is unlikely that any intensity-based or even a method based on field maps, would be able to recover the signal. In areas in which signal loss is moderate, our method leads to results

that are qualitatively similar to those obtained with a field map approach. Assessing quantitatively which of these method leads to more accurate results is difficult. Our method is prone to errors related to local minima and accuracy of numerical methods for the computation of the gradients. Methods based on field maps are sensitive to errors related to phase unwrapping and motion. The later is of particular importance for long acquisition sessions. A field map acquired at the beginning of the study may not be registered to an image volume acquired during the study. As discussed in [1], [17], simply registering the field map to a volume is not sufficient, and in order to avoid this misregistration problem, many field maps must be acquired during the study, each requiring two additional volume acquisitions. Acquiring a field map takes several seconds (in EPI space, as in [17]) or a few minutes (in non-EPI space as in [18]), and these additional acquisitions may result in an unacceptable reduction in the temporal resolution of the study. The time needed for the method we propose depends on the size of the image and the number of basis functions used to model the distortion field, but it does not affect acquisition time. For the real brain images presented in this study, a typical registration takes between 8 and 9 minutes on a PC with a 3G Hz CPU and 1GB of RAM. If time between acquisition and analysis is critical, such an approach may not be practical. If, however, correction of the images can be done independently of the analysis of the images or when a field map is not available, our method provides a solution. Although it is outside the scope of this work, the comparison of activation maps obtained after geometric and intensity correction with a field-map approach and with our method would be a valuable extension to this work.

The Jacobian and rephasing factors need to be estimated for correcting intensity distortions. This requires the computation of the spatial derivative of the field map, which is approximated here by a deformation field. Approximation errors often exist due to imperfect registration or missing information in distorted images. The errors will typically be accentuated when the derivatives are computed. This, in turn, will affect the registration process. It is especially true for the rephasing factor because it is proportional to the reciprocal of a small number that is calculated using the gradient of the deformation field. In areas where the signal-to-noise ratio (SNR) is low, the accurate estimation of the corresponding deformation field is more difficult. This may lead to inaccurate correction factors, which may deteriorate the images further rather than enhancing them. Also, as the results have shown, correction of the images where signal attenuation is very severe remains imperfect. This suggests developing methods that can automatically identify regions over which the algorithm is likely to succeed and regions over which it may not.

In this chapter, we discussed a correction method that is designed for GE EPI images by introducing an intensity correction factor. In the next chapter we will propose an approach in which the characteristic of the geometric distortion in EPI images is taken into consideration.

CHAPTER IV

NONRIGID REGISTRATION WITH SPATIALLY VARYING SCALE OF DEFORMATIONS: APPLICATION TO GEOMETRIC DISTORTION CORRECTION IN ECHO PLANAR IMAGES

1. Introduction

As mentioned in Section 3, Chapter II, nonrigid registration-based methods have been used to correct for the distortions in EPI images [22]-[27]. Because these methods often rely on deformations with a very large number of degrees of freedom, their regularization is of great importance for their accuracy, robustness, and speed. In Section 4, Chapter II, various techniques used to regularize the deformation field have been introduced. They can be categorized into two groups: uniform and adaptive. Among the latter approach, the adaptive placement of basis functions or control points have been used in some registration algorithms by means of the detection of mismatched regions in advance, such as in [40], [56], [57]. While such adaptive methods reduce the optimization complexity, the detection of mismatched or active regions is typically done at the same scale over the entire image. This not only is time consuming but also assumes that the properties of the transformation do not change spatially. This assumption may lead to spurious local displacements due to local optima in regions in which the deformation field ought to be smooth and regular. The use of prior knowledge to constrain the deformation fields may help to alleviate the problem.

Recently, Pekar *et al.* [91] propose a method in which the scale of the transformation is adapted spatially. They apply Gaussian-shaped forces at control points and use a PDE (Navier equation) to model the connection between the forces and the

resulting deformation field. The influence areas of the forces, i.e. the Gaussian width σ, are adjusted automatically together with their strengths and the positions of the control points during the optimization. While, as claimed by the authors, the method can achieve similar results by using less control points than registration methods based on regular grids, the optimization complexity is increased because the position of the control points are additional free parameters. Also, a priori information about the deformation field is not considered in their method.

In this chapter, we propose an approach to integrate a priori information into our registration algorithm. We introduce a scale map into the algorithm to specify the support size of the basis functions to be used over the various regions of the image. We also present a method to compute the scale map from a priori information, namely, an estimate of the expected deformation field. Knowledge of the physical processes that induce distortion in the EPI images is used to calculate this estimate. The proposed approach is applied to both simulated and real images. The remainder of the chapter is organized as follows. Section 2 presents our approach in detail. Section 3 describes the distortions in EPI images and ways by which the estimated deformation field can be created. Experiments on simulated and real data are presented in Section 4. Finally, conclusions are drawn in Section 5.

2. Nonrigid Registration with Spatially Varying Scale

Our approach is based on a previously proposed nonrigid registration method—the Adaptive Bases Algorithm (ABA) [43]. The main steps in our approach are shown in Figure 11. The computation of a scale map and the way to use it in the ABA method are

presented in this section. The approach we use to estimate an expected distortion field is described in the next section.

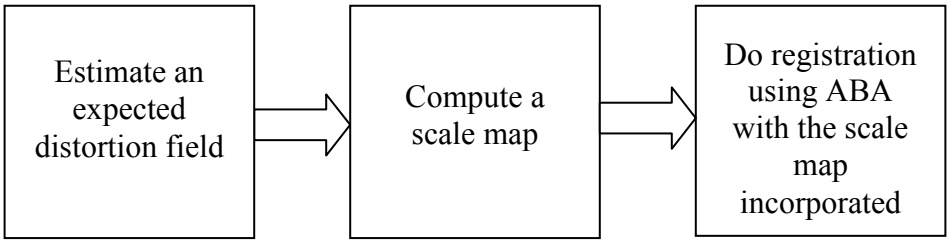

Figure 11: A flow chart for our approach.

2.1. Revisit of the ABA method

The ABA method has been described in Chapter III. Here we rewrite the equation that models the deformation field, $\mathbf{D}(\mathbf{x})$, :

$$\mathbf{D}(\mathbf{x}) \equiv \mathbf{x}' - \mathbf{x} = \sum_{i=1}^{n} \mathbf{c}_i \phi\left(\frac{\|\mathbf{x} - \mathbf{x}_i\|}{s}\right) \tag{28}$$

where s is the support size of the basis function. During the registration, a multilevel approach is performed by progressively changing the resolution of the images and the support size of the basis functions. A particular combination of image resolution and basis function density is called a "level". In this algorithm, the support size of the basis functions is inversely proportional to their density, i.e. when the density increases by some factor, the size of the support decreases by that same factor. In the application described in this paper, in order to focus our experiments on the effects of the scale of deformation, we use only one image resolution. Thus, only the density of basis functions varies with level.

2.2. $\mathbf{d}_{\text{final}}$ and scale map

In the ABA method, the scale of the transformation is controlled by the density of basis functions at the final level, which we call $\mathbf{d}_{\text{final}}$, which is a 1 x 3 vector containing the densities in the x, y, and z directions. When $\mathbf{d}_{\text{final}}$ is low for a given region, few basis functions with a large support size are used, which leads to transformations that are smooth and regular everywhere within the region. On the other hand, a high $\mathbf{d}_{\text{final}}$ permits the modeling of highly local deformations with a large number of degrees of freedom. Such a model allows almost arbitrary deformations, corresponding to a weak regularization. Hence, $\mathbf{d}_{\text{final}}$ can be viewed as a regularization factor which determines the scale of a deformation field. To adjust $\mathbf{d}_{\text{final}}$ spatially, a scale map S, which is a volume that has the same size as the image, is introduced into the ABA algorithm as a new component. According to S, a higher $\mathbf{d}_{\text{final}}$ is assigned to the regions where we anticipate rapid variations in the deformation field, and a lower $\mathbf{d}_{\text{final}}$ is assigned to regions where slow variations are expected. In a multi-level approach, all the levels up to the pre-specified $\mathbf{d}_{\text{final}}$'s are used for the regions with different scales in the registration. The method we use to generate S is described in the following part.

2.3. Generation of scale map

Based on a priori information about the expected deformation field, a number of strategies can be used to generate a scale map. One could assign manually a scale to a given location in the scale map, but this requires the scale information for each location to be known a priori. We use this approach in the experiments described in Section 4.1. When such information is not available a priori, it needs to be computed. One solution, in

this case, is to use an estimated deformation field and to extract scale information from that field. The estimated field can be derived from a deformation field computed from a large population, as in [59] and [77], or it can be generated using knowledge about the problem at hand, which is the approach we follow in this work. Here, we present a technique to compute a scale map from an estimated deformation field. The generation of this field is based on knowledge about the physics of EPI, which is described in Section 3.

To compute a scale map of a given deformation field, we first need to determine areas in the field that are smooth and slowly varying and areas in which changes are faster. The approach we use to do this is similar to the multilevel scheme we use in the ABA algorithm. We use as many levels as in the registration algorithm and we use the same number of RBFs in each level. During the optimization, because the deformation field is known, the optimization process in the registration method is replaced by a least squares approximation. Conceptually, we fit the field, first with a few basis functions with large support, then with more and more basis functions with smaller and smaller support. If the field changes slowly, the fitting is good enough with few basis functions. When the field changes rapidly, more basis functions are necessary. Practically, we store in an array $\boldsymbol{\Theta} = [(N_{x1}, N_{y1}, N_{z1}), (N_{x2}, N_{y2}, N_{z2}), \cdots (N_{xn}, N_{yn}, N_{zn})]$ the numbers of basis functions we use in the x, y, and z directions at each iteration. The density of basis functions corresponding to level j is then $\mathbf{d}(j) = \boldsymbol{\Theta}[j]/\mathbf{V} = (N_{xj}/v_x, N_{yj}/v_y, N_{zj}/v_z)$, where $\mathbf{V} = (v_x, v_y, v_z)$ is the size of the image in the x, y, and z directions. The values in each direction increase monotonically from the beginning to the end of the array. Here, n, the length of $\boldsymbol{\Theta}$, is the number of iterations we use when fitting the field. Given a deformation field $\mathbf{D}_0$, we do the following at the m^{th} iteration:

Step 1: Set the current deformation field, $\mathbf{D}_{\text{current}}(\mathbf{x}, m)$, as the residual deformation field obtained from the previous iteration $\mathbf{D}_{\text{residual}}(\mathbf{x}, m-1)$, i.e.

$$\begin{aligned} \mathbf{D}_{\text{current}}(\mathbf{x}, m) &= \mathbf{D}_{\text{residual}}(\mathbf{x}, m-1) \\ \mathbf{D}_{\text{residual}}(\mathbf{x}, 0) &= \mathbf{D}_0(\mathbf{x}) \end{aligned}. \tag{29}$$

Step 2: Use RBFs at level m (i.e. with total number $N_m = N_{xm} \times N_{ym} \times N_{zm}$) to approximate $\mathbf{D}_{\text{current}}(\mathbf{x}, m)$ with a least-squares approach. A new residual deformation field $\mathbf{D}_{\text{residual}}(\mathbf{x}, m)$ is computed as:

$$\mathbf{D}_{\text{residual}}(\mathbf{x}, m) = \min_{\mathbf{C}(\Omega)} \sum_{\mathbf{x} \in \Omega} \left[\sum_{j=1}^{N_m} \mathbf{c}_j \Phi\left(\left\| \mathbf{x} - \mathbf{x}_{j,m} \right\| \right) - \mathbf{D}_{\text{current}}(\mathbf{x}, m) \right]^2 \tag{30}$$

where Ω represents the entire image space, and $\mathbf{x}_{j,m}$ is the spatial location of the j^{th} basis function at level m, and $\mathbf{c}_j \in \mathbf{C}(\Omega)$ is the coefficient of the j^{th} basis functions.

After all $\mathbf{D}_{\text{residual}}(\mathbf{x}, m), 1 \le m \le n$ are obtained, the scale map can be computed by selecting a number of scales and thresholding the corresponding $\mathbf{D}_{\text{residual}}$. One could use as many scales as entries in the $\boldsymbol{\Theta}$ array. But, this would be impractical. Often the nature of the problem dictates the number of scales to be used. For instance, in the application described herein, two scales, named low scale and high scale, are used to model the deformation field (see Section 3.2 for details). We then empirically decide the density of basis functions that define the low and the high scale. $\mathbf{d}(3)$ could, for instance, specify the density of basis functions we want to use to model the field at the low scale. We examine the value in $\mathbf{D}_{\text{residual}}(\mathbf{x}, 3)$ after $\boldsymbol{\Theta}(3)$ basis functions are used in the fitting. Areas in $\mathbf{D}_{\text{residual}}(\mathbf{x}, 3)$ for which the value is below a threshold is considered to be approximated

well by using basis functions with density up to $\mathbf{d}(3)$. And the corresponding areas in the scale map *S* are then labeled as low scale and assigned the value 3. The other areas are labeled as high scale and assigned the value *n*. When registering the images, we use the same array $\boldsymbol{\Theta}$ to specify the density of the basis functions used at each level. Following our example, $\mathbf{d}_{\text{final}}$ will be set to $\mathbf{d}(3)$ in the low scale areas and to $\mathbf{d}(n)$ in the high scale areas. This instructs the registration algorithm to use basis functions with densities up to $\mathbf{d}(3)$ in the low scale areas and up to $\mathbf{d}(n)$ in the high scale areas.

Note that we use "iteration" only in describing our method for generation of the scale map. The RBF level advances one during each iteration. The Selection of scales in the scale map performs only once after all iterations end.

2.4. Algorithm overview

Our algorithm is summarized as follows:

1. Choose a RBF array $\boldsymbol{\Theta}$ with length *n* and select *K* scales of interest (in our current application, *K*=2)
2. Generate $\mathbf{D}_0$, an estimate of the expected deformation field.
3. Compute a scale map *S* via the iterative method described above. Define scale regions R_k, $1 \le k \le K$, as the union of the locations at which the scale values are equal to s_k.
4. For *j* = 1 to *n*
    a. For *k* = 1 to *K*

        If $j \le s_k$, place basis functions in region R_k with density $\mathbf{d}(j)$.

    End For

b. Identify the basis functions which cover mismatched areas according to the gradients of the similarity measure with respect to the coefficients of the basis functions.

c. Optimize the coefficients of the basis functions in the mismatched areas.

End For

3. A priori Information about Distortions in EPI Images

3.1. Distortions in EPI images

As mention in Section 2.2, Chapter III, it is known that geometric distortion in EPI images in the presence of an inhomogeneous main magnetic (B_0) field is directed almost exclusively along the phase encoding direction (here the y direction). The displacement at location (x, y, z) is rewritten here as:

$$\mathbf{D}(x, y, z) = [0 \quad \Delta y(x, y, z) \quad 0]^T \tag{31}$$

where $\Delta y(x, y, z)$ is the geometric distortion at the original position (x, y, z) and is calculated by:

$$\Delta y(x, y, z) = \gamma \Delta B(x, y, z) \mathrm{FOV}_y / \mathrm{BW}_y \ . \tag{32}$$

Here, γ is the gyromagnetic ratio, ΔB is the perturbation of the B_0 field, and FOV_y and BW_y are the Field of View and bandwidth in the phase encoding direction, respectively.

The Jacobian factor has been derived in Eq. (13) in Chapter III and is rewritten here:

$$J^{-1}(x, y, z) = \left(1 + \partial \Delta y(x, y, z) / \partial y\right)^{-1}. \tag{33}$$

Additionally, for Gradient Echo (GE) EPI images, the dephasing factor has been derived in Eq. (21) in Chapter III and is rewritten here:

$$h(x, y, z) = \left|\mathrm{sinc}\left(\pi \gamma v_z t_{\mathrm{TE}} \left(\partial \Delta B(x, y, z) / \partial z\right)\right)\right| \tag{34}$$

with v_z the voxel size of the EPI image in the z direction and t_{TE} the echo time. From Eqs. (32) - (34), the distortion model in EPI images can be written as:

$$i(x, y + \Delta y, z) = i_0(x, y, z) \cdot J^{-1} \tag{35}$$

or

$$i(x, y + \Delta y, z) = i_0(x, y, z) \cdot J^{-1} \cdot h\,. \tag{36}$$

Here, i and i_0 are images with and without distortions, respectively. Eq. (35) holds for Spin Echo (SE) EPI images, which have no signal loss caused by intra-voxel dephasing effect, and Eq. (36) holds for GE EPI images. They have been used in registration based distortion correction methods for SE EPI images [22] and GE EPI images [78], respectively.

3.2. Characteristics of the geometric distortion

According to Eq. (32), the amount of geometric distortion is proportional to the amplitude of the B_0 field inhomogeneity ΔB. Such inhomogeneity is induced mainly by the magnetic susceptibility differences between substances within the subject inside the scanner. In this work we focus on the EPI images for human brain. In the brain, there exist mainly two substances which have very different susceptibility: air and water (i.e. soft tissue). The magnitude of the distortion typically changes smoothly in the areas inside the brain but dramatically at the interfaces between air and tissue. Because of this, we classify the existing geometric distortions as one of two types: low or high.

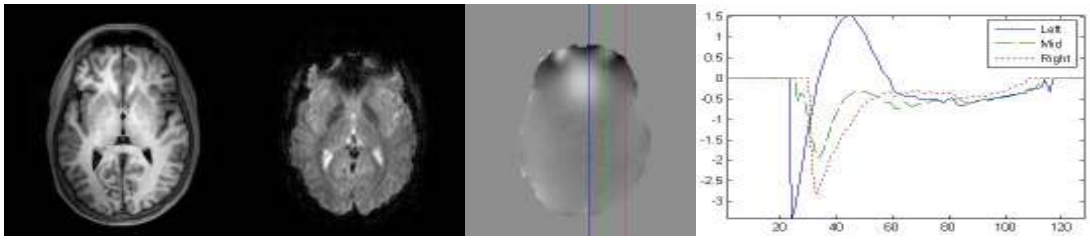

(a) (b) (c) (d)

Figure 12: Anatomic image (a) and EPI image (b) of a subject are shown. (c) is the corresponding geometric distortion map. Profiles of distortion in units of voxels in the phase encoding direction in (c) are shown in (d). The positive horizontal direction in (d) corresponds to the downward direction in (c) in voxels.

An example of the geometric distortion that can be observed in a real EPI image is illustrated in Figure 12. Figure 12 (a) is one slice of a high-resolution, multi-shot image volume. We call this image an "anatomic image" because of the anatomical detail it shows, and we note that geometrical distortion is negligible throughout this volume because of the multi-shot protocol used in its acquisition. Figure 12 (b) is an EPI image of the same subject. Figure 12 (c) is the corresponding geometric distortion map for the

EPI protocol derived from a measured field map via Eq. (32). Profiles along the phase encoding direction, which is vertical in Figure 12 (c), are shown in Figure 12 (d) to demonstrate various types of changes across the image. By comparing the values in the three different plots in Figure 12 (d), it can be seen that a large amount of variation is present in the frontal area of the brain (from the 20th to the 60th pixel, where numbers increase downward), whereas the changes are substantially smaller inside the brain (from the 60th to 110th pixel).

3.3. Estimation of the distortion field in EPI images

As described in Section 2.3, we calculate a scale map based on $\mathbf{D}_0(x,y,z)$, an estimate of the expected deformation field. In our application, $\mathbf{D}_0(x,y,z)$ can be generated based on knowledge of the physical phenomena affecting the images, as discussed above. To generate $\mathbf{D}_0(x,y,z)$, we segment the anatomic image of a subject into air and water using a simple thresholding method. The threshold in this method is selected based on the histogram of the image. The obtained binary image is further processed by morphological 'dilate' and 'erode' operations to remove small gaps or speckles. A water/air susceptibility map is created based on this binary image and then convolved with a kernel to generate a simulated field map using the method described in [64]. A distortion field at each location (x,y,z) is computed from this field map and used as the y component of $\mathbf{D}_0(x,y,z)$, which is 0 in the x and the z components, as shown in Eq. (31). Note that accurate simulation of the field map is a complicated task in itself [64], [79], [80], and it requires precise head models. To initiate our scale map calculation, however, we need only a rough approximation. More specifically, the estimated deformation field is

expected to have variations similar to those of the real one, but the amplitude of the estimated deformation field at each location does not need to be accurate.

4. Experiments and Results

In this section we describe experiments in which we evaluate our method and show how it compares to our previous approach in which a uniform scale is used, which we call the "fixed scale" approach. First we apply the proposed approach to 2D images with known deformations and known scale information to demonstrate the importance of varying the scale spatially. Then, we apply it to both simulated and real 3D EPI images, which contain geometric and intensity distortions. The smoothness, accuracy, and running time of the algorithm with and without spatial scale adaptation are compared.

4.1. Experiments with 2D MR data

In this section, a pair of 2D MR images is used to illustrate the workings of the method and to demonstrate the importance of spatial scale adaptation. A 128 x 128 T1-weighted brain image is used as the source image. It is then deformed with a known deformation field D_{test} to generate the target image. The source and target images are shown in Figure 13 (a) and (b). To create D_{test} with known scales, a real deformation field is first computed from a measured field map for the same subject, see Figure 13 (c). This field is then approximated twice with basis functions placed on an 18 x 18 regular grid and on a 10 x 10 regular grid, respectively, to create two approximations. The first one permits modeling changes at a higher scale than the second. The upper half of the first approximation and the bottom half of the second approximation are then combined to

create D_{test}, see Figure 13 (d). D_{test} is thus the deformation field we need to recover through registration of the source and target images.

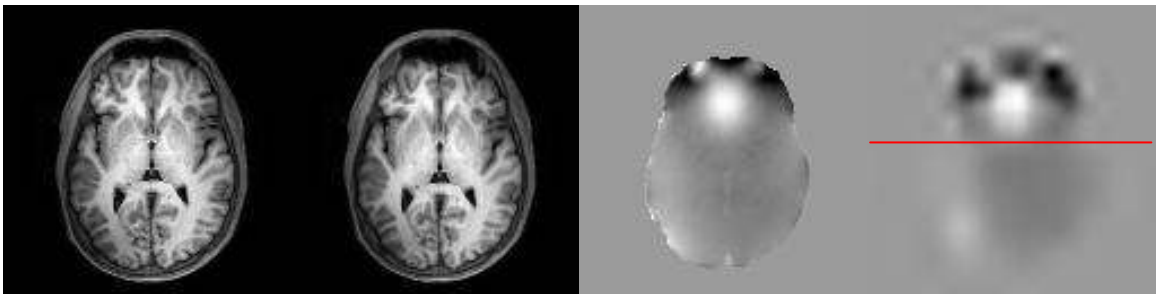

(a) (b) (c) (d)

Figure 13: (a): Source image, (b): target image, (c): a real deformation field from which D_{test} is computed, (d): D_{test} with high scale in the upper part and low scale in the low part (separated by the red line).

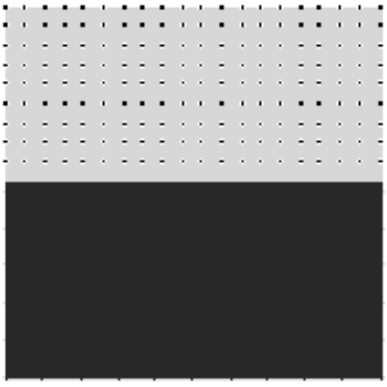

Figure 14: Scale map and placement of basis functions.

In this example, the scale of the transformation is known. Rather than estimating it, we manually specify a scale map with two scales: high scale in the upper half and low scale in the lower half. The RBF density corresponding to the high scale is (20/128, 20/128) in the x and y directions and that corresponding to low scale is (11/128, 11/128).

The scale map and the location at which basis functions are placed are illustrated in Figure 14.

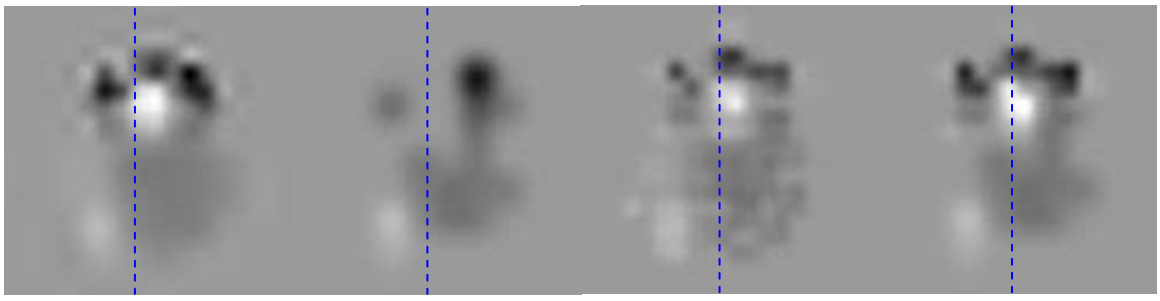

(a) (b) (c) (d)

Figure 15: D_{test} (a) and deformation fields obtained with different approaches: (b) low scale, (c) high scale, (d) spatially varying scale. Dashed lines show the location of the profiles in Figure 16.

Figure 15 shows D_{test} (a) and the deformation fields obtained with the nonrigid registration algorithm using different scales (b)-(d). Figure 15 (b) shows the estimated deformation field when a low scale is used everywhere in the image; Figure 15 (c) and (d) show the same when a high scale and a spatially varying scale are used, respectively. The Sum of Squared Differences (SSD) between D_{test} and each of the estimated distortion fields are 69.9, 53.4 and 42.3 pixels respectively. The displacement along the vertical dashed lines drawn in each of the panels is plotted in Figure 16. These results illustrate the advantage of using a priori information on the type of displacement that can be expected in a region and of adjusting the scale of the transformation accordingly. Figure 15 (b) shows that a low scale is insufficient to estimate the top part of the deformation field. It may be surprising that using high scale in both regions produces a distortion estimate that is inferior to that obtained when using spatially varying scale. However, as Figure 16 shows, using a uniformly high scale leads to oscillations in the low scale region

because of local minima (using a high scale value increases the number of degrees of freedom in the transformation and therefore the complexity of the optimization problem). The best result is obtained when the scale is varied spatially.

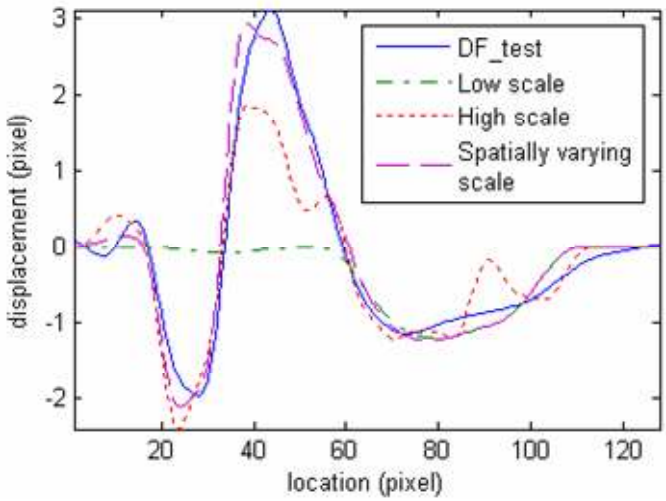

Figure 16: Plots of the displacement changes along the dashed lines shown in Figure 15. Here, the positive horizontal direction corresponds to the downward direction in Figure 15 (a)-(d) in voxels.

4.2. Experiments with 3D simulated and real EPI images

4.2.1. Parameters for the scale map

In the set of experiments conducted with both simulated and real EPI images, we experimentally choose a RBF array Θ with 6 levels to compute the scale map. The same Θ is also used in our registration process. We select the 4^{th} and the 6^{th} RBF densities (i.e. $\mathbf{d}(4)$ and $\mathbf{d}(6)$) as the $\mathbf{d}_{final}$'s for the low and the high scales, respectively. Figure 17 shows an example of a given deformation field (a) and the corresponding scale map (b) obtained with these parameters. As expected, the low scale region mainly corresponds to area inside the brain while most of the high scale region is located in the frontal part of the

image, close to the sinuses. Note that for simulated EPI images, we compute each scale map from the deformation field derived from a measured field map; for real EPI images, we compute each scale map using an estimate of the distortion field obtained with the method described in Section 3.3.

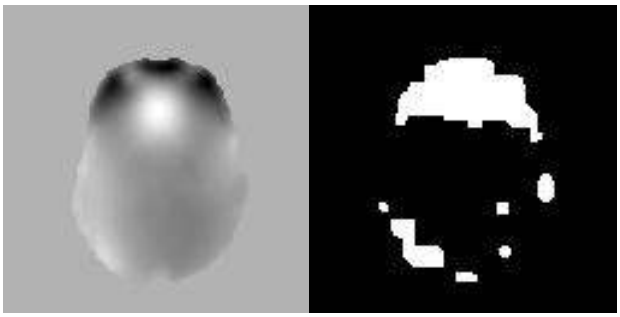

(a) (b)

Figure 17: (a): Distortion field; (b): scale map with low scale in the black area and high scale in the white areas.

4.2.2. Simulated GE EPI images

In this section, simulated GE EPI images are used to evaluate the proposed method. A 256 × 256 × 28 T1-weighted head image volume of each of six subjects is acquired using a Philips 3T MR scanner. A field map for each of the subjects is also acquired during the same study from the phase difference between two Fast Field Echo (FFE, gradient echo) scans collected at differing echo times. The field map has the same dimensions and voxel size as the T1-weighted image. Using our MR simulator [64], six distortion-free EPI volumes (size 128 × 128 × 12) corresponding to the six subjects are generated. The input to the simulator consists of three tissue volumes: white matter, gray matter, and CSF, which are segmented from each of the six T1-weighted images. Figure 18 (a) shows a typical slice in a distortion-free image volume.

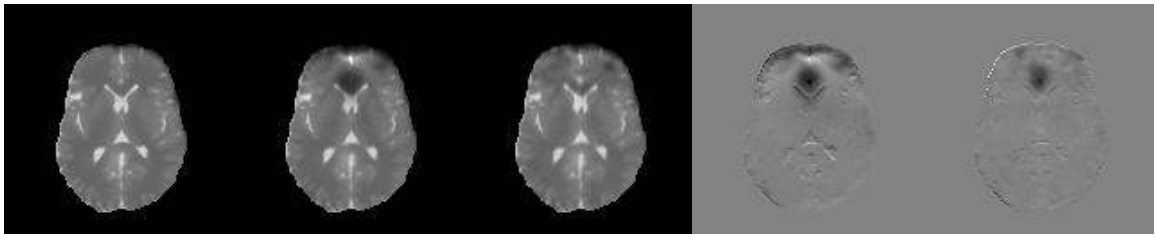

(a) (b) (c) (d) (e)

Figure 18: (a): Simulated distortion-free EPI image; (b): distorted version of (a); (c): corrected version of (b) using the proposed method; (d): difference image: (b)-(a); (e): difference image: (c)-(a).

We then use these reference images and the measured field maps to create six simulated EPI images with geometric distortion and modified intensity values according to Eq. (36). The distorted version of Figure 18 (a) is shown in Figure 18 (b). The geometric distortions computed from the field maps are used as the ground truth to which the deformation fields obtained with our method are compared. The distortion model given in Eq. (36) is included in our registration method as described in [78]. The registrations are performed using three approaches: fixed low scale (i.e. use level 1-4 in Θ everywhere), fixed high scale (i.e. use level 1-6 in Θ everywhere) and spatially varying scales (i.e. a scale map with value 4 and 6). Figure 18 (c) shows the image in Figure 18 (b) after it has been corrected with our spatially varying scale approach. Figure 18 (d) and (e) are the intensity differences, (b)-(a) and (c)-(a), respectively; these show a substantial reduction in both geometric and intensity distortions after correction.

Figure 19 compares the residual errors, inside the low scale region (a) and the high scale region (b), of the deformation fields estimated with both the fixed low scale and the fixed high scale approaches. The errors are computed as the mean absolute

difference (MAD) between the estimated deformation fields and the ground truth. It can be seen that in the low scale region increasing the density of the basis functions does not substantially affect accuracy. However, increasing their density improves accuracy in the high scale region. Although using radial basis functions with high density everywhere in the image may appear to be a solution, it is not ideal. There are indeed several disadvantages in using high density when it is known to be unnecessary. First, computation time increases. Second, the algorithm may over fit the data. As will be shown in the next section in which real images are used, using too many degrees of freedom in regions where it is not needed leads to deformation fields that are not as smooth as what would be expected from our knowledge of the physical process (this problem is not as apparent with the simulated images we use in this section because they are themselves smoother than the real ones).

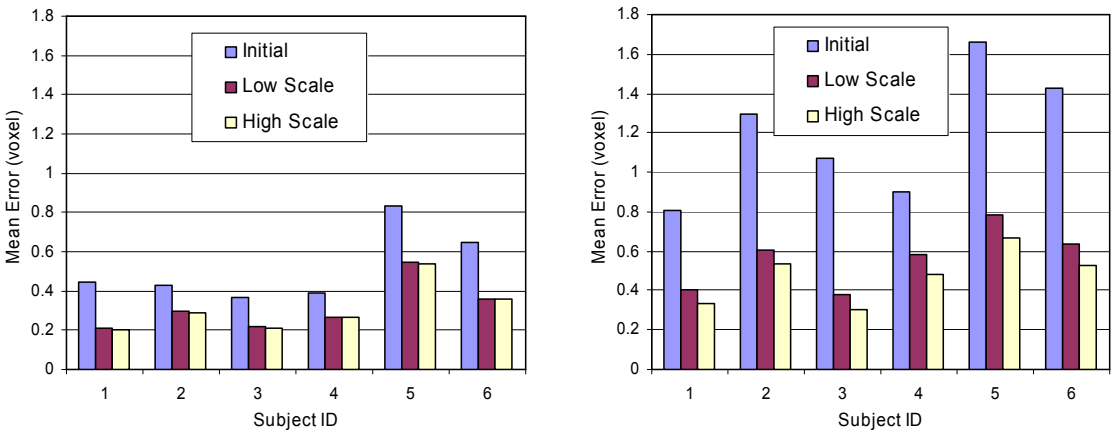

Figure 19: Initial displacement and residual errors for 3D simulated images inside the low scale region (a) and the high scale region (b) using the fixed low scale and the fixed high scale approaches.

Figure 20 shows the residual errors over the entire deformation field when the fixed high scale and the spatially varying scale approaches are used. These results show that, with the data used in this section, the spatially varying scale approach leads to an accuracy that is comparable to the fixed high scale approach. However, as shown in Table 1, it does it in a fraction of the time.

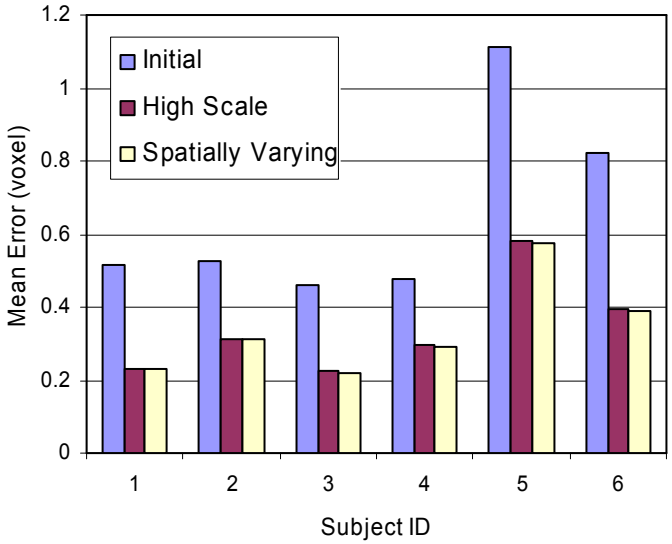

Figure 20: Initial displacement and residual errors for 3D simulated images over the entire deformation field using the fixed high scale and the spatially varying scale approaches.

Table 1: Registration times for 3D simulated EPI images (min).

Subject ID	1	2	3	4	5	6
High Scale	5.03	3.75	3.63	3.38	4.87	4.68
Spatially Varying Scale	3.20	2.12	2.10	2.03	3.45	3.05
Time Reduction	36%	43%	42%	40%	29%	35%

4.2.3. Real GE EPI images

In this section, the spatially varying scale scheme is evaluated with real GE EPI images of six subjects. For each subject, a set of GE EPI images and a single high-resolution, multi-shot, spin-echo anatomic image are acquired on a Philips 3T scanner. The image resolution for the GE EPIs is 128 × 128 (interpolated from 80 × 80), with 12 slices, TE 35 ms, voxel size 1.875 × 1.875 × 4.5 mm, with 0.4mm gap. The anatomic images have the same number of slices as the GE EPIs but have 256 × 256 in-plane resolution. They are downsampled to 128 × 128 for registration purpose. See Figure 21 (a) and (b) for an example. Note that the non-brain tissue in each image is removed using a brain extraction tool [70]. As can be seen, the geometric distortion and intensity attenuation are present mainly in the frontal regions of the brain. Each GE EPI image is registered to its corresponding anatomic image using the proposed method to correct for geometric distortion and signal loss.

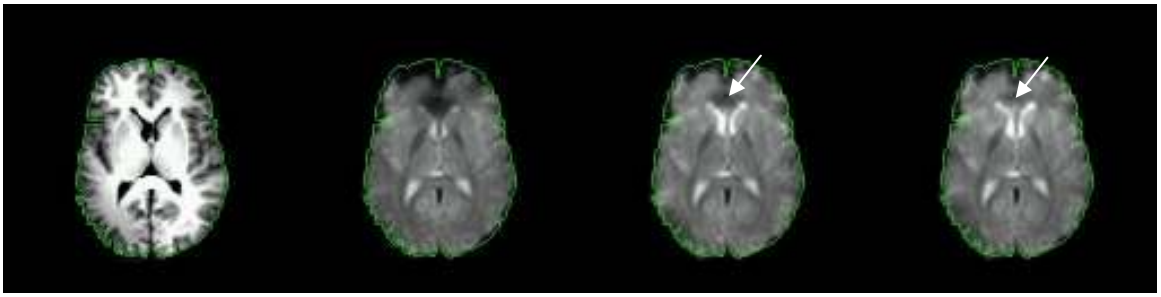

(a) (b) (c) (d)

Figure 21: (a): anatomic image; (b): EPI image; (c) and (d): corrected images using nonrigid registration with fixed scale (c) and spatially varying scale (d). More signal recovery is apparent in some places (arrow) with spatially varying scale.

Figure 21 (c) and (d) show the images after correction using nonrigid registration methods with fixed (high) scale and spatially varying scale, respectively. The iso-

intensity contour of the brain is outlined in (a) and overlaid onto the other images. Both approaches lead to similar results albeit the spatially varying scale method seems able to recover more signal in the area above the ventricles (shown with white arrows in the figure).

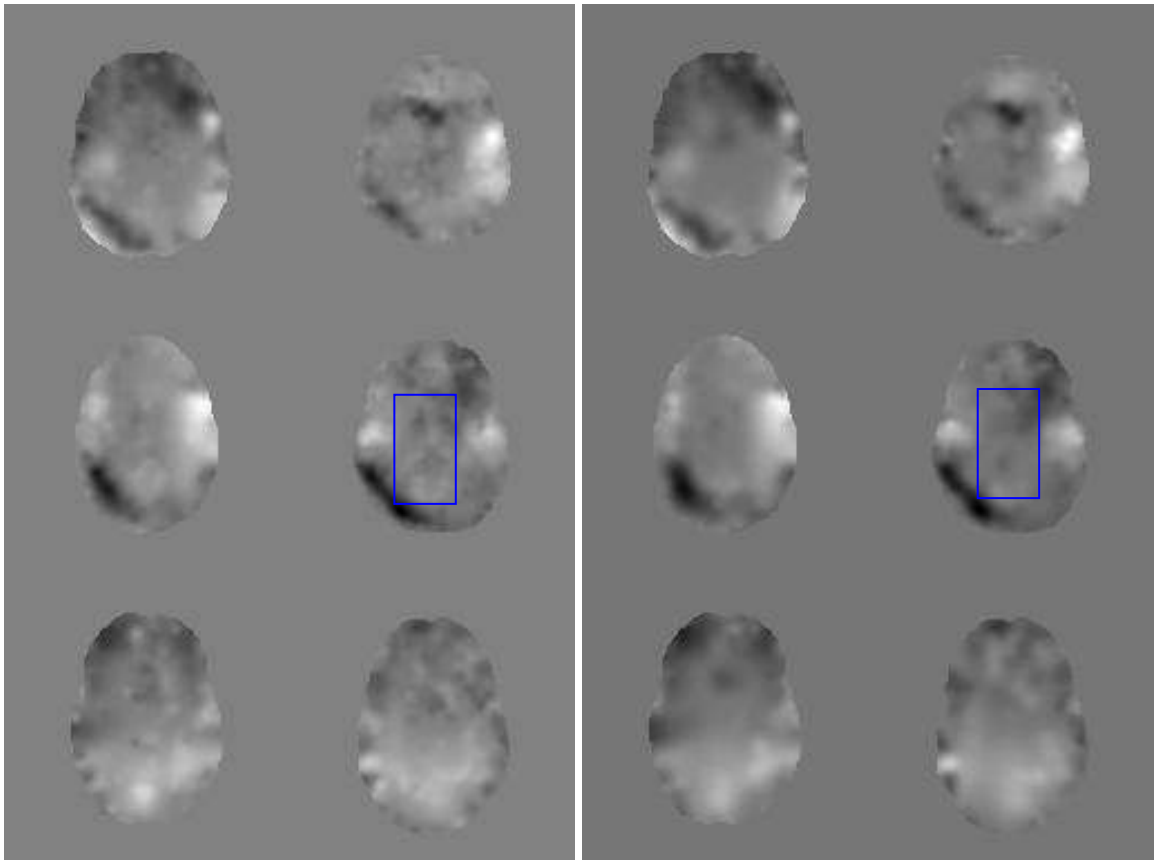

(a) (b)

Figure 22: Estimated distortion fields for 6 subjects using fixed scale (a) and spatially varying scale (b). The regions enclosed by the blue rectangles are shown in Figure 23.

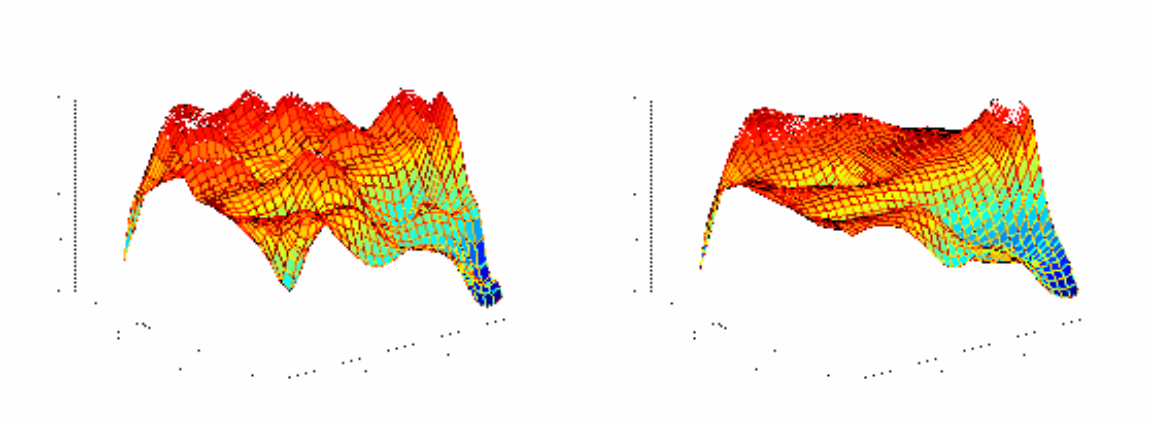

(a) (b)

Figure 23: A close look at the distortion fields obtained with fixed scale (a) and spatially varying scale (b), corresponding to the regions inside the blue rectangles shown in Figure 22.

The smoothness and regularity of the deformation fields obtained with our approaches is illustrated in Figure 22 to Figure 24. Figure 22 (a) and (b) show examples of the deformation fields obtained with the fixed scale and the spatially varying scale approaches, respectively, for all six subjects. In all cases, the deformation fields obtained with both approaches are qualitatively similar, but the varying scale approach leads to smoother fields. Figure 23 shows a 3D view of the magnitude of the deformation field over the rectangular windows shown in Figure 22. Clearly, the use of spatially varying scale leads to a smoother deformation field. To evaluate the smoothness of the deformation fields (12 in total) over the entire image volume, the Laplacian of each deformation field is computed, summed over the volume, and normalized. Figure 24 plots this value for the 6 volumes that have been used to evaluate our method. Using spatially varying scales leads to a reduction on the order of 13%. Timing information for both approaches is provided in Table 2, which shows a substantial amount of reduction for the spatially varying scale method.

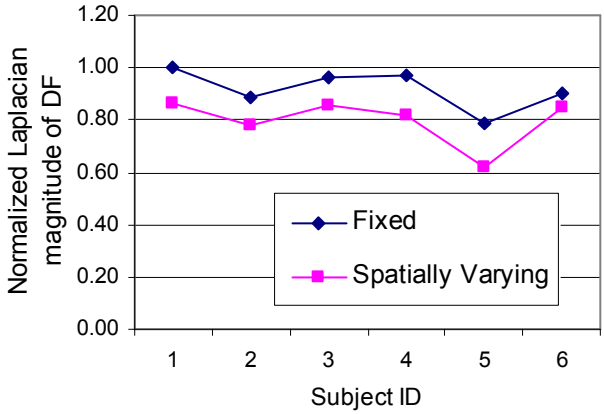

Figure 24: Comparison of the Laplacian magnitudes of the deformation fields.

Table 2: Registration times for 3D real EPI images (min).

Subject ID	1	2	3	4	5	6
Fixed Scale	4.38	4.18	4.18	4.05	4.38	4.6
Spatially Varying Scale	2.81	2.85	2.47	2.4	2.6	2.58
Time Reduction	36%	32%	41%	41%	41%	44%

5. Discussion

Regularizing deformation fields obtained with nonrigid registration algorithms is a difficult issue. Too much regularization leads to inaccuracies. Too little regularization leads to spurious and physically unlikely deformation. Results presented in this paper show that this is the case for EPI images. Excessive regularization leads to transformations that are inaccurate in areas where the magnetic field changes rapidly. Using a regularization scheme that leads to good results in these areas, e.g. basis functions with small support everywhere, unfortunately leads to transformations that are not as smooth as expected in areas where the field changes slowly. This paper proposes a novel approach in which the regularization of the field is adapted spatially by means of a

scale map. We also introduce a method by which this scale map can be generated according to a priori information. Our experimental results show that the proposed approach leads to transformations that are smoother and that can be computed faster than those computed when a fixed scale is used without sacrificing accuracy.

In the ABA method, the scale of the regions of mismatch is detected automatically by employing a multi-scale approach, in which basis functions up to the highest level are applied to the whole image. There is no a priori information incorporated. Thus, in regions of the images in which the field change slowly, the final density of basis functions may be too high. This lengthens the process and can also lead to spurious displacements. By avoiding the use of more complex basis functions in regions that do not require them, the proposed approach addresses both of these problems.

As discussed in the Introduction section, varying the scale spatially based on a priori information was also employed in [46], [59]. These methods rely on a non-stationary diffusion filter applied to the computed displacement field. The diffusion parameter in the diffusion filter is estimated based on knowledge about deformability of segmented tissues. Instead of working on the computed deformation field, we constrain the field at the time of computation using a pre-computed scale map. This reduces the optimization complexity as well as the computational time. Furthermore, such a spatially varying scale mechanism has not been used for EPI images before.

Clearly, the generation of the scale map and of the expected deformation field carries a computational overhead. In our experiments, the scale map computation itself can be done in about 40 seconds; computation of the field map takes about 50 seconds. If these are included in the total computation time, then the spatially varying scale method

loses its computational advantage for the correction of a single volume. However, in practice, the scale map needs to be computed only once for an fMRI study, which may involve more than a hundred volumes. In this case, the method we propose is advantageous. For illustration purposes, we consider registrations on an fMRI dataset with one hundred volumes. The running times for the fixed scale and the spatially varying scale approaches (on a PC with a 3.0G Hz CPU and 1GB of RAM) are 315 min and 208 min, respectively, which represent a 34% reduction in time.

The main parameters that need to be selected include the length of the array Θ, the number of basis functions to be used at each level, and the number of scales to be used in the scale map. The application often suggests the number of scales to use. The length of the array and the number of basis functions to use at every level typically require experimentation when the method is applied to a new type of image. In our experience, when a set of parameter is chosen for one application and one type of image, the same set of parameters can be used across volumes.

Thanks to our simulated images, we are able to show quantitatively that our method holds promise on single EPI image volumes. Further studies will investigate the effect of our correction algorithm on fMRI time series and determine whether or not correction modifies the location and extend of areas of activation.

In this chapter we bring a regularization scheme into our nonrigid registration for distortion correction when a measured field map is not available. When a field map is acquired with EPI acquisitions, it can be utilized to help the registration process. The way to do that will be introduced in the next chapter.

CHAPTER V

FIELD-MAP-CONSTRAINED NONRIGID REGISTRATION FOR CORRECTION OF DISTORTIONS IN ECHO PLANAR IMAGES

1. Introduction

In Chapter II, we have discussed the fact that two broad classes of algorithms have been proposed for distortion correction: field-map methods [15]-[18] and nonrigid registration methods [22]-[28]. Success of field map methods is largely a function of the accuracy of the field map estimation. In the regions of the brain where the field inhomogeneity is severe or the signal to noise ratio is very low, it is difficult to estimate a field map accurately, even if unwrapping/regularization algorithms are used. Physics-based constraints have been added to nonrigid registration methods to help the registration process, as described in Chapters III and IV. The registration process could be further improved if information extracted from the field maps is incorporated. In this chapter we propose to combine the field-map method with nonrigid registration. The field map is used only where it is believed to be reliable. Nonrigid registration takes precedence over the field map where it is not. The proposed approach is demonstrated on a simulated brain EPI image and on a real EPI image of a phantom.

2. Integration of the Field Map with Nonrigid Registration

The same physical model for EPI as that described in Chapter III is used here for distortion correction. By assuming that the phase encoding direction is along the y axis, we rewrite the equation for this model as:

$$i_0(x, y, z) = i_1(x, y + \Delta y, z) \cdot J \cdot h^{-1} \tag{37}$$

where i_0 and i_1 are the intensity values in the corrected and distorted images, respectively, and J and h^{-1} represent the Jacobian factor and the rephasing factor at the position (x, y, z), respectively. Δy is the geometric distortion at the position (x, y, z).

We perform distortion correction in two steps. In the first step, we compute a distortion map Δy directly from the field map and use it as the initial value for the deformation field of our nonrigid registration algorithm. This Δy is also used to compute the Jacobian factor J and the rephasing factor h^{-1} (for GE images), and the distorted image is initially corrected using Eq. (37). We then refine the results obtained in this first step through nonrigid registration. To do so, we use our Adaptive Bases Algorithm (ABA) with physics-based constraints. As described in Chapter III, this algorithm uses a linear combination of radial basis functions (RBFs) with finite support to model the deformation field. These RBFs are placed on a set of grid points in the image and their amplitudes are changed to maximize the normalized mutual information between the reference image and the corrected image.

To accelerate the registration process and reduce the chances of falling into local minima, we utilize information contained in the field map to constrain the optimization. Our strategy is based on one assumption: inaccuracies in the field map occur mainly where the field inhomogeneity is large or changes rapidly and where there is severe signal attenuation, which results in low SNR. The reason is that in these areas the measured field map can suffer severe phase wrapping or unreliable measurement due to low SNR. We build two masks delineating these regions— msk_{field}, based on the

magnitude and gradients of the field map and msk_{image} based on the intensity of the image. Only components of the field map in the *y* and *z* directions are considered because they are responsible for the major geometric and intensity distortions. We define the first mask as:

$$msk_{field} = area\left(abs\left(\Delta y\right) > thrd_{\Delta y}\right) \cup area\left(abs\left(J-1\right) > thrd_{J}\right) \cup area\left(h < thrd_{h}\right) \quad (38)$$

Here, $area\left(\mathrm{A}\right) = \begin{cases} 1 & \mathrm{A\ is\ true} \\ 0 & otherwise \end{cases}$ stands for a brain region with 1 at the locations where the condition inside parenthesis is satisfied and 0 otherwise. $thrd_{\Delta y}$, $thrd_{J}$ and $thrd_{h}$ are thresholds that are set empirically. See Figure 25 (a) for the result. The regions, in which severe distortions are expected, such as frontal brain, are included in the mask.

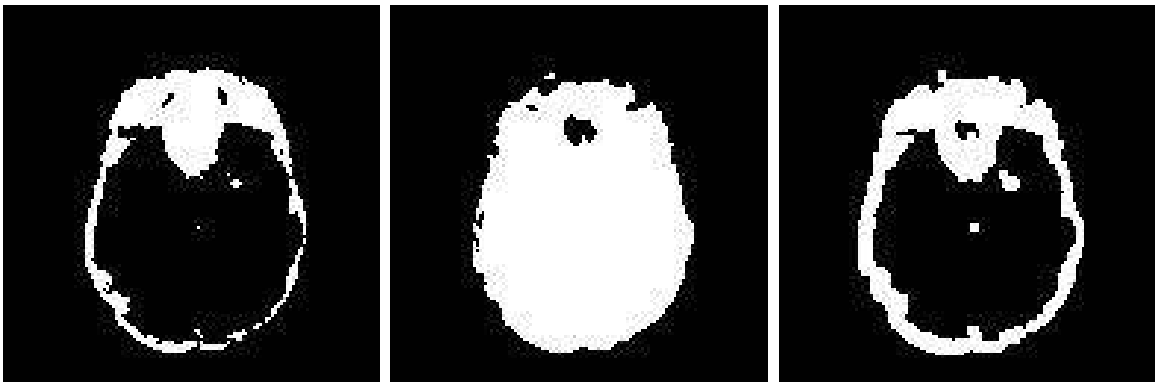

(a) (b) (c)

Figure 25: (a): msk_{field}, the mask generated according to the measured field map; (b): msk_{image}, the mask generated according to the distorted EPI image; (c) the union of msk_{field} and msk_{image}.

We also consider the fact that Jacobian and rephasing corrections may not work well over areas with severe signal attenuation because of low SNR. This is addressed by

identifying regions in the EPI images below an intensity threshold and avoiding placing basis functions over these areas, which gives the second mask, msk_{image}, see Figure 25 (b).

$$msk_{image} = area\left(intensity > thrd_{im} \times max\_intensity\right) \tag{39}$$

with $0 < thrd_{im} < 1$. The union of these two masks, see Figure 25 (c), is used to guide the placement of the grid points, i.e. RBFs are placed only inside this mask. We call this mask msk_{rbf} with:

$$msk_{rbf} = msk_{field} \bigcup msk_{image} \tag{40}$$

Figure 26 shows the locations of the grid points when msk_{rbf} is used and when it is not. As can be seen, only a small portion of basis functions will be employed in the registration process with mask.

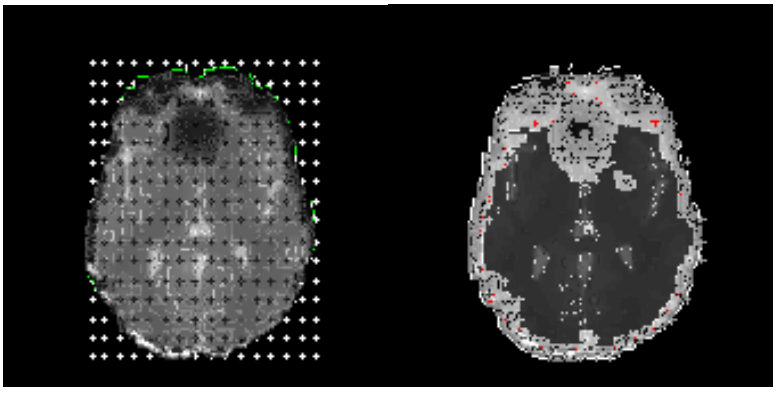

Figure 26: The placement of the grid points without (left image) and with (right image) a mask as the constraint.

3. Experiments and Results

We first test the proposed method using a simulated image obtained with an MR simulator [64]. Figure 27 (a) shows a simulated distortion-free image, and Figure 27 (b) shows its distorted version created with a real field map measured from a human brain. Figure 27 (c) is the intensity difference between Figure 27 (a) and (b). As expected, the distortions happen mainly in the frontal area of the brain. The measured field map is then perturbed to simulate inaccuracy of field map estimation. This corrupted field map is subsequently used as the input to the field-map method and our approach to correct for the distortion in the image shown in Figure 27 (b). The differences between the corrected images and the distortion-free image are shown in Figure 27 (d)-(f). Histograms of intensity differences between the distortion-free image and the distorted image as well as the images corrected with (1) the nonrigid registration-based method only, (2) the field map-based method, and (3) the method we propose are compared in Figure 28. A lower curve indicates better results, and our proposed approach is clearly an improvement. Furthermore, our approach greatly speeds up the calculations because optimization is performed on only a small part of the image. In this case, CPU time was reduced to 0.8min from 4.3min.

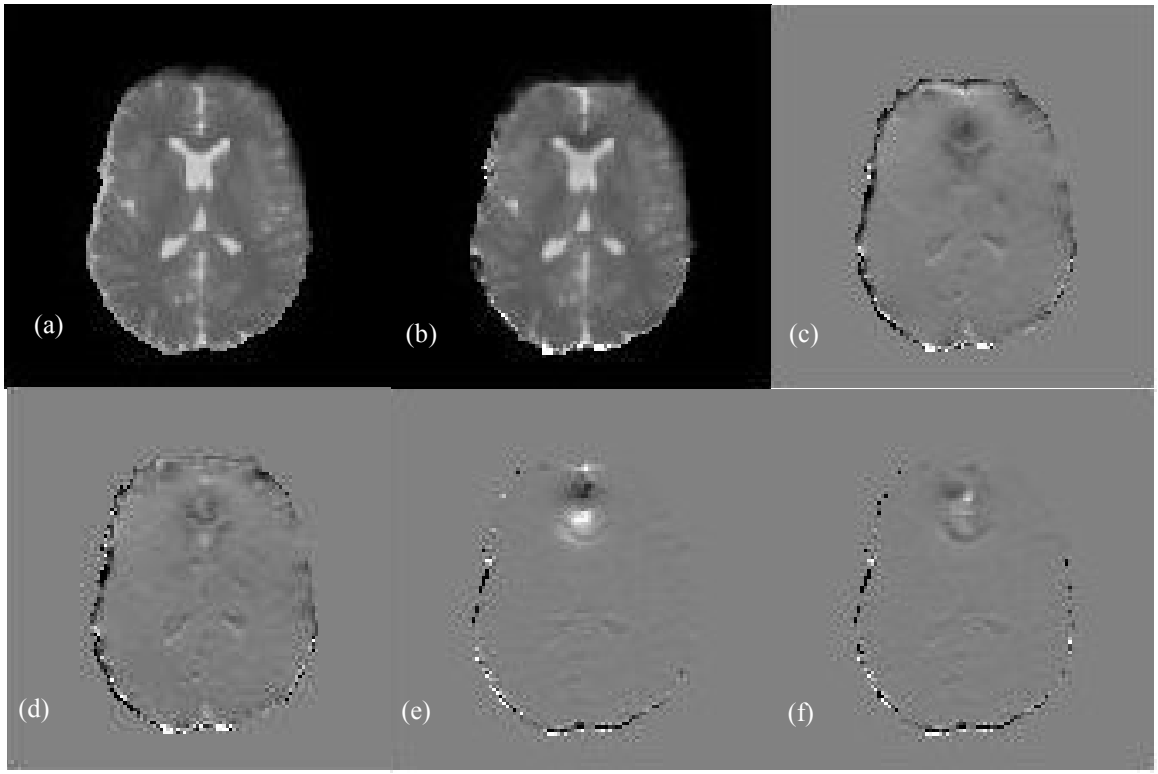

Figure 27: (a): distortion-free EPI image; (b): distorted image; (c): difference between (a) and (b); (d)-(f): differences between distortion-free EPI image and images corrected via nonrigid registration alone (d), the field-map alone (e), and our approach (f).

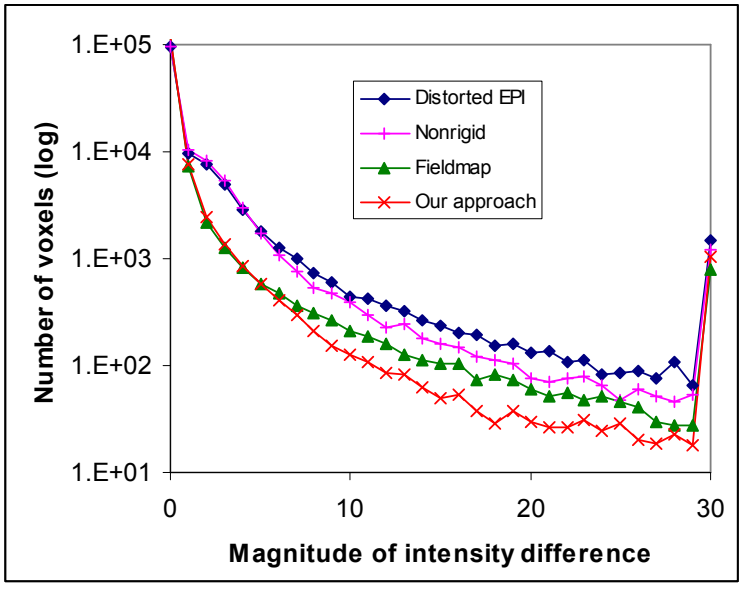

Figure 28: Histograms of difference images.

In Figure 29, an imaging phantom is used to compare results obtained with our approach to those obtained with the SPM FieldMap toolbox [71], which implements a method based on the field map alone. Note that the residual shift near the right edge of the gray part to which the arrows point in Figure 29 (c) (SPM toolbox) has substantially eliminated in Figure 29 (d) (our method).

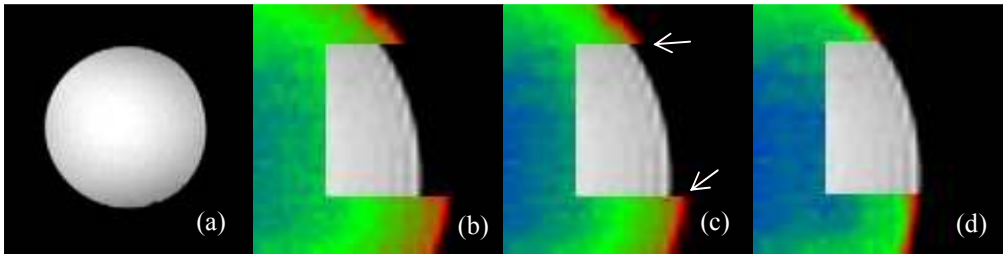

Figure 29: (a): reference image; (b): overlay of the reference image on the distorted image; (c) and (d): overlay of the reference image (gray level) on the corrected images (in color) by two methods: SPM FieldMap toolbox (c) and our approach (d). (b), (c) and (d) are magnified to show the differences).

3.1. Selection of thresholds for mask

The computation of the RBF mask used in our method depends on several thresholds, as can be seen in Eqs. (38) and (39). When the values for these thresholds change, the region covered by the mask varies, and that change may affect the correction results. The purpose of this experiment is to determine how the change of the RBF mask affects the results. We pick one threshold ($thrd_{\Delta y}$) and change its value from 0.5 to 1.5 (voxel units) with step size 0.25. We then generate five RBF masks corresponding to different $thrd_{\Delta y}$, as shown Figure 30. It can be seen that the region of the RBF mask

reduces gradually when $thrd_{\Delta y}$ is getting bigger. Each of these RBF masks is used in our method to correct the image shown in Figure 27 (b). By comparing the corrected images, we find that using different masks has a negligible effect on the results. This suggests that our approach is not sensitive to the RBF mask changing in certain range.

Figure 30: Different RBF masks (msk_{rbf}), from left to right corresponding to $thrd_{\Delta y}$ changing from 0.5 to 1.5 with step size 0.25.

4. Conclusion

We propose a strategy for the correction of distortions in EPI images, which combines field map and nonrigid registration methods. Our results indicate that using the field map both to initialize and to constrain our non-rigid registration algorithm may improve the obtained results.

We have introduced a correction method limited to GE EPI images (Chapter III), and two correction methods for both SE and GE EPI images: a registration method (Chapter IV) and a combination method (this chapter). Comparing our methods with another commonly used post-processing method: field-map methods on real brain images is an interesting problem and will be performed in the next chapter.

CHAPTER VI

COMPARISON OF THREE DISTORTION CORRECTION METHODS FOR EPI IMAGES

1. Introduction

In Chapter II, many distortion correction methods for EPI images have been described. They are generally divided into two groups: prospective methods, which rely on techniques designed to reduce these artifacts during or before the acquisition of the images and retrospective methods, which rely on the processing of the images after acquisition. Among the retrospective methods that have been proposed, field-map methods and registration methods have been widely used in a number of applications.

Field-map methods need additional scans from which to calculate a field map. This type of method usually requires pre-processing of the acquired field map, such as regularization and phase unwrapping. The accuracy of the field map depends on a number of factors such as respiration, blood flow, and other imaging artifacts, and the performance of the aforementioned pre-preprocessing method. Subject motion during EPI images acquisition also influences the effectiveness of the field-map methods [1]. Registration methods compute a deformation field by registering the EPI image to a reference image (usually a conventional MR image) in which the distortion is negligible. The obtained deformation field, which provides an estimate to the existing geometric distortion, is applied to the EPI image to produce a corrected one. The accuracy of such methods depends on the optimization technique, the similarity measure, and the deformation model that are used as well as on the quality of the image to be registered.

Recently, the combination of the two types of methods has been proposed, as described in Chapter V. In this approach, a displacement map computed with a field map is used to initialize a deformation field, which is then refined with a registration based method. This displacement map is also used to constrain the optimization during registration, which can both accelerate the process and reduce problems of local minima. Each of these methods has its advantages and disadvantages, but very few comparative studies in which these techniques have been evaluated side by side can be found in the published literature.

In this chapter, we compare three approaches. The first one relies solely on a field map and is called FLD. The second, which is called REG, is a registration method. The last one, called COMB, combines the two. This study is performed on both 3T and 7T EPI images. This chapter is organized as follows: Section 2 describes the data we have used. Section 3 presents some pre-processing steps and introduces briefly the three distortion correction methods. Results on experiments performed on the 3T and 7T real EPI images are presented in Section 4. Conclusions are drawn in Section 5.

2. Data Acquisition

For each subject, three types of data have been acquired. The first are T2*-weighted Gradient Echo (GE) EPI images, which are commonly used in functional MR studies. These images are then corrected using three different methods described in this chapter. The second is a GE non-EPI field-map image. This image measures the deviations of the magnetic field from homogeneity. The third is a conventional MR image. It is assumed that this image has negligible distortions. All data acquisitions are performed on a Philips 3T or 7T MR scanner.

Ten subjects were scanned using a 3T scanner. The GE EPI images were acquired using a FEEPI sequence, with matrix size 128 x 128 (interpolated from 80 x80), slice number 28, TE 35 ms, TR 1988.3 ms, field of view (FOV) 240 x 240 mm, and slice thickness 4.5 mm with 0.4 mm gap. Phase encoding is in the anterior-posterior direction. SENSE is used for the acquisition (SENSE factor 1.7). A T1-weighted high resolution conventional image for each subject was acquired using an Inverse Recovery Turbo Spin Echo (IR TSE) pulse sequence, with the same slice number and FOV as those used for the EPI images; the matrix size is 256 x 256, TE 10 ms, and TR 2000ms. It takes 1 min 56 s to acquire such an image volume. Each field map is obtained from the phase difference between two Fast Field Echo (FFE, gradient echo) scans collected at different echo times. The field map has the same number of slices, FOV, and matrix size as the EPI image. It takes 55 s to acquire this image.

We also acquired a set of multi-shot EPI images for one subject on a 7T scanner. Normally EPI is a single-shot imaging technique, i.e. a single excitation pulse results in a complete image. However, a multi-shot EPI, using multiple excitations per image, may be used to increase spatial resolution and/or reduce geometric distortion. Here, five EPI scans were acquired with different numbers of shots: 2, 4, 8, 16 and 32. All scans have a matrix size of 128 x 128, slice number 15, TE 25 ms, FOV 192 x 192 mm, and slice thickness 4.0 mm with 0 mm gap. TR times are inversely proportional to the numbers of shots and change from 990.10 ms for the 2-shot scan to 61.88 ms for the 32-shot scan. Acquisition times are 2.8s for 2 shots, 7.5s for 4 shots, 9.4s for 8 shots, 14s for 16 shots and 43.2s for 32 shots. A high resolution conventional MR image is acquired using a FFE pulse sequence, with the same number of slices and FOV as the EPI images, matrix size

256 x 256, TE 5 ms, TR 500 ms. A field map is also acquired using the method used for 3T data. It has the same slice number, matrix size and FOV as the conventional image and takes 110 s to be acquired.

3. Methods

3.1. Data processing

Since the scalp is clearly imaged in the conventional MR images while it is not in the EPI images (see Figure 31 for example), it may affect the registration results, especially around the boundary of the brain. Therefore, both EPI and conventional MR images are preprocessed by applying a brain mask to remove non-cerebral parts. The brain mask for each subject is generated by using the Brain Extraction Tool (BET) software [70] on a magnitude image obtained from the field-map scan. After masking, the conventional MR images are downsampled from 256 x 256 x 28 to 128 x 128 x 28 to facilitate the following registration process.

The scan for field map acquisition provides two images simultaneously: one magnitude image and one frequency image (with unit in Hz). These two images are derived from the two complex images $\mathbf{C}_1$ and $\mathbf{C}_2$, acquired at different echo times: $T_{E,1}$ and $T_{E,2}$, respectively. The magnitude of $\mathbf{C}_1$ and $\mathbf{C}_2$ are the same and either of the two can be used as the magnitude image. The phase difference accrued between the two images is $\Delta\mathbf{\Phi} = \angle\left\{\mathbf{C}_1^*\mathbf{C}_2\right\}$ and is called the phase image. The frequency image is calculated as:

$$\mathbf{f} = \frac{\Delta\mathbf{\Phi}}{2\pi\,\Delta T} \tag{41}$$

where $\Delta T = T_{E,1} - T_{E,2}$ is the change in echo time. Because the phase difference is wrapped into the range [-π, π], it needs to be unwrapped by adding multiples of 2π when necessary. This was done by using a tool called PRELUDE [70]. PRELUDE takes as input both the magnitude image and the phase image (converted from the frequency image according to Eq. (41)). The software produces an unwrapped phase image. Also, regions in this image where the intensities are low in the magnitude image are assigned a phase value of zero. This is so because at these locations, the phase information can not be estimated accurately. This phase image is then converted back to the frequency image. The brain mask used for EPI images is also used here to mask the obtained frequency image. To increase the signal to noise ratio, this frequency image is smoothed using a 2D Gaussian kernel. Finally, this preprocessed frequency map is used to compute a displacement map **D** as:

$$\mathbf{D} = \frac{\mathbf{f} \cdot \mathrm{FOV}}{\mathrm{BW} \cdot v_y} \tag{42}$$

where BW is the bandwidth in the phase encoding (here y) direction and v_y is the voxel size in the y direction.

3.2. Description of three distortion correction methods

(a) Field map method for distortion correction (FLD)

With the displacement map **D** computed according to Eq. (42), EPI images are undistorted using the pixel-shift method [16]. Intensity correction factors, i.e. Jacobian and rephasing factors as described in chapter III, are included to correct for intensity distortion and signal loss, respectively. Tri-linear interpolation is used for resampling.

(b) Registration with spatially varying scales (REG)

This method has been introduced in detail in Chapter IV and is described here only briefly. The conventional MR image for each subject is used as the reference image to which the EPI image is non-rigidly registered. Before registration, a simulated distortion field is first generated for each subject using an MR simulator [64]. The input to the simulator is a water/air mask for this brain. Given the simulated distortion field, a scale map with two values (4 and 6) is computed and used to vary spatially the final density of the basis functions. During registration, six levels of radial basis functions (RBF) are used to model a deformation field, which provides an estimate of the existing geometric distortion in the EPI image. The first four levels of RBF are used in regions where the scale map is equal to 4 and all six levels of RBF are used in regions where the scale map is equal to 6. Only one image resolution is used. The optimization is performed along only the *y* direction, which is the phase-encoding direction in EPI images.

(c) Registration with field map as initialization (COMB)

This method has been introduced in detail in Chapter V. Here again we provide only a brief description. The source and target images are the same as the ones used in method REG, but the deformation field is initialized with the distortion map computed from the field (frequency) map. This deformation field is then refined through the nonrigid registration process. As is the case in method REG, six levels of RBF and only one image resolution are used during registration. A binary mask, computed from the distortion map and the EPI image, as described in Chapter V, is used to guide the placement of basis functions during registration, i.e. RBFs are placed only in regions with a mask value equal to 1. In the regions in which the mask value is zero, the displacements

provided by the field map are used. This method reduces the number of regions to be optimized and thus requires less time than method REG.

4. Experiments and Results

4.1. 3T EPI images with ten datasets

In this experiment, we compare the three distortion correction methods using ten 3T datasets. Figure 31 shows an example of the acquired conventional MR (left column) and EPI (right column) images in both axial and sagittal views. They are then processed as described in Section 3.1 and used for distortion correction.

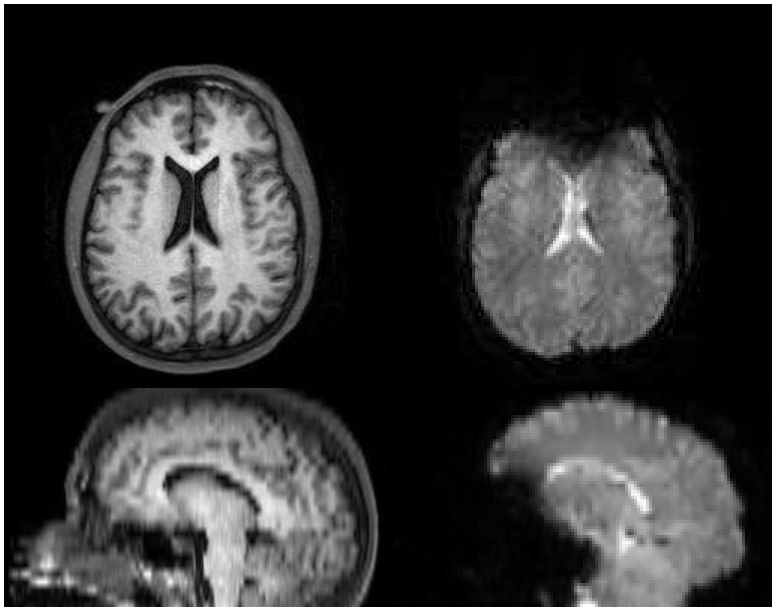

Figure 31: Conventional MR (Left column) and EPI (right column) images of one subject.

For each subject, we apply the three distortion correction methods to the original EPI image. Results from one of the subjects are shown in Figure 32, in both sagittal and axial views. Figure 32 (a) shows the conventional MR images. Figure 32 (b)-(e) shows

the EPI images before correction and corrected with methods FLD, REG and COMB, respectively. The outer contour of the brain is outlined in (a) and overlaid onto the other images to show the existing geometric distortions. All three correction methods provide similar geometric correction results. One notes that the geometric distortion in the original EPI image is mild except for the frontal part of the brain. This is confirmed by checking the displacement map computed from the measured field map for this subject using Eq. (42). Figure 33 shows the displacement map (a) and a mask in which the magnitude of the displacement is larger than one voxel (b). Each slice of mask (b) is overlaid onto the corresponding EPI slice. This figure shows that severe geometric distortions are concentrated in the frontal areas and the edge of the brain. The mean of the magnitude of the displacements for each slice is computed and plotted in Figure 34. It shows that the mean values become quite small (less than 0.5 voxel) after the 12^{th} slice.

Signal loss is, however, quite perceptible in the EPI image, as shown in Figure 32 (b). Figure 32 (c)-(e) shows that all three methods are able to reduce the signal loss effect thanks to the use of the intensity correction factors discussed in the Methods section. But, the results from method FLD appear to induce more unrealistically high intensity values into the corrected image than methods REG and COMB, as pointed by the arrows in Figure 32 (b).

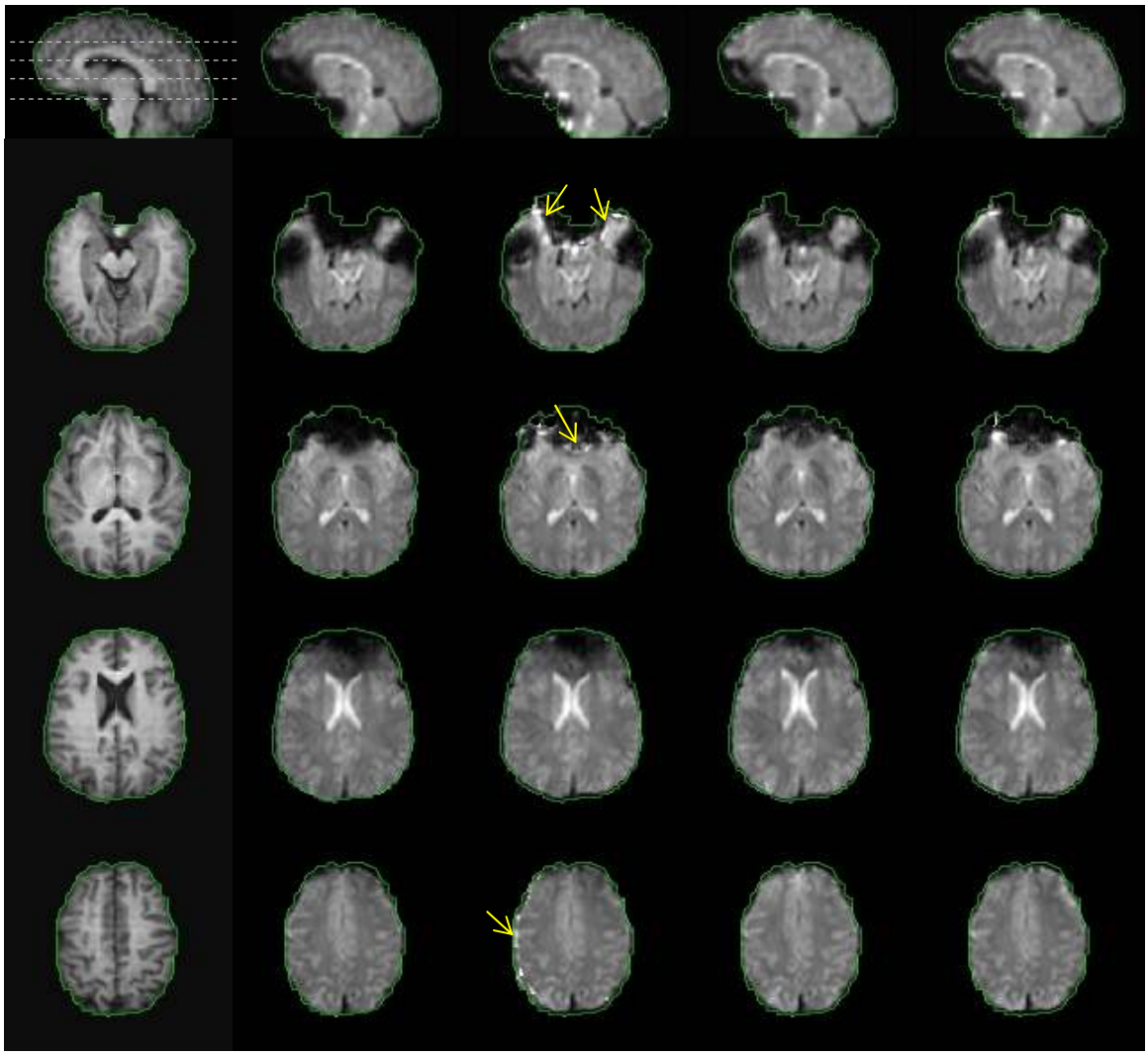

(a) (b) (c) (d) (e)

Figure 32: Distortion correction results for one subject using three methods. (a): Conventional MR image; (b): EPI image before correction; (c), (d) and (e): EPI image after correction with method FLD, REG and COMB. Both sagittal (the 1st row) and axial (the 2nd to the 5th row) views are shown. The locations of the axial views are indicated with the dotted lines in the top left image.

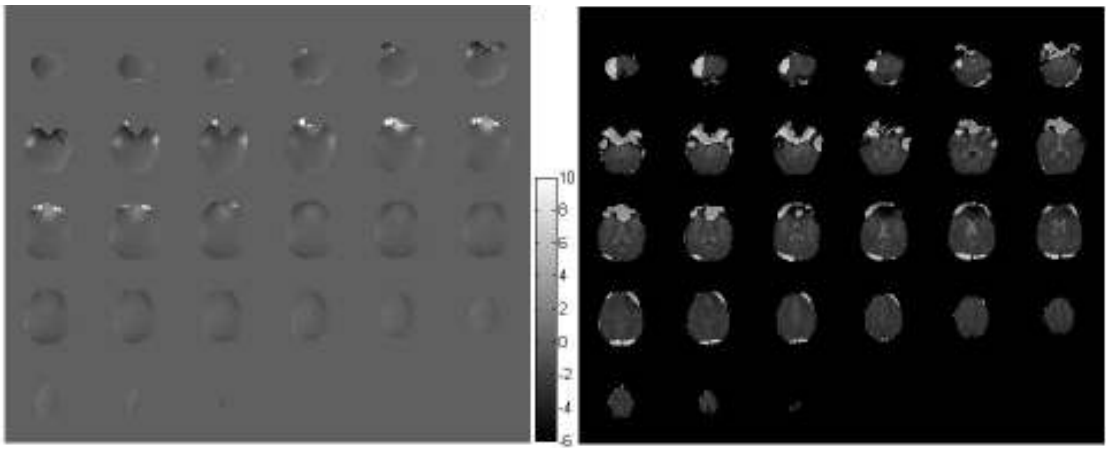

(a) (b)

Figure 33: Displacement map computed from a measured field map. (a): 28 slices of the displacement map; (b): a mask (the brightest regions), in which the magnitude of displacement is larger than one voxel, overlaid on the original EPI image.

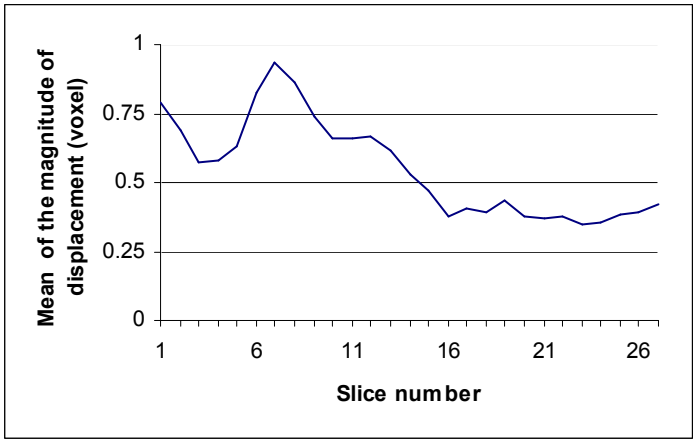

Figure 34: Mean in voxel units of the magnitude of displacement across slices.

Comparing the three correction methods one subject at a time is difficult as one method may appear superior to the other in one case and inferior in another case. To address this issue, we have compared methods on the entire population after spatial normalization.

Spatial normalization is an important step during multi-subject studies for EPI images, such as group analysis in fMRI [81] or DTI [82]. It is used to align the same brain regions across subjects together, which may enhance the statistical power of a random effects group study. Here, we randomly choose the conventional MR image of one subject as a template and align the conventional MR images of other subjects to the template. This alignment includes two steps: First, a rigid registration technique [83], [84] with six degrees of freedom (three rotation angles and three translations) is employed to match each image to the template roughly; Second, the rigidly transformed image is locally deformed to the template using a nonrigid registration method [43]. For each subject, the combination of the two deformation fields obtained in the two steps is then applied to the EPI images before or after correction. With this procedure, we generate four groups of spatially normalized images based on four sets of EPI images: before correction, and corrected with methods FLD, REG, and COMB.

We compute the average of the normalized images for each case and show the results in Figure 35. As can be seen, for all cases, the overall shape of the averaged EPI images resembles that of the conventional image except possibly in the anterior region, where intensity attenuation is too severe to determine the boundary. This may be explained by the relatively small displacements existing in the original EPI images as observed in the previous experiment. But, noticeable intensity differences between the results can be found in the frontal and temporal cortex, as pointed by the arrows. Intensity profiles along the lines drawn in Figure 35 (b)-(e) are plotted in Figure 36 to show the intensity differences between results from the three methods. The region encircled by an ellipse in this figure highlights the amount of intensity recovered near the edge by the

three methods. These results show that the REG and COMB methods are better than the FLD method at recovering the signal.

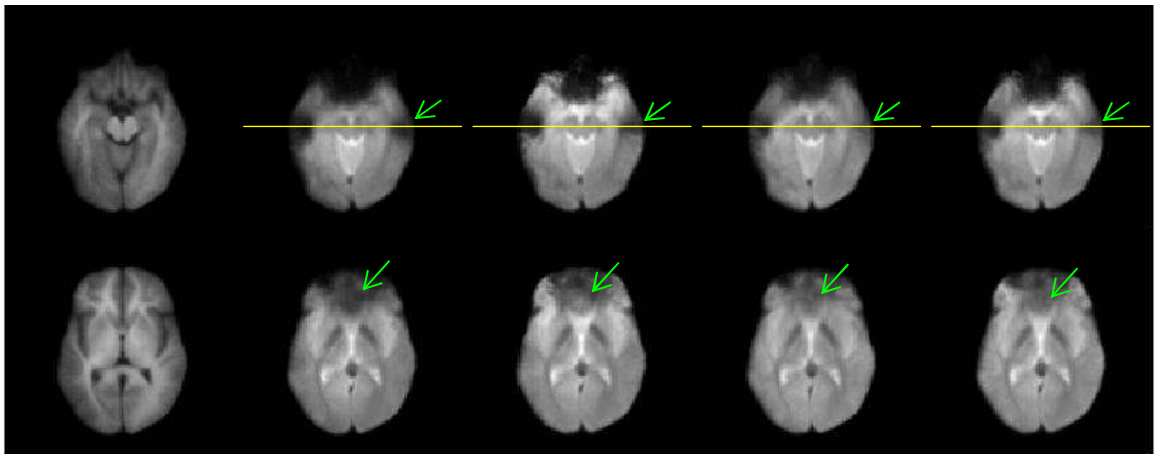

(a) (b) (c) (d) (e)

Figure 35: Average of the spatially normalized conventional MR image (a), EPI images before correction (b), corrected with methods FLD (c), REG (d) and COMB (e). Two rows show images at slice number 10 and 13.

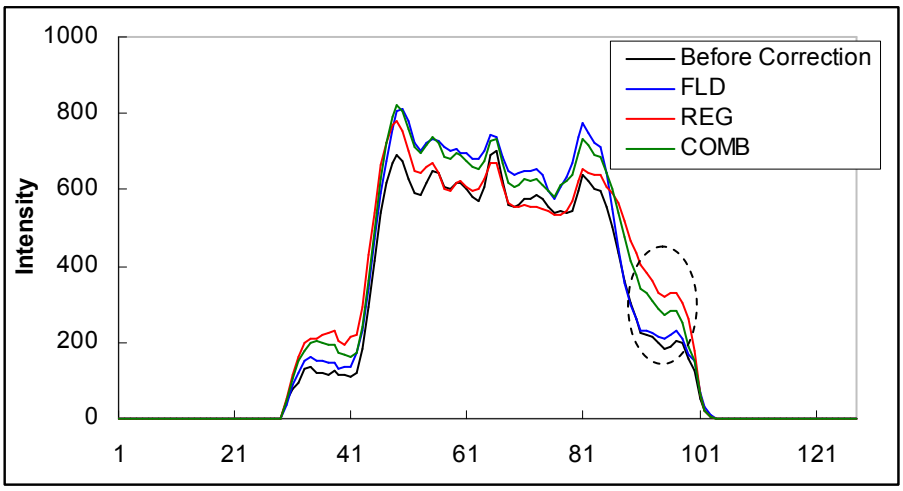

Figure 36: Intensity profiles along the lines from left to right in Figure 35 (b)-(e) top row.

To compare more quantitatively the influence of the correction method on the normalization results, we first check the improvement in similarity between each of the normalized EPI images and the template due to the three distortion correction methods. To do so, we compute two similarity measures: normalized mutual information (NMI) [69] and the correlation ratio (CR) [85]. The results for each correction method are plotted in Figure 37. Using the boxplot function provided by Matlab [The MathWorks, Natick, MA], the statistics on these results is computed and shown in Figure 38. In this figure, the columns show the statistics on the similarity values obtained before correction and after correction with the three methods. The box is bounded on the bottom by the first quartile and on the top by the third quartile. The red line in the middle of the box indicates the median. By comparing the medians of all groups of data for both similarity measures, it can be seen that images from all subjects show an improved match with the template after correction. Among the three methods, method REG provides the highest median values. We also perform a paired *t*-test with Bonferroni correction between each pair of correction methods to test whether or not the results are statistically different. While there is no significant difference at $p = 0.05$ (0.017 with Bonferroni correction for three tests) between methods FLD and COMB or between methods COMB and REG, method REG is significantly different from method FLD ($p < 0.01$ for NMI and $p < 0.006$ for CR).

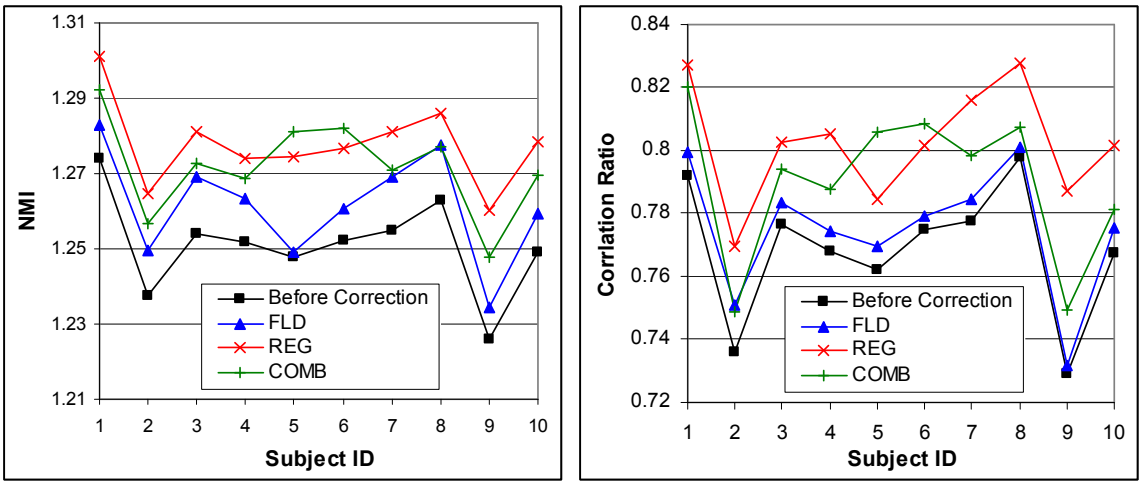

(a) (b)

Figure 37: Similarity measures between the normalized EPI images and the template. (a): Normalized Mutual Information (NMI); (b): Correlation Ratio (CR).

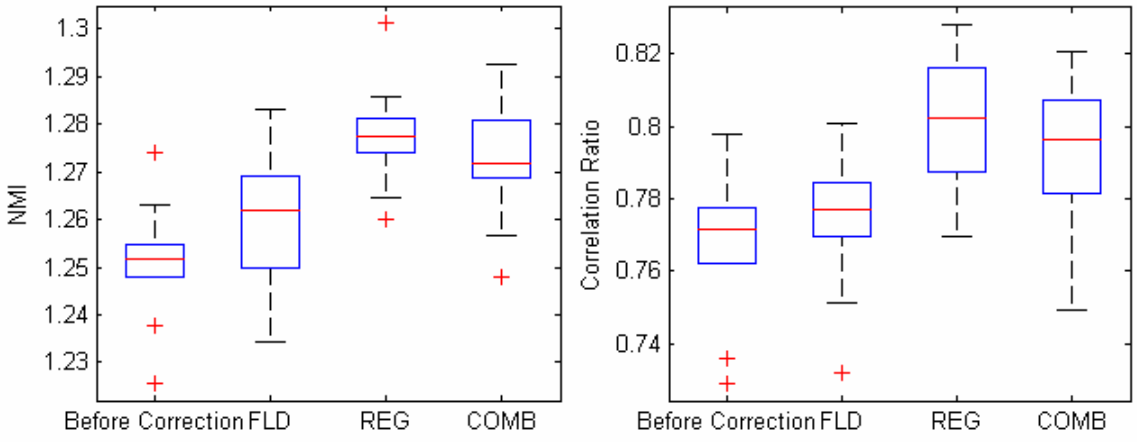

(a) (b)

Figure 38: Box plot of the values for two similarity measures. (a): NMI; (b): CR.

We also use another method to compare the correction techniques. For each method, we take the 10 normalized volumes and applied a principal component analysis to this set of images. We then compute the principal component images, which are the projections of the original images onto the principal components. If all the images in the set were absolutely identical, the first principal component image would be identical to

these images and the other ones would be zero. If there are differences between these images, the first principal component image would capture the common feature among all the images and the higher order PC images would capture differences between these images. In addition, the eigenvalue associated with each principal component image is the variance in this component. The larger it is, the more information the component image contains. Figure 39 shows the first five principal component images for the three methods. The image from method FLD appears to contain more variations than that from method REG or COMB. Figure 40 plots the cumulative sum of the eigenvalues as a function of the number of principal components. This plot shows that the difference among the normalized images is the largest with the FLD method and the smallest with the REG method, again indicating that the FLD method is not able to correct images as well as the other methods.

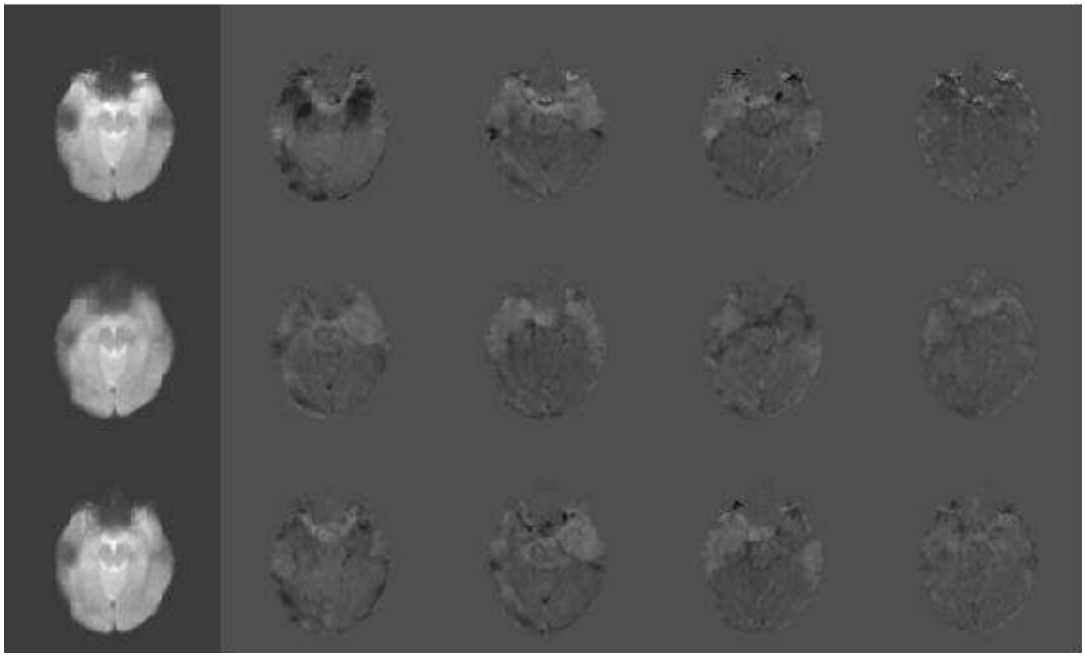

Figure 39: First five principal component images for methods FLD (top row), REG (middle row), and COMB (bottom row).

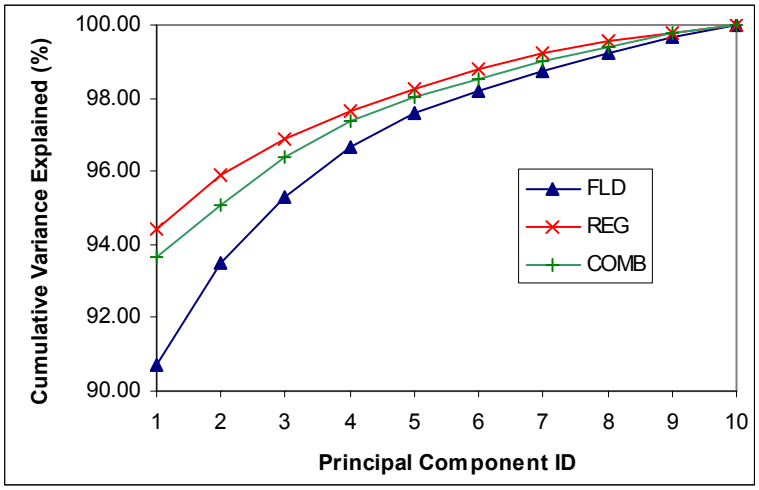

Figure 40: Cumulative variance explained by principal components for each distortion correction method.

4.2. 7T EPI images with multiple shots

In this experiment, we examine the three distortion correction methods using multiple-shot EPI images collected on a 7T MR scanner. Because they provide a high signal-to-noise ratio, higher spatial and temporal resolution, and improved contrast, ultra high field (7T and above) scanners are increasingly being used for many applications. However, susceptibility effects also increase in proportion with the field strength. Thus, susceptibility induced distortions in 7T EPI images are more severe than those in 3T images. To reduce such distortions, multi-shot imaging techniques are used for EPI scans. According to the physics of MR imaging, geometric distortion in images is reduced by half when the number of shots during imaging is doubled. Here, we compare the correction results obtained on these 7T datasets using the three methods. We also evaluate the ability of each of these methods to produce an image equivalent to an image acquired with more shots than the image being corrected. The conventional MR image is

shown in Figure 41 (a). It can be seen that there exists spurious intensity variation across the image, and more specifically, the intensity values in the central of the image are much higher than expected. This phenomenon is called center whitening or dielectric resonance artifacts [86], [87], which is caused by an inhomogeneous radiofrequency distribution in larger tissue volumes and is more pronounced at high field imaging. To mitigate the effect of this artifact on our registration method, which uses intensities as its similarity measure, we preprocess the image using the method described in [88], which uses a parametric estimation of a bias field to correct the image. The image after bias correction is show in Figure 41 (b).

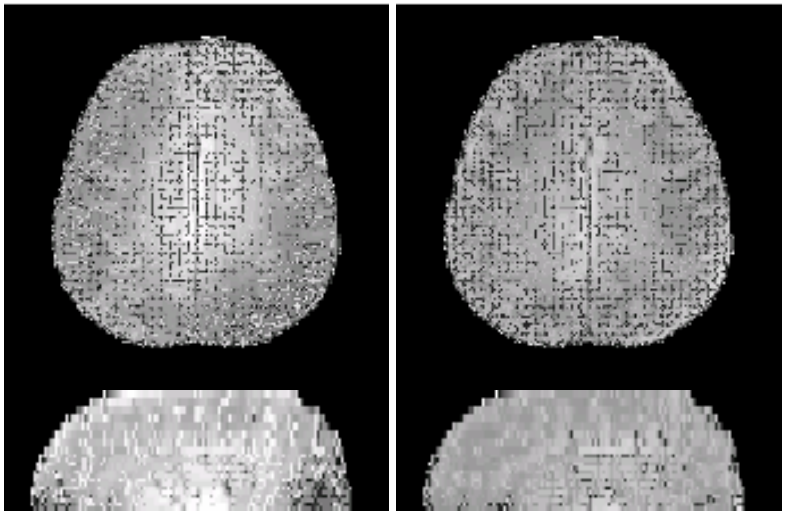

(a) (b)

Figure 41: 7T conventional MR images. (a): Before bias correction; (b): After bias correction.

One axial slice in each EPI image acquired with 2, 4, 8, 16 or 32 shot is shown in Figure 42 (a)-(e). The corresponding slice in the conventional MR image is shown in Figure 42 (f). To illustrate the amount of geometric distortions visible in the EPI images,

lines along some visible structures are drawn in the conventional MR image and overlaid onto the EPI images. The displacements of the structures in the EPI image with 2-shot (a) are clearly visible. With more shots, the amount of displacement is reduced. In the images with 16- and 32- shots, the lines already match the corresponding structures very well.

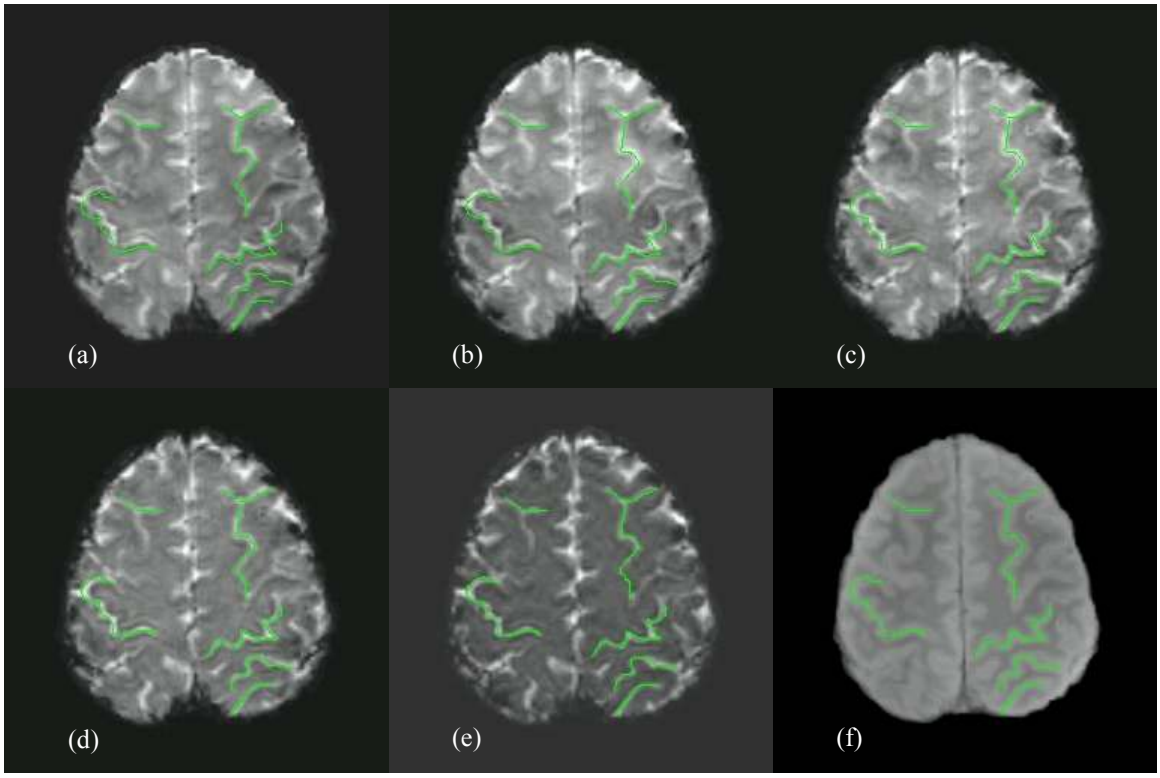

Figure 42: EPI images acquired with different shot numbers: 2 (a), 4 (b), 8 (c), 16 (d), and 32 (e), and the corresponding conventional MR image (f). Lines along visible structures in (f) are manually drawn and overlaid onto (a)-(e).

Figure 43 shows the images in Figure 42 after correction using methods FLD (left column), REG (middle column) and COMB (right column). Rows from top to bottom in this figure correspond to shot numbers 2 to 32, respectively. The lines drawn in Figure 42 (f) are overlaid onto the images to evaluate the correction results. By checking the

corrected images in the top two rows, which are generated from the images with 2- and 4-shots, it can be seen that method FLD reduces the distortions but also that noticeable displacements remain (left column). In the images corrected with methods REG and COMB (middle and right columns), the lines match the corresponding structures more closely. For the images with 16- and 32- shots, in which geometric distortions are not noticeable, corrections barely change the images. By visually comparing the degree of match between the manually drawn lines and the structures in the corrected 2-shot images (shown in the first row in Figure 43) with that in the original EPI images (shown in Figure 42), we observe that the remaining geometric distortions in the 2-shot images corrected using methods REG and COMB are comparable to the original 16- or 32-shot images. This implies that with the help of such post-processing methods, a lower number of shots can be used while keeping the geometric distortion in the acquired image comparable to the distortion observed in images with more shots. This, in turn, reduces acquisition time. In our experiments, the imaging time differences between 2-shot and 16- and 32- shots is 11.2s and 41.4s, respectively.

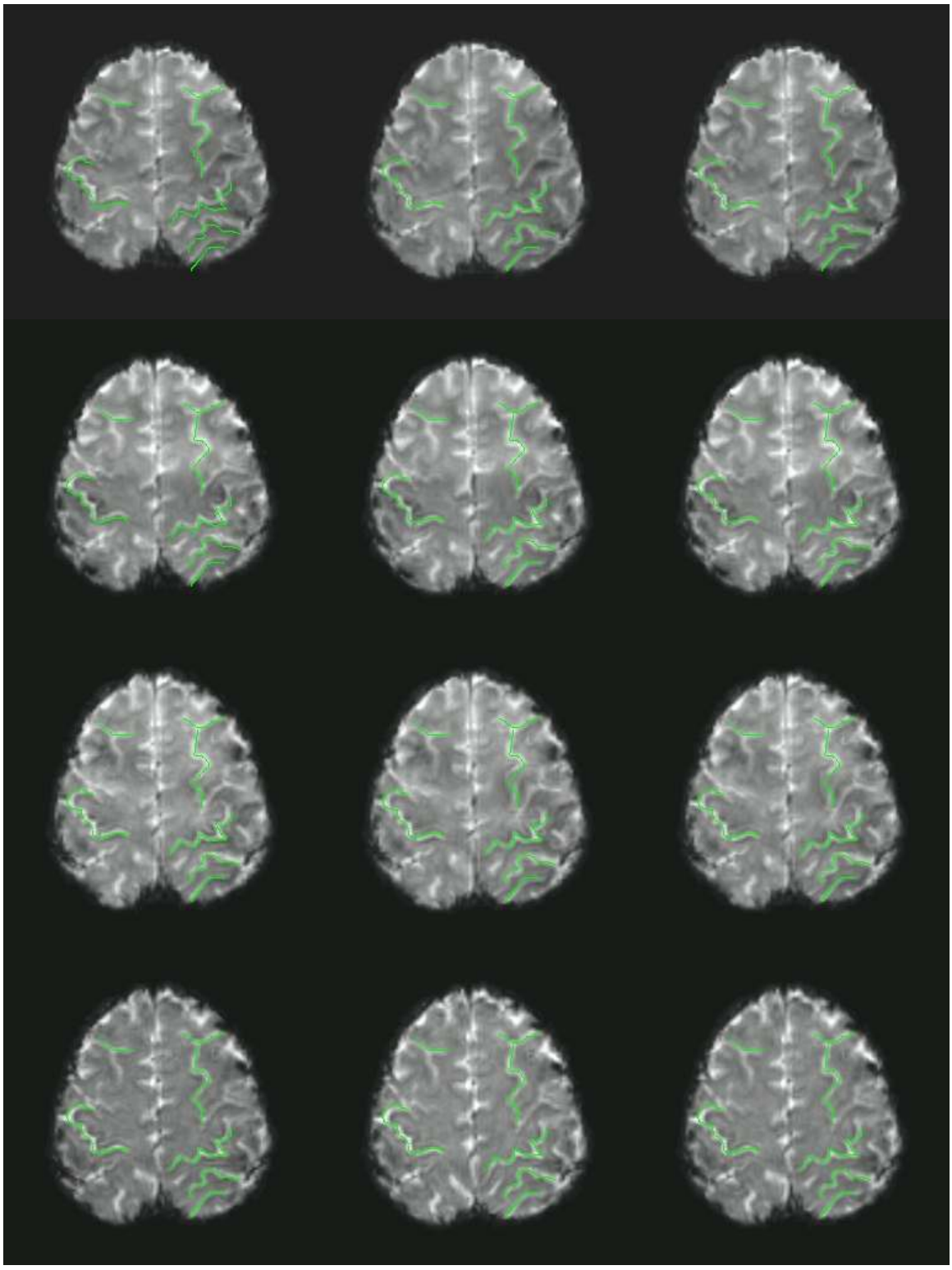

Figure 43: EPI images after correction with method FLD (left column), REG (middle column), and COMB (right column). Rows from top to bottom correspond to shot numbers 2, 4, 8, 16 and 32, respectively.

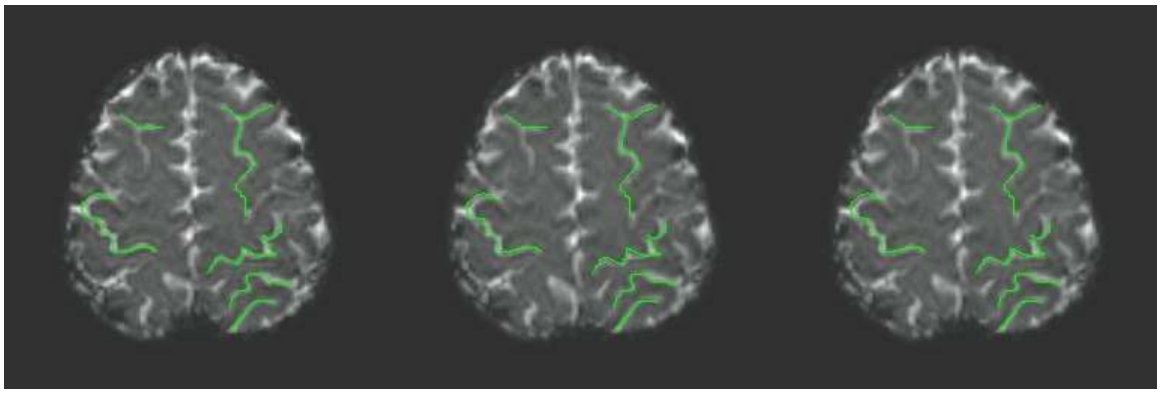

Figure 40, Continued

To compare the correction results quantitatively, we also draw lines in the EPI images along the same structures as in the conventional image. After correction, we deform the lines in each image using the deformation fields provided by the three methods separately. We then compute a distance measure between the lines in the conventional image and those in each EPI image before and after deformation. The distance measure is defined as the square root of the sum of squared minimum distances from each point on the lines in the EPI image to the lines in the conventional image. A lower value of this measure means a better match between the structures in the EPI and the conventional images. Table 3 shows the results. For all EPI images, the three correction methods are able to reduce the distance measures. For the 2-shot image, methods REG and COMB provide noticeable lower distance measures than that from method FLD. For the images with higher shots, all three methods perform similar.

Table 3: The distance measures between the lines drawn in the conventional MR image and those drawn in the EPI images and their deformed versions (voxel).

Shots	2	4	8	16	32
Before Correction	42.13	25.08	17.15	14.09	13.83
FLD	23.52	14.83	10.97	9.38	8.36
REG	16.20	13.84	11.94	11.35	11.20
COMB	15.60	13.38	11.78	11.22	9.86

5. Discussion

In this study we have compared three retrospective distortion correction methods for EPI images. Both 3T and 7T images are used in the experiments. The results we have obtained indicate that the choice of a method for distortion correction largely depends on the type of distortions to be corrected as well as on the availability of data.

For EPI images in which the distortion is relatively small, such as the 3T EPI images used in our experiments, all three methods perform in a similar way if geometric corrections alone are considered. In this case and if the data can be acquired, field map methods should be the preferred to registration methods because of their simplicity.

Field map based methods, however, are prone to causing their own intensity artifacts when used for intensity correction. These artifacts are due mainly to the difficulty of calculating the rephasing factor, which requires the computation of the derivative of the measured field map across axial slices (here in the z direction). In EPI acquisitions, in order to limit the scan time, a small number of axial slices are usually acquired. This may lead to a rapidly changing field in the z direction. Therefore, the estimated derivative of the field in the z direction may be inaccurate and cause severe intensity artifacts. Applying a simple low-pass filter to the field map in the z direction can not solve this problem. These intensity artifacts are less discernible in the registration

methods due to the smoothness of the RBF modeled deformation field. Therefore, when intensity correction is needed, a registration method or a method combining registration and field-mapping should be preferred. The combination approach has the additional advantage of being faster than the method based purely on registration while leading to comparable results. Note that the accuracy of registration methods is limited by the voxel size and the optimization algorithm they use. When the geometric distortion is small (less than one voxel), the estimation error introduced in the registration process may be comparable to the distortion itself. Although it is difficult to observe in our 3T data, this type of error may be reduced in the combination approach because of the constraints introduced by the field map.

For EPI images in which the distortion is much larger, such as in the 7T EPI images we have used, while the results show no apparent difference between the registration method and the combination method, both of them outperform the field-map method. An interesting finding is that the corrected 2- or 4-shot EPI images appear to have an amount of geometric distortions that is comparable to the amount of distortions observed in the uncorrected 16- or 32 shot EPI images, which take much longer to acquire.

The effectiveness of the field-map method is largely determined by the accuracy of the field inhomogeneity measurement. Our experiments for 7T images show that a field map may not be accurately measured when the existing inhomogeneity is severe. In this work, we use the standard field map acquisition method to get a field estimate. More sophisticated imaging techniques, such as [89], could be used to improve the quality of the obtained field map. It is also worth mentioning that other imaging artifacts existing in

conventional MR acquisition may also affect the estimate of the field map. Another potential issue which may affect field map based methods is motion. Since susceptibility artifacts are related to subject movement [1], a field map acquired at the beginning of the study may not reflect the field inhomogeneity during the study, and simply transforming the field map to an EPI image space is not sufficient.

Finally, one notes that the similarity measure used in our registration method is calculated based on image intensities, more specifically, the histogram of the intensities. One assumption of the method is that different tissues in the image have different intensity ranges. Therefore, strong intensity variations across the image, as in the 7T conventional MR image, or low contrast between different tissues, which usually happens in EPI images with low resolution, may affect the accuracy of the registration results. In conclusion, the selection of one or the other approach for correction of distortions in EPI images should be based on a careful analysis of the image characteristics.

CHAPTER VII

CONCLUSION AND FUTURE WORK

1. Conclusion

In this thesis we developed methods based on nonrigid registration to correct in EPI images the geometric and intensity distortions caused by the inhomogeneity in the main magnetic field. Our methods are founded on the physics of Echo Planar Imaging. First, we incorporated a new rephasing factor into our nonrigid registration algorithm to account for signal loss due to dephasing in GE EPI images. Second, we introduced a spatially varying scale mechanism into our registration algorithm to adapt the local scale properties of the deformation field to match these with the characteristics of the actual geometric distortions in EPI images. Third, we proposed to combine the field-map method and the nonrigid registration method for correction of distortions in EPI images. We also compared three distortion correction methods to study their advantages and disadvantages, which provides insights into the selection of field map based or registration based methods for distortion correction of EPI images under certain circumstances.

GE EPI images are susceptible to both geometric distortions and signal loss. While MR imaging physics has been used in nonrigid registration methods for distortion correction, a physics-based model specifically for GE EPI has not been used in any registration method. In Chapter III, we added into our registration algorithm a new intensity correction factor derived to compensate for intra-voxel dephasing in GE EPI images. Intra-voxel dephasing causes signal loss and thus intensity attenuation in the

images. The new rephasing factor we introduce, which changes the intensity of a voxel in images during the registration, is used to improve the accuracy of the intensity-based nonrigid registration method and mitigate the intensity attenuation effect. Simulation-based experiments were first used to evaluate the method. An MR simulator and a real field map were used to generate a realistic GE EPI image. The geometric distortion computed from the field map was used as the ground truth to which the estimated nonrigid deformation can be compared. We then applied the algorithm to 5 datasets of real human brain images. The results show that, after registration, alignment between EPI and multi-shot, spin-echo images, which have relatively long acquisition times but negligible distortions, is improved and that signal loss caused by dephasing can be recovered.

The property of geometric distortion in EPI images can be quite different across the images. The magnitude of the distortion changes smoothly in areas inside the brain but dramatically at the interfaces between air and tissues. This makes the distortion heterogeneous. To make the deformation field estimated by nonrigid registration be as similar to the real distortions as possible, such characteristics should be included in the registration process. In Chapter IV, we proposed a novel approach in which the regularization of the field is adapted spatially based on a scale map. We also presented a method by which this scale map can be generated according to a priori information about the distortions. In the experiments, we first applied the proposed approach to images with known deformation and scale information. Then, we applied it to simulated and real 3D EPI images. Our results show that the proposed approach provide transformations that are

smoother and that can be computed in a much shorter time (39% less in average for 6 datasets) than those computed when a fixed scale is used without sacrificing accuracy.

Field map methods and nonrigid registration methods are two commonly used retrospective methods for distortion correction in EPI images. Field map methods are simple and fast, but they require additional scans to obtain a field map. Also, the accuracy of the field map measurement is influenced by a number of factors, such as imaging artifacts, subject motion, etc. Methods based on nonrigid registration on the other hand need no additional scan time, and they use an estimated deformation field to approximate the distortions in EPI images. The computation of the deformation field is usually time-consuming and the result may be affected by local minima. The combination of these two methods has not heretofore been studied. In Chapter V, we proposed to use a measured field map as a constraint for the nonrigid registration method. We tested the approach on a simulated image and on a real EPI image of a phantom and found that the correction results are improved and the computational time is reduced.

Which distortion correction method should be chosen for an EPI image is an interesting question to be answered. In Chapter VI, we compared the methods we proposed in this thesis and a field map method on 10 datasets of 3T images and a set of 7T data which includes 5 different shots of EPI images. The effect of correction for both geometric and intensity distortions are compared. The experimental results we have obtained with these datasets suggest that while the three correction methods appear to perform similarly, field map methods, due to their simplicity, should be preferred for the correction of small geometric distortion. When intensity correction is needed or the distortion is larger, the registration method and the combination method perform better.

2. Future Work

In Chapter IV, we used a nonrigid registration with spatially varying scale to estimate the distortions in EPI images. In the experiments, the number of scales (2) used for the classification of the existing distortions is chosen empirically. Whether this selection is optimum has not been investigated yet. The use of more scales in the scale map would be worth exploring. Also, besides the scale property, another property, called the stiffness, of the deformation field could be adapted spatially. In the ABA algorithm, a stiffness parameter λ is used to control the stiffness of the transformation. Duay *et al.* [53] have utilized such technique with success for the nonrigid image registration of images with large space occupying lesions by assigning two different λ values for the intra-ventricular and extra-ventricular regions. Here, as was done for the scale map, a stiffness map could be introduced to control the stiffness of the deformation field. The stiffness map could be computed based on the Jacobian of an estimated distortion field, which measures the amount of displacement in the field.

The methods proposed in this thesis have been evaluated on single EPI images and the results are promising. An extension of this work will be to use them on fMRI time series. Because subject movement usually exists during an fMRI scan, the EPI images in this scan need to be aligned to correct the motion artifact. Instead of performing distortion correction after aligning them together, the EPI images should be first corrected and then aligned. This is because the physics of MR imaging tells us that geometric distortions will happen mainly in the phase encoding direction, which is usually along the y axis in the image. We used this fact in our registration-based correction method, and we constrain our deformation to be in the y axis direction only.

But, after registration (which typically includes rotation) the phase encoding direction may no longer lie along an image axes. Therefore, assuming that a reference image and an fMRI time series have been acquired, distortion correction on these images should be performed as follows. First, the reference image is rigidly registered to each of the EPI image in the series to generate a reference image for each EPI images. Second, the distortions in each EPI image are corrected using the proposed methods. Third, the corrected images are registered to each other for motion correction. Activation analysis can then be performed on images with and without distortion correction to compare the changes.

When extending our methods into time series, temporal smoothness along the obtained deformation fields (in the aligned space) could be used as an additional constraint to help the registration. This is because one can assume that the distortion at the same anatomic location in the EPI images change smoothly along time. To impose this constraint in the registration process, a simple approach is to perform nonrigid registration for the EPI images sequentially and use the obtained deformation field from the previous image as the initial deformation field for the current image. Note that the previous deformation field needs to be transformed into the current image space.

Another interesting direction for nonrigid registration based methods is to correct for distortions in diffusion weighted images (DWIs). In this thesis, we focused mainly on the distortions caused by inhomogeneity in the static magnetic field. While such inhomogeneity also contributes to distortions in DWIs, another important source for distortions in DWIs is the eddy current effect, which is especially manifested in diffusion imaging due to the strong and rapidly switching diffusion weighting gradients. This effect

may lead to shear, shift, and scaling of the resultant images [90]. As mentioned in Chapter II, affine or polynomial registration methods have been used to correct such distortions [29]-[35]. Incorporating physics-based models into nonrigid registration to correct for distortions due to static-field inhomogeneity as well as the eddy current effect in DWIs has not been investigated. A model derived from eddy current principles could be added into the proposed methods in this work to provide an approach dedicated for DWIs distortion correction.

REFERENCES

1. Andersson JL, Hutton C, Ashburner J, Turner R, and Friston K, Modeling geometric deformations in EPI time series, *NeuroImage*, 13 (2001), 903-19.

2. Andersson, JL and Skare, S, A model-based method for retrospective correction of geometric distortions in diffusion-weighted EPI, *NeuroImage*, 16 (2002), 177-99.

3. Reese TG, Davis TL, and Weisskoff RM, Automated shimming at 1.5 T using echo-planar image frequency maps, *J Magnetic Resonance Imaging,* 5 (1995), 739-745.

4. Zhao Y, Anderson AW, and Gore JC, Computer simulation studies of the effects of dynamic shimming on susceptibility artifacts in EPI at high field, *J Magnetic Resonance*, 2005; 173(1):10-22.

5. Constable RT, Functional MR imaging using gradient-echo echo-planar imaging in the presence of large static field inhomogeneities, *J Magnetic Resonance Imaging,* 1995; 5(6):746-52.

6. Yang QX, Dardzinski BJ, Li S, Eslinger PJ, and Smith MB, Multi-gradient echo with susceptibility inhomogeneity compensation (MGESIC): demonstration of fMRI in the olfactory cortex at 3.0 T, *Magnetic Resonance in Medicine*, 1997; 37:331-5.

7. Chen NK and Wyrwicz AM, Correction for EPI distortions using multi-echo gradient-echo imaging, *Magnetic Resonance in Medicine*, 1999; 41:1206-13.

8. Chen NK and Wyrwicz AM, Optimized distortion correction technique for echo planar imaging, *Magnetic Resonance in Medicine*, 2001; 45:525-528.

9. Yang QX, Wang J, Smith MB, Meadowcroft M, Sun X, Eslinger PJ, and Golay X, Reduction of magnetic field inhomogeneity artifacts in echo planar imaging with SENSE and GESEPI at high field, *Magnetic Resonance in Medicine*, 2004; 52(6):1418-23.

10. Chang H and Fitzpatrick JM, A Technique for Accurate Magnetic-Resonance-Imaging in the Presence of Field Inhomogeneities, *IEEE Trans on Medical Imaging*, 1992; 11:319-329.

11. Bowtell RW, McIntyre MC, Commandre MJ, Glover PM, and Mansfield P, Correction of geometric distortion in echo planar images, *Proceedings of the Society of Magnetic Resonance*, 2nd meeting, San Francisco, CA 1994.

12. Morgan PS, Bowtell RW, McIntyre DJO, and Worthington BS, Correction of spatial distortion in EPI due to inhomogeneous static magnetic fields using the reversed gradient method, *J Magnetic Resonance Imaging*, 2004; 19:499-507.

13. Bodammer N, Kaufmann J, Kanowski M, and Tempelmann C, Eddy current correction in diffusion-weighted imaging using pairs of images acquired with opposite diffusion gradient polarity, *Magnetic Resonance in Medicine*, 2004; 51(1):188-93.

14. Zeng HR and Constable RT, Image distortion correction in EPI: Comparison of field mapping with point spread function mapping, *Magnetic Resonance in Medicine*, 2002; 48:137-146.

15. Sumanaweera TS, Glover GH, Binford TO, and Adler JR, MR Susceptibility Misregistration Correction, *IEEE Trans on Medical Imaging,* 1993; 12:251-259.

16. Jezzard P and Balaban RS, Correction for Geometric Distortion in Echo-Planar Images from B_0 Field Variations, *Magnetic Resonance in Medicine*, 1995; 34:65-73.

17. Hutton C, Bork A, Josephs O, Deichmann R, Ashburner J, and Turner R, Image distortion correction in fMRI: A quantitative evaluation, *NeuroImage*, 2002; 16:217-240.

18. Cusack R, Brett M, and Osswald K, An evaluation of the use of magnetic field maps to undistort echo-planar images. *NeuroImage*, 2003; 18:127-142.

19. Jenkinson M, Improved unwarping of EPI images using regularized B_0 maps, *NeuroImage*, 2001; 13:S165.

20. Jenkinson M, Fast, automated, N-dimensional phase-unwrapping algorithm, *Magnetic Resonance in Medicine*, 2003; 49(1): 193-7.

21. Neufeld A, Assaf Y, Graif M, Hendler T, and Navon G, Susceptibility-matched envelope for the correction of EPI artifacts, *Magnetic Resonance Imaging*, 2005; 23(9):947-51.

22. Studholme C, Constable RT, and Duncan JS, Accurate Alignment of Functional EPI Data to Anatomical MRI Using a Physics-Based Distortion Model, *IEEE Trans on Medical Imaging,* 2000; 19(11):1115-27.

23. Kybic J, Thevenaz P, Nirkko A, and Unser M, Unwarping of unidirectionally distorted EPI images, *IEEE Trans on Medical Imaging,* 2000; 19:80-93.

24. Hellier P and Barillot C, Multimodal non-rigid warping for correction of distortions in functional MRI, *Proc. Medical Image Computing and Computer-Assisted Intervention* (*MICCAI),* 2000, 512-20.

25. Skerl D, Pan S, Li R, Fitzpatrick JM, Parks MH, Martin PR, Morgan VL, and Dawant BM, Correction of geometric distortions in EP images using non-rigid registration to corresponding anatomic images, *Proc. SPIE Medical Imaging: Image Processing*, 2001; 4322, 58-68.

26. Ardekani S and Sinha U, Geometric distortion correction of high-resolution 3 T diffusion tensor brain images, *Magnetic Resonance in Medicine*, 2005; 54(5):1163-71.

27. Gholipour A, Kehtarnavaz N, Briggs RW, and Gopinath KS, A field map guided approach to Non-rigid registration of Brain EPI to Structural MRI, *Proc. SPIE Medical Imaging: Image Processing,* 2007; 6512, 651205.

28. Pauchard Y, Smith MR, and Mintchev MP, Improving geometric accuracy in the presence of susceptibility difference artifacts produced by metallic implants in magnetic resonance imaging, *IEEE Trans on Medical Imaging,* 2005; 24(10):1387-99.

29. Mangin JF, Poupon C, Clark C, Le Bihan D, and Bloch I, Eddy-Current Distortion Correction and Robust Tensor Estimation for MR Diffusion Imaging, *Proc. Medical Image Computing and Computer-Assisted Intervention* (*MICCAI)*, 2001, 186-94.

30. Mangin JF, Poupon C, Clark C, Le Bihan D, and Bloch I, Distortion correction and robust tensor estimation for MR diffusion imaging, *Medical Image Analysis*, 2002; 6(3):191-8.

31. Netsch T and Muiswinkel A, Image Registration for Distortion Correction in Diffusion Tensor Imaging, *International Workshop on Biomedical Image Registration (WBIR)*, 2003; 171-80.

32. Netsch T and Muiswinkel A, Quantitative evaluation of image-based distortion correction in diffusion tensor imaging, *IEEE Trans on Medical Imaging,* 2004; 23(7):789-98.

33. Nielsen JF, Ghugre NR, and Panigrahy A, Affine and polynomial mutual information coregistration for artifact elimination in diffusion tensor imaging of newborns, *Magnetic Resonance Imaging,* 2004; 22(9):1319-23.

34. Rohde GK, Barnett AS, Basser PJ, Marenco S, and Pierpaoli C, Comprehensive approach for correction of motion and distortion in diffusion-weighted MRI, *Magnetic Resonance in Medicine,* 2004; 51(1):103-14.

35. Mistry NN and Hsu EW, Retrospective Distortion Correction for 3D MR Diffusion Tensor Microscopy Using Mutual Information and Fourier Deformations, *Magnetic Resonance in Medicine*, 2006; 56(2):310-6.

36. Friston KJ, Ashburner J, Frith CD, Poline JB, Heather JD, and Frackowiak RS J, Spatial registration and normalization of images, *Human Brain Mapping*, 1995; 3(3):165-89.

37. Ashburner J and Friston KJ, Nonlinear spatial normalization using basis functions, *Human Brain Mapping*. 1999; 7(4):254-66.

38. Goshtasby, A, Registration of images with geometric distortions, *IEEE Trans on Geoscience and Remote Sensing*, 1988; 26, 60-4.

39. Meyer CR, Boes JL, Kim B, Bland PH, Zasadny KR, Kison PV, Koral K, Frey KA, and Wahl RL, Demonstration of accuracy and clinical versatility of mutual information for automatic multimodality image fusion using affine and thin-plate spline warped geometric deformations, *Medical Image Analysis*, 1997; 1(3):195-206.

40. Park H, Bland PH, Brock KK, and Meyer CR, Adaptive registration using local information measures, *Medical Image Analysis*, 2004; 8(4):465-73.

41. Rueckert D, Sonoda LI, Hayes C, Hill DL, Leach MO, and Hawkes DJ, Nonrigid registration using free-form deformations: application to breast MR images, *IEEE Trans on Medical Imaging,* 1999; 18(8):712-21.

42. Ledesma-Carbayo MJ, Kybic J, Desco M, Santos A, Suhling M, Hunziker P, and Unser M, Spatio-temporal nonrigid registration for ultrasound cardiac motion estimation, *IEEE Trans on Medical Imaging,* 2005; 24(9):1113-26.

43. Rohde GK, Aldroubi A, and Dawant BM, The adaptive bases algorithm for intensity-based nonrigid image registration, *IEEE Trans on Medical Imaging,* 2003; 22(11):1470-9.

44. Thirion JP, Image matching as a diffusion process: an analogy with Maxwell's demons, *Medical Image Analysis*, 1998; 2(3):243-60.

45. Guimond A, Roche A, Ayache N, and Meunier J, Three-dimensional multimodal brain warping using the demons algorithm and adaptive intensity corrections, *IEEE Trans on Medical Imaging,* 2001; 20(1):58-69.

46. Stefanescu R, Pennec X, and Ayache N, Grid powered nonlinear image registration with locally adaptive regularization, *Medical Image Analysis*, 2004; 8(3):325-42.

47. Hermosillo G, Chef d'Hotel C, and Faugeras O, Variational methods for multimodal image matching, *International Journal of Computer Vision,* 2002; 50(3), 329-43.

48. D'Agostino E, Maes F, Vandermeulen D, and Suetens P, A Viscous Fluid Model for Multimodal Non-rigid Image Registration Using Mutual Information, *Proc. Medical Image Computing and Computer-Assisted Intervention* (*MICCAI)*, 2002; 541-8.

49. Christensen GE, Rabbitt RD, Miller MI, Joshi SC, Grenander U, Coogan TA, and Van Essen DC, Topological properties of smooth anatomic maps, *Proc. Information Processing in Medical Imaging(IPMI)*, 1995; 101-12.

50. Rohlfing T, Maurer CR Jr, Bluemke DA, and Jacobs MA, Volume-preserving nonrigid registration of MR breast images using free-form deformation with an incompressibility constraint, *IEEE Trans on Medical Imaging,* 2003; 22(6):730-41.

51. Hellier P, Barillot C, Memin E, and Perez P, Hierarchical estimation of a dense deformation field for 3-D robust registration, *IEEE Trans on Medical Imaging,* 2001; 20(5):388-402.

52. Lester H, Arridge SR, Jansons KM, Lemieux L, Hajnal JV, and Oatridge A, Non-linear Registration with the Variable Viscosity Fluid Algorithm, *Proc. Information Processing in Medical Imaging(IPMI)*, 1999; 238-51.

53. Duay V, D'Haese PF, Li R, and Dawant BM, Non-rigid registration algorithm with spatially varying stiffness properties, *Proc. International Symposium on Biomedical Imaging: From Nano to Macro (ISBI)*, 2004; 408-11.

54. Staring M, Klein S, and Pluim JPW, Nonrigid registration using a rigidity constraint, *Proc. SPIE Medical Imaging: Image Processing*, 2006; 6144, 614413.

55. Li X, Peterson TE, Yankeelov T, Gore J, and Dawant BM, Constrained non-rigid registration for whole-body image registration: method and validation, *Proc. SPIE Medical Imaging: Image Processing*, 2007; 6512, 651202.

56. Rohlfing T and Maurer CR, Intensity-based non-rigid registration using adaptive multilevel free-form deformation with an imcompressibility constraint, *Proc. Medical Image Computing and Computer-Assisted Intervention* (*MICCAI),* 2001; 111-9.

57. Schnabel JA, Rueckert D, Quist M, Blackall JM, Castellano-Smith AD, Hartkens T, Penney GP, Hall WA, Liu H, Truwit CL, Gerritsen FA, Hill DLG, and Hawkes DJ, A generic framework for non-rigid registration based on non-uniform multi-level free-form deformations, *Proc. Medical Image Computing and Computer-Assisted Intervention* (*MICCAI),* 2001; 573-581.

58. Jezzard P and Clare S, Sources of distortion in functional MRI data, *Human Brain Mapping*, 1999; 8(2-3):80-5.

59. Commowick O, Stefanescu R, Fillard P, Arsigny V, Ayache N, Pennec X, and Malandain G, Incorporating Statistical Measures of Anatomical Variability in Atlas-to-Subject Registration for Conformal Brain Radiotherapy, *Proc. Medical Image Computing and Computer-Assisted Intervention* (*MICCAI)*, 2005; 927-934.

60. Pekar V, Gladilin E, and Rohr K, An adaptive irregular grid approach for 3D deformable image registration, *Physics in Medicine and Biology*, 2006; 51(2):361-77.

61. Jacobs AH, Kracht LW, Gossmann A, Ruger MA, Thomas AV, Thiel A, and Herholz K, Imaging in neurooncology, *NeuroRx,* 2005; 2:333-47.

62. Bakshi R, Minagar A, Jaisani Z, and Wolinsky JS, Imaging of multiple sclerosis: role in neurotherapeutics, *NeuroRx*, 2005; 2:277-303.

63. Dickerson BC and Sperling RA, Neuroimaging biomarkers for clinical trials of disease-modifying therapies in Alzheimer's disease, *NeuroRx*, 2005; 2:348-60.

64. Yoder DA, Zhao YS, Paschal CB, and Fitzpatrick JM, MRI simulator with object-specific field map calculations, *Magnetic Resonance Imaging*, 2004; 22: 315-28.

65. Xu N, Li Y, Paschal CB, Gatenby JC, Morgan VL, Pickens DR, Dawant BM, and Fitzpatrick JM, Simulation of susceptibility-induced distortions in fMRI, *Proc. SPIE Medical Imaging: Image Processing,* 2006; 6144: 2071-79.

66. Hardy PA, Kucharczyk W, and Henkelman RM, Cause of signal loss in MR images of old hemorrhagic lesions, *Radiology*, 1990; 174(2):549-55.

67. Haacke EM, Brown RW, Thompson MR, and Venkatesan R, Magnetic resonance imaging—physical principles and sequence design, New York, NY: John Wiley and Sons, 1999.

68. Fernandez-Seara MA and Wehrli FW, Postprocessing technique to correct for background gradients in image-based R2* measurements, *Magnetic Resonance in Medicine*, 2000; 44(3):358-66.

69. Studholme C, Hill DLG and Hawkes DJ, An overlap invariant entropy measure of 3D medical image alignment, *Pattern Recognition*, 1999; 32:71-86.

70. http://www.fmrib.ox.ac.uk/fsl/.

71. http://www.fil.ion.ucl.ac.uk/spm/toolbox/fieldmap/.

72. Xu N, Li Y, Fitzpatrick JM, Dawant BM, Morgan VL, and Pickens DR, Realistic Computer Generated fMRI Phantoms with Motion Correlated Susceptibility Artifacts, *Proc. International Society for Magnetic Resonance in Medicine (ISMRM) 14th Scientific Meeting*, 2006; 2833.

73. Pruessmann KP, Weiger M, Scheidegger MB, and Boesiger P, SENSE: Sensitivity encoding for fast MRI, *Magnetic Resonance in Medicine*, 1999; 42(5):952-62.

74. Bammer R, Keeling SL, Augustin M, Pruessmann KP, Wolf R, Stollberger R, Hartung HP, and Fazekas F, Improved diffusion-weighted single-shot echo-planar imaging (EPI) in stroke using Sensitivity Encoding (SENSE), *Magnetic Resonance in Medicine*, 2001; 46(3):548-54.

75. Golay X, Pruessmann KP, Weiger M, Crelier GR, Folkers PJM, Kollias SS, and Boesiger P, PRESTO-SENSE: An ultrafast whole-brain fMRI technique, *Magnetic Resonance in Medicine*, 2000; 43(6):779-86.

76. Wu Z, Compactly supported positive definite radial functions, *Advances in Computational Mathematics*, 4 (1995), 283-92.

77. Xue Z, Shen D, and Davatzikos C, Statistical representation of high-dimensional deformation fields with application to statistically constrained 3D warping, *Medical Image Analysis*, 2006; 10(5):740-51.

78. Li Y, Xu N, Fitzpatrick JM, Morgan VL, Pickens DR, and Dawant BM, Accounting for Signal Loss due to Dephasing in the Correction of Distortions in Gradient-Echo EPI via Nonrigid Registration, *IEEE Trans on Medical Imaging,* to be published.

79. Collins CM, Yang B, Yang QX, and Smith MB, Numerical calculations of the static magnetic field in three-dimensional multi-tissue models of the human head, *Magnetic Resonance Imaging,* 2002; 20:413-24.

80. Truong TK, Clymer BD, Chakeres DW, and Schmalbrock P, Three-dimensional numerical simulations of susceptibility-induced magnetic field inhomogeneities in the human head, *Magnetic Resonance Imaging*, 2002; 20:759-70.

81. Thirion B, Flandin G, Pinel P, Roche A, Ciuciu P, and Poline JB, Dealing with the shortcomings of spatial normalization: multi-subject parcellation of fMRI datasets, *Human Brain Mapping*, 2006; 27(8):678-93.

82. Jones DK, Griffin LD, Alexander DC, Catani M, Horsfield MA, Howard R, and Williams SCR, Spatial Normalization and Averaging of Diffusion Tensor MRI Data Sets, *NeuroImage,* 2002; 17(2): 592-617.

83. Wells WM III, Viola P, Atsumi H, Nakajima S, and Kikinis R, Multi-modal volume registration by maximization of mutual information, *Medical Image Analysis*, 1996; 1(1):35-51.

84. Maes F, Collignon A, Vanderneulen D, Marchal G, and Suetens P, Multimodality image registration by maximization of mutual information*, IEEE Trans on Medical Imaging*, 1997; 16(2*)*:187-98.

85. A Roche, G Malandain, X Pennec, and N Ayache, The correlation ratio as a new similarity measure for multimodal image registration, *Proc. Medical Image Computing and Computer-Assisted Intervention* (*MICCAI)*, 1998; 1115-24.

86. Sled JG and Pike GB, Standing-wave and RF penetration artifacts caused by elliptic geometry: an electrodynamic analysis of MRI, *IEEE Trans on Medical Imaging,* 1998; 17:653-62.

87. Kangarlu A, Baertlein BA, Lee R, Ibrahim T, Yang L, Abduljalil AM, and Robitaille PM, Dielectric resonance phenomena in ultra high field MRI, *J Computer Assisted Tomography*, 1999; 23:821-31.

88. Styner M, Gerig G, Brechbuehler C, and Szekely G, Parametric estimate of intensity inhomogeneities applied to MRI, *IEEE Trans on Medical Imaging,* 2000; 19(3):153-165.

89. Zhao Y, Zeng H, and Gore JC, B_0 Field Mapping with a Fast Asymmetric Spin Echo Sequence at High Field, *Proc. International Society for Magnetic Resonance in Medicine (ISMRM) 13th Scientific Meeting*, 2005; 2248.

90. Jezzard P, Barnett AS, and Pierpaoli C, Characterization of and correction for eddy current artifacts in echo planar diffusion imaging, *Magnetic Resonance in Medicine*, 1998; 39(5): 801-12.

91. Pekar V, Gladilin E, and Rohr K, An adaptive irregular grid approach for 3D deformable image registration, *Physics in Medicine and Biology,* 2006; 51: 361-77.